Journal of Structural Geology 92 (2016) 140–177

Contents lists available at ScienceDirect

Journal of Structural Geology

journal homepage: www.elsevier.com/locate/jsg

Benchmarking numerical models of brittle thrust wedges

Susanne J.H. Buiter [a, b, *], Guido Schreurs [c], Markus Albertz [d], Taras V. Gerya [e], Boris Kaus [f], Walter Landry [g, 1], Laetitia le Pourhiet [h], Yury Mishin [e], David L. Egholm [i], Michele Cooke [j], Bertrand Maillot [k], Cedric Thieulot [l, b], Tony Crook [m], Dave May [e], Pauline Souloumiac [n, 2], Christopher Beaumont [o]

[a] Geodynamics Team, Geological Survey of Norway, Trondheim, Norway
[b] The Centre for Earth Evolution and Dynamics, University of Oslo, Norway
[c] Institute of Geological Sciences, University of Bern, Switzerland
[d] ExxonMobil Upstream Research Company, Houston, TX, USA
[e] Department of Earth Sciences, Swiss Federal Institute of Technology, Zürich, Switzerland
[f] Institute of Geosciences, Johannes Gutenberg University Mainz, Germany
[g] Computational Infrastructure for Geodynamics, Caltech, USA
[h] Sorbonne Universités, UMPC Univ Paris 06, Institute des Sciences de la Terre de Paris, France
[i] Department of Earth Sciences, University of Aarhus, Denmark
[j] Department of Geosciences, University of Massachusetts, Amherst, MA, USA
[k] Département Géosciences et Environnement, Université de Cergy-Pontoise, France
[l] Department of Earth Sciences, Utrecht University, the Netherlands
[m] Three Cliffs Geomechanical Analysis Ltd, Swansea, UK
[n] Ecole des Mines, Paris, France
[o] Department of Oceanography, Dalhousie University, Halifax, NS, Canada

ARTICLE INFO

Article history:
Received 13 July 2015
Received in revised form
29 February 2016
Accepted 8 March 2016
Available online 16 March 2016

Keywords:
Thrust wedges
Benchmarking
Critical taper
Shear zones
Numerical modelling
Plasticity

ABSTRACT

We report quantitative results from three brittle thrust wedge experiments, comparing numerical results directly with each other and with corresponding analogue results. We first test whether the participating codes reproduce predictions from analytical critical taper theory. Eleven codes pass the stable wedge test, showing negligible internal deformation and maintaining the initial surface slope upon horizontal translation over a frictional interface. Eight codes participated in the unstable wedge test that examines the evolution of a wedge by thrust formation from a subcritical state to the critical taper geometry. The critical taper is recovered, but the models show two deformation modes characterised by either mainly forward dipping thrusts or a series of thrust pop-ups. We speculate that the two modes are caused by differences in effective basal boundary friction related to different algorithms for modelling boundary friction. The third experiment examines stacking of forward thrusts that are translated upward along a backward thrust. The results of the seven codes that run this experiment show variability in deformation style, number of thrusts, thrust dip angles and surface slope. Overall, our experiments show that numerical models run with different numerical techniques can successfully simulate laboratory brittle thrust wedge models at the cm-scale. In more detail, however, we find that it is challenging to reproduce sandbox-type setups numerically, because of frictional boundary conditions and velocity discontinuities. We recommend that future numerical-analogue comparisons use simple boundary conditions and that the numerical Earth Science community defines a plasticity test to resolve the variability in model shear zones.

1. Introduction

Numerical and analogue models are frequently and successfully used to investigate the evolution of deformation processes in the crust and lithosphere. Analogue models are built of materials, such

* Corresponding author.
E-mail address: susanne.buiter@ngu.no (S.J.H. Buiter).
[1] Now at: Infrared Processing and Analysis Center, Caltech, Pasadena, USA.
[2] Now at: Département Géosciences et Environnement, Université de Cergy-Pontoise, France.

http://dx.doi.org/10.1016/j.jsg.2016.03.003

as sand, clay, wax, and silicone putty, to achieve a scaled representation of a so-called natural prototype (Hubbert, 1937). Numerical models can be designed at the actual scale of the problem, but need to approximate Earth's materials and their deformation behaviour with equations. The freedom in both model approaches, in terms of choices of modelling method, material properties, boundary conditions, and deformation mechanisms, could imply an effect on model results. Most of these freedoms can be investigated within the same software or analogue laboratory. The method aspect is usually addressed in benchmark studies, that compare results of simulations of the same experimental setup directly. Here the numerical modelling community has a longer history (e.g., Blankenbach et al., 1989; Van Keken et al., 2008; Schmeling et al., 2008; Crameri et al., 2012), than the analogue modelling community where the first analogue benchmark study involving results of five laboratories was reported by Schreurs et al. (2006). Because numerical and analogue models approach similar deformation problems with very different methods, it could be argued that the confidence level in the findings of studies would increase if analogue and numerical results were similar. Some studies have, therefore, combined the two modelling techniques in their investigation of brittle or brittle-viscous deformation processes (e.g., Exadaktylos et al., 2003; Ellis et al., 2004; Panien et al., 2006a; Nilfouroushan et al., 2012). Among the questions that arise is not only the more fundamental question of how applicable the individual methods are to the study of processes in the crust or lithosphere, but also whether numerical models can be directly compared to analogue models.

Many analogue models use granular materials, such as quartz sand, corundum sand, or microbeads, as their building material. It is, therefore, often thought that numerical models that consist of an assembly of particles, such as computed with the distinct element method (DEM) (Cundall and Strack, 1979), would intrinsically be best suited for simulating sand-like materials. The normal shear zones forming horst-and-graben structures in the earlier DEM models by Saltzer and Pollard (1992) and Saltzer (1992), for example, resemble structures typically observed in analogue models, while the later models of Seyferth and Henk (2006) and Egholm et al. (2007) nicely capture most deformation structures of corresponding analogue models of basin formation. It should be kept in mind though that DEM particles cannot be equated with sand grains and that one particle typically will correspond to several grains. Several studies also show that methods that assume a continuous medium, such as finite difference (FDM) or finite element (FEM) methods, may successfully simulate granular materials. The Lagrangian FEM models of Crook et al. (2006), for example, resemble the half-graben models of McClay (1990) in fair detail. Encouraging agreement between results from finite element and analogue models is also shown by, among others, Smart and Couzens-Schultz (2001); Ellis et al. (2004); Panien et al. (2006a); Le Pourhiet et al. (2006); and Nilfouroushan et al. (2012).

In connection with the GeoMod2004 meeting, a series of models investigated how well different numerical solution methods could reproduce sandbox structures by comparing results of six numerical codes for two prescribed setups to results of five analogue laboratories (Schreurs et al., 2006; Buiter et al., 2006) (Fig. 1). To first order, it was shown that numerical and analogue models obtain a similar evolution with localisation of deformation onto shear zones, and that different numerical techniques (FEM, FDM and DEM) are capable of reproducing structures observed in the analogue sandbox experiments. But the experiments also pointed to variability among models in number of shear zones, their dip angle and spacing, and in the evolution of surface slope for thrust wedges. This formed our motivation to organise new comparison experiments, with the aim to try to understand these differences in a quantitative manner. Our new experiments focus on brittle thrust wedges, because critical taper theory provides an analytical background for these setups (Davis et al., 1983; Dahlen et al., 1984) and many previous studies investigated brittle thrust wedge behaviour with analogue and numerical models (e.g., Cadell, 1890; Koyi, 1995; Burbidge and Braun, 2002; Lohrmann et al., 2003; Simpson, 2011; Buiter, 2012; Graveleau et al., 2012; Mary et al., 2013). Our three thrust wedge setups resemble setups frequently used by especially analogue models. Here, we present results of eleven numerical codes, which use finite element, finite difference, boundary element, and distinct element techniques. The companion paper of Schreurs et al. (2016) presents the results of fifteen laboratories for the same setups. The analogue models used the same quartz and corundum sand, the same type of foil to cover the base and walls of the model apparatus, and followed a model building protocol that prescribed sieve structure, sifting height, and filling rate. Model widths (parallel to the mobile wall) varied between 20 and 80 cm among the laboratories, while model length was fixed (at 35 cm for experiments 2 and 3). Despite the strict model protocol, the analogue results show variability in especially surface slope, thrust spacing, and number of forward and backward thrusts. These variations show that even small changes in initial model building – the human factor – may affect the mechanical properties of the sand pack and it's boundary friction and thus cause variations that impact model evolution.

2. Critical compressional wedges

Fold-and-thrust belts and accretionary wedges form in compressional settings by offscraping of sediments and crustal materials from a lower plate and stacking these in the foreland of an orogen or at a subduction zone trench. This process has been compared to a wedge of snow or soil accreting in front of a moving bulldozer in a set of papers by Davis et al. (1983); Dahlen (1984), and Dahlen et al. (1984). The material in front of the bulldozer will deform until a so-called critical taper ($\alpha + \beta$) is reached, where α is the surface dip angle and β the basal dip angle of the wedge (Fig. 2a,b). If no further material is encountered, the wedge will slide in a stable manner and not experience deformation. If new material enters the wedge, the wedge will grow self-similarly at the critical taper value. The critical taper of a brittle wedge can be derived under the assumptions that the material in the wedge is at the verge of failure everywhere, the strength of the base does not exceed the interior strength, the base is cohesionless, and brittle failure occurs following pressure-dependent Mohr–Coulomb behaviour:

$$\left|\tau\right| = C + \tan(\phi)\left(\sigma_n - P_f\right) \quad (1)$$

τ is the shear stress, σ_n the normal stress, φ the angle of internal friction, and P_f the pore fluid pressure. In this study, we only consider dry wedges, for which the pore fluid pressures are zero. The sands in the corresponding analogue experiments of Schreurs et al. (2016) have not only an internal cohesion C, but also a basal cohesion C_b. Whereas a cohesionless wedge ($C = 0$) will have a perfectly triangular form, the higher internal strength for a constant cohesion wedge leads to a concave upward wedge shape (decreasing taper angle towards the wedge toe) (Dahlen et al., 1984). The effect of a basal cohesion is an increased resistance to start sliding of the wedge over the base. This effect would be strongest near the wedge toe (where normal stresses are smallest) and the wedge is expected to have a convex upward shape there. The analytical solutions of critical taper theory do not apply for cases with basal cohesion, and our models are therefore not expected to follow the critical taper solution exactly near the wedge

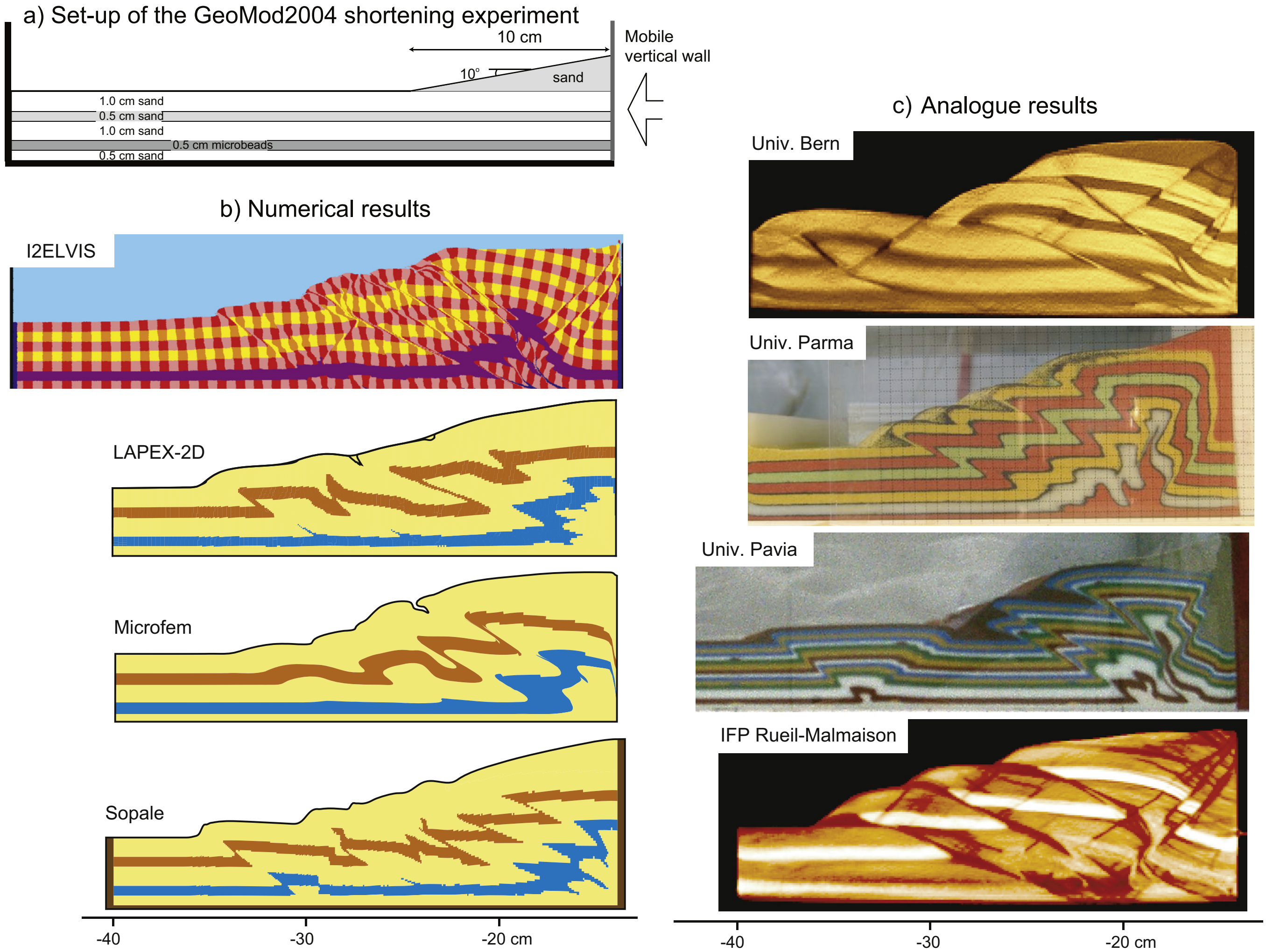

Fig. 1. A selection of results of the GeoMod2004 analogue and numerical thrust wedge comparison experiment (Buiter et al., 2006; Schreurs et al., 2006). a) A 3.5 cm high sand package with an embedded microbeads layer is shortened by a mobile wall moving into the model domain. A pre-existing wedge of sand with a surface slope of 10° lies on top of the sand layers, next to the mobile wall. b) Numerical results after 14 cm of shortening. I2ELVIS is a finite-difference model, LAPEX-2D a FLAC-type finite-difference model, and microfem and SOPALE are arbitrary Lagrangian Eulerian finite-element models. A description of the codes is in Buiter et al. (2006). c) Analogue results after 14 cm of shortening. The sections of Bern and IFP Rueil-Malmaison are CT scans through the centre of the model domain, whereas the sections of Parma and Pavia are sidewall observations. More details of the analogue models are in Schreurs et al. (2006). Figures reproduced from Buiter et al. (2006) with permission from the Geological Society of London.

toe.

The critical taper equation is:

$$\alpha + \beta = \psi_b - \psi_0 \tag{2}$$

α is the surface slope, β the basal slope and their sum ($\alpha + \beta$) the taper angle, which should be positive (Fig. 2a,b). ψ_b and ψ_0 are the angles between the maximum principal stress σ_1 and the base and top of the wedge, respectively. For a cohesionless wedge:

$$\psi_b = \frac{1}{2}\arcsin\left(\frac{\sin\phi_b}{\sin\phi}\right) - \frac{1}{2}\phi_b \tag{3}$$

$$\psi_0 = \frac{1}{2}\arcsin\left(\frac{\sin\alpha}{\sin\phi}\right) - \frac{1}{2}\alpha \tag{4}$$

ϕ_b is the angle of basal friction.

For a given basal dip angle, two values for surface dip angle lead to admissible solutions for the critical taper (except at the extremes of the basal dip domain) (Fig. 2a,b). Of these, the lower critical taper value defines the boundary between the domain of subcritical wedges and supercritical wedges. For supercritical wedges that are in the stable regime, the requirement that the material in the wedge is on the verge of failure everywhere is no longer valid. However, wedges that are in the stable regime and that do not accrete new material, will slide stably, without deformation. This is our first wedge experiment. Subcritical wedges will deform upon compression towards the critical taper value. Our second and third experiments start as subcritical wedges.

3. Modelling approach

3.1. Mechanical equations

The momentum equation for slow creeping flows is:

$$\nabla \cdot \boldsymbol{\sigma}' - \nabla P + \rho \mathbf{g} = 0 \tag{5}$$

$\boldsymbol{\sigma}'$ is the deviatoric stress tensor (the full stress tensor $\boldsymbol{\sigma} = \boldsymbol{\sigma}' - PI$), P pressure, ρ density, and $\mathbf{g}$ gravitational acceleration ($g_x = 0$ and $g_z = -9.81$ m s^{-2}). Compressional stresses are positive. Conservation of mass is given by:

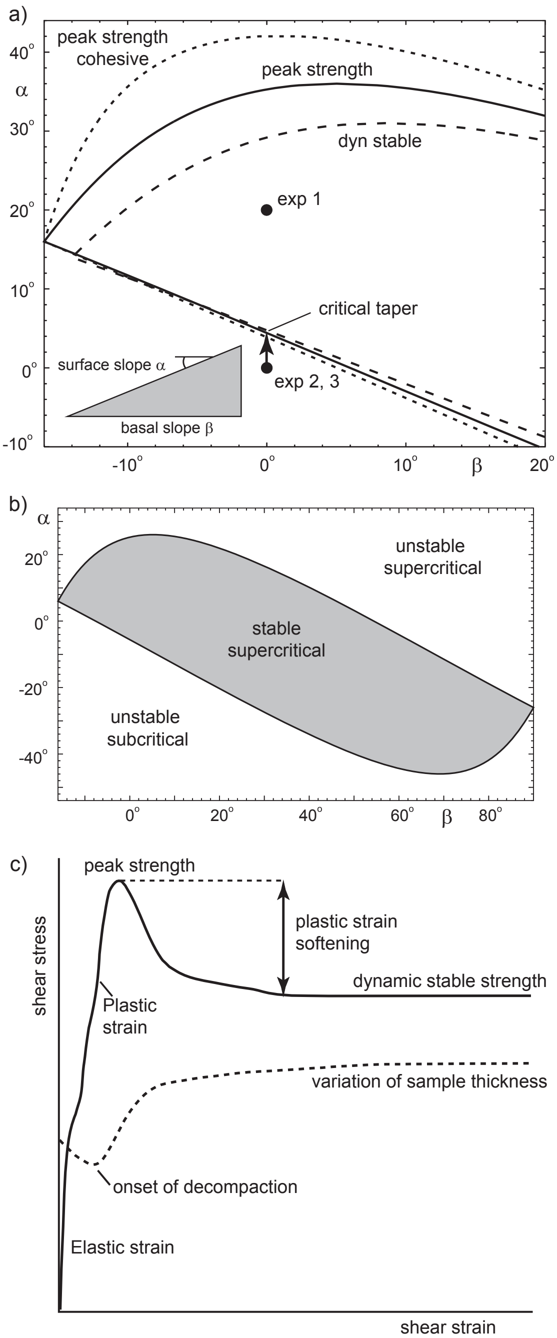

Fig. 2. Wedge stability fields for quartz sand. a) Zoom of critical taper curves for cohesionless sand at peak strength ($\varphi = 36°$, $\phi_b = 16°$ and $C = 0$ Pa), cohesionless sand at dynamic stable strength ($\varphi = 31°$, $\phi_b = 14°$ and $C = 0$ Pa), and a cohesive sand at peak strength with depth-dependent cohesion ($\varphi = 36°$, $\phi_b = 16°$ and $C = 2000$ Pa m^{-1} × depth, following Zhao et al. (1986)). Peak and dynamic stable strengths as in panel c. b) Full stability field for cohesionless sand at peak strength. c) Schematic plot of shear stress versus shear strain for sand (modified from Lohrmann et al. (2003); Panien et al. (2006b)). Strain-softening from peak strength to dynamic-stable strength correlates with sand dilation. We explicitly prescribe the plastic strain-softening behaviour for our continuum numerical experiments.

$$\frac{\partial \rho}{\partial t} + \nabla \cdot (\rho \boldsymbol{u}) = 0 \tag{6}$$

$\boldsymbol{u}$ is the velocity. For incompressible materials $\frac{\partial \rho}{\partial t} = 0$ and the equation reduces to $\nabla \cdot \boldsymbol{u} = 0$.

3.2. Brittle rheology and material properties

The analogue wedges of Schreurs et al. (2016) are built of quartz and corundum sands (Klinkmüller et al., 2016) (Table 1). These sands are characterised by angle of internal friction φ, cohesion C, and dilation ψ. Loading of sand first leads to limited elastic deformation, followed by strain-hardening before failure at peak strength (Fig. 2c). Further strain leads to softening until an often stable dynamic strength is reached (Lohrmann et al., 2003; Panien et al., 2006b). Shear bands form close to the peak strength at maximum dilation rates, whereas the dynamic stable state is associated with decreased decompaction rates. Because the peak angle of internal friction varies with handling technique (i.e., sprinkling or pouring) (Krantz, 1991; Schellart, 2000; Lohrmann et al., 2003), the analogue wedges in the companion paper have a prescribed sieving height (20 cm) and rate (250 ml min^{-1}) (Schreurs et al., 2016). The values for internal angle of friction for the quartz and corundum sands are reasonably well constrained, but larger uncertainty exists in the boundary friction for quartz sand (Table 1). However, the greatest variations occur in the values for internal cohesion and boundary cohesion, because these are obtained by linear extrapolation to zero normal stress on shear stress versus normal load curves. We have strongly simplified the cohesion values for our numerical experiments.

The formation of shear zones in the particle-based DEM method most resembles the formation of shear bands in granular materials. DEM models implicitly include dilation and its associated softening behaviour. Finite-element and finite-difference methods usually employ a Drucker–Prager failure criterion which is a smooth version of the angular Mohr–Coulomb failure criterion (Eq. (1)). In stress invariants, the Drucker–Prager criterion is:

$$\sigma_e = P \sin\phi + C \cos\phi \tag{7}$$

σ_e is the effective shear stress as determined by the second invariant of the stress tensor $\boldsymbol{\sigma}$ ($\sigma_e = \left(\frac{1}{2}\sigma_{ij}\sigma_{ij}\right)^{\frac{1}{2}}$) and total pressure P is the mean stress.

The numerical material properties follow the analogue properties as closely as possible (Table 1). Sands initially have non-zero value for the dilation angle, which will tend towards zero once a shear band forms (Fig. 2c). However, we have no exact dilation values for the sands used in Schreurs et al. (2016). Also, most of the participating continuum codes are incompressible. For continuum models, we therefore prescribe $\psi = 0$ throughout and explicitly prescribe softening from peak strength to stable strength. Softening is simulated by a linear decrease of the peak angle of internal friction to the stable angle over a finite strain interval of 0.5–1.0 (finite strain is measured from the deviatoric strain tensor $\boldsymbol{\varepsilon}'$ as $\left(\frac{1}{2}\varepsilon'_{ij}\varepsilon'_{ij}\right)^{\frac{1}{2}}$). Boundary friction for our models also shows softening behaviour. As an aside, for associated flows ($\varphi = \psi$), a unique shear zone dip angle exists (the Coulomb angle, Section 3.3), but the dilation causes the shear band to widen as it shears (Choi and Petersen, 2015). One solution to this shear band expansion is to reduce the dilation angle with accumulated strain, similar as to what would occur in sands (Choi and Petersen, 2015). Because the bulk moduli of sand are on the order of hundreds MPa to a GPa and stresses within the experiments are 1–1000 Pa, we ignore the role of elasticity.

3.3. The dip angle of shear zones

In granular materials, the dip angle of shear bands with maximum compressive stress σ_1 varies between the Roscoe (1970) angle:

Table 1
Material properties (at cm-scale).

Parameter	Numerical	Analogue range[a]
Quartz sand (n = 5)		
Density ρ (kg m^{-3})	1560	1560
Angle of internal friction (peak strength) ϕ^p	36°	34° – 37°
Angle of internal friction (dynamic stable strength) ϕ^s	31°	30°–31°
Apparent internal cohesion (Pa) C	30	19–69
Boundary friction (peak strength) ϕ_b^p	16°	15°–21°[b]
Boundary friction (dynamic stable strength) ϕ_b^s	14°	9°–14°
Apparent boundary cohesion (Pa) C_b	30	14–141
Dilation angle	0°	
Corundum sand (n = 3)		
Density ρ (kg m^{-3})	1890	1890
Angle of internal friction (peak strength) ϕ^p	36°	35°–36°
Angle of internal friction (dynamic stable strength) ϕ^s	31°	31°
Apparent internal cohesion (Pa) C	30	15–28
Boundary friction (peak strength) ϕ_b^p	24°	23°–25°
Boundary friction (dynamic stable strength) ϕ_b^s	23°	22°–24°
Apparent boundary cohesion (Pa) C_b	30	23–44
Dilation angle	0°	
Whole model		
Background viscosity η_m (Pa s)	10^{12}	
Gravitational acceleration g_z (m s^{-2})	−9.81	
Time step Δt (s)	3.6	
Air viscosity η_{air} (if applicable) (Pa s)	10^4	
Air density ρ_{air} (if applicable) (kg m^{-3})	0	

[a] φ, ϕ_b, C, C_b were measured by Matthias Klinkmüller with the ring-shear tester of GFZ Postdam (Schreurs et al., 2016). ρ is from Panien et al. (2006b) for sands sifted from 30 cm height at a filling rate of 200 cm^3/min.
[b] Value initially measured as 11°–21° but later corrected to 15°–21°.

$$\theta_R = 45° - \psi/2 \tag{8}$$

the Coulomb (1773) angle:

$$\theta_C = 45° - \varphi/2 \tag{9}$$

and the intermediate Arthur et al. (1977) angle:

$$\theta_A = 45° - (\varphi + \psi)/4 \tag{10}$$

ψ is the angle of dilation (Roscoe, 1970):

$$\sin\psi = \frac{\dot{\varepsilon_1} + \dot{\varepsilon_3}}{\dot{\varepsilon_3} - \dot{\varepsilon_1}} \tag{11}$$

ε_i are the principal strains. All shear band inclinations between the Coulomb and Roscoe solutions are admissible (Vermeer, 1990). Fine sands tend to lead to Coulomb angles, whereas course sand tend to Roscoe angles (Vermeer, 1990). For granular materials, the orientation of shear bands with σ_1 increases with confining pressure (Bésuelle et al., 2000). As analogue sand models have low confining pressure, shear bands would be more likely to form at Coulomb angles.

The dip angle of shear zones in continuum models has also been shown to vary between the Roscoe, Arthur and Coulomb dip angles (Vermeer, 1990; Lemiale et al., 2008; Kaus, 2010). Coulomb angles require a fine numerical mesh (Lemiale et al., 2008), a well resolved heterogeneity that initiates the shear band (Kaus, 2010), and dynamic (rather than lithostatic) pressures (Buiter, 2012). A coarse mesh, small heterogeneities, or lithostatic pressure result in steeper dip angles than Coulomb in compression.

The theoretical dip angle predictions are relative to σ_1. Initially, σ_1 will be horizontal in experiments that have horizontal top and base (our second and third experiment). For incompressible materials ($\psi = 0$), predicted shear zone dip angles for forward and backward thrusts are then (from Eqs. (8)–(10) and with $\varphi = 36°$): Roscoe angle $\theta_R = 45°$, Coulomb angle $\theta_C = 27°$, and Arthur angle $\theta_A = 36°$. However, as topography builds up, the direction of σ_1 rotates to an angle with the base. For critical wedges, the dip angles of forward and backward thrusts relative to the base of the wedge can be computed by using the critical taper prediction for ψ_b, the angle between σ_1 and the wedge base (Eq. (3)). For the material properties in Table 1, ψ_b is 6°. Predicted shear zone forward dip angles and backward dip angles relative to the base of the wedge can then be found by subtracting or adding ψ_b to the shear zone dip angles resulting in (forward/backward): Roscoe angle $\theta_R = 39°/51°$, Coulomb angle $\theta_C = 21°/33°$, and Arthur angle $\theta_A = 30°/42°$. Forward thrusts that form later in the evolution of a wedge could, therefore, be expected to become progressively shallower relative to the base of the wedge, whereas backward thrusts form progressively in a steeper manner.

3.4. Boundary conditions

The analogue sand wedges have frictional basal and side boundary conditions, which are not straightforward to represent in numerical models. In our study, different approaches have been used to simulate boundary friction. Because no community test for boundary friction in sandbox-like experiments exists, we can not rule out that variations in model outcomes could be caused by variations in the implementation of boundary friction. We will come back to this when discussing the second experiment. Seven of our codes (ELEFANT, GALE, I3VIS, MILAMIN_VEP, SDEM, Sdvig, and SOPALE) use a frictional boundary layer that is explicitly included in the model domain. The internal frictional parameters of this layer are set equal to the boundary friction parameters. The other codes (EEM, Elfen, Fric2D, and pTatin) use a frictional boundary condition. Further details can be found with the descriptions of the codes (Section 3.6).

I3VIS and Sdvig approximate free surface behaviour by including a layer of so-called 'sticky air' above the sand domain. Following Crameri et al. (2012), this 'air' layer should have zero density, a viscosity low enough relative to the sand (10^4 Pa s was prescribed here), a reasonable vertical resolution, and a minimum thickness. More codes have used a sticky air layer in our first experiment, because this has a triangular sand model domain and adding an air layer allows using an overall quadrilateral model domain.

3.5. Model analysis

We analyse model results in a qualitative manner by visual comparisons and quantitatively by numerical quantities and cross-section measurements. We show cross-sections of the material, strain, strain-rate, and pressure fields. At every 0.5 cm of shortening, we measured surface slope as a visual best fit line through the valleys of the thrusts (following Stockmal et al., 2007) (Fig. 3d). Slope values were measured by two authors (Buiter and Schreurs) and averaged. The maximum difference in the measurements was 2°–3°. The same approach was followed for numerical and analogue results to allow inter-model comparisons. We measured two experimental results for each analogue model and up to three different resolutions for each numerical model. For every new thrust, we measured basal, mid, and top dip angle and its spacing to the previous thrust (Fig. 3d). Shear zones were measured when they accumulated enough finite strain to have a small, visible offset. As outputs were requested every 0.5 cm of shortening, the exact moment of 'enough' finite strain is subject to a 0.5 cm uncertainty. Again, dip values were measured by the same two authors and averaged. For well-defined shear zones, the maximum difference in the measurements was 2°–3°. Thrust spacing in brittle models has been shown to depend on model thickness, thrust dip angle, and basal friction (Mulugeta, 1988; Gutscher et al., 1998; Marshak and Wilkerson, 1992; Panian and Wiltschko, 2007). In addition, for numerical continuum models thrust spacing depends on mesh resolution, with finer meshes resulting in more thrusts and smaller thrusts spacing than coarse meshes (Buiter et al., 2006). For the final stage of shortening at 10 cm, we counted the number of forward and backward shear zones as visible in the material fields. This allows a direct comparison with the number of shear zones formed in the analogue models. However, the number of numerical shear zone measurements (dip angle and spacing) may differ from the number of visible thrusts in the 10 cm material field, because some earlier thrusts that became inactive may no longer be visible at the end of the experiment. At every 0.5 cm of shortening, we computed the internal rate of dissipation of energy:

$$\dot{W}_i = \frac{1}{2}\int_A (\boldsymbol{\sigma}\cdot\dot{\boldsymbol{\varepsilon}})\, dA \tag{12}$$

the gravitational rate of work:

$$W_g = -\int_A (\rho\, g_z\, v_z)\, dA \tag{13}$$

the root-mean-square velocity:

$$v_{rms} = \sqrt{\frac{1}{A}\int_A \left(v_x^2 + v_z^2\right) dA} \tag{14}$$

and the force applied at the mobile wall:

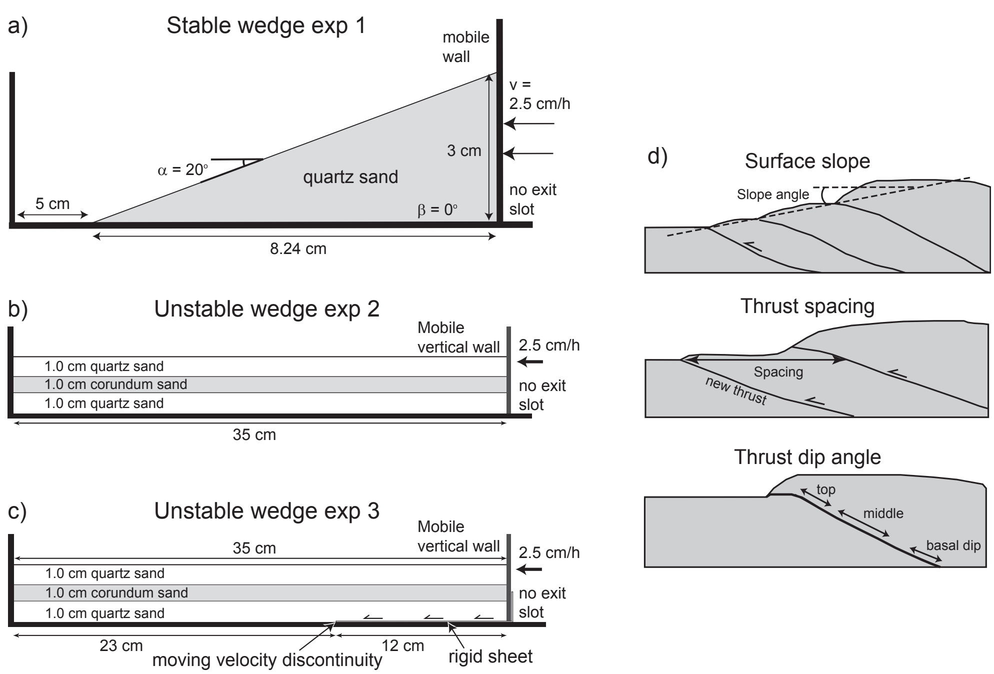

Fig. 3. Setups of the thrust wedge experiments and illustration of measurements of surface slope and shear zone parameters at deformed stages. The material properties of quartz and corundum sand are in Table 1. a) Setup of stable wedge experiment 1. A wedge of quartz sand with a surface slope of 20° is pushed with a constant velocity over a horizontal base. The mobile wall is in direct contact with the base and this corner is, therefore, a sharp velocity discontinuity. b) Setup of unstable wedge experiment 2. Three horizontal layers of quartz, corundum and quartz sand are shortened by a mobile wall which moves with constant velocity from right to left. The mobile wall is again in direct contact with the base and this corner is a sharp velocity discontinuity. This experiment should build a critically-tapered wedge. c) Setup of unstable wedge experiment 3. Three horizontal layers of quartz, corundum and quartz sand are shortened by a mobile wall which moves with constant velocity from right to left A rigid sheet is attached to the mobile wall and moves with it. The tip of the sheet at 12 cm from the mobile wall is a moving velocity discontinuity. d) Schematic illustration of the approach followed for measurements of surface slope (top), thrust spacing (middle), and thrust dip angles (bottom). Surface slope is measured as the best fitting line through the valleys (Stockmal et al., 2007) and can only be determined once 2 or more thrusts have formed. Thrust spacing is measured from a newly initiated thrust to the previously formed thrust.

$$F_x = \int_h (\sigma_{xx} \cdot n_x) \, dz \quad (15)$$

ρ is density, g_z vertical component of the gravitational acceleration, v_x and v_z the magnitude of the horizontal and vertical velocity components, and n_x the unit vector inward to the wall. Integration is over wedge area A for Eqs. (12)–(14) and over thickness h of the wedge at the backstop for Eq. (15).

3.6. Short descriptions of the participating codes

3.6.1. EEM

The Equilibrium Element Method (EEM) (used by authors Maillot and Souloumiac) determines the internal deformation and the associated stress distribution (Souloumiac et al., 2009) by an internal approach of limit analysis, which provides the lower bound on the tectonic force. The optimum stress field satisfies equilibrium and boundary conditions, and lies within the convex strength domain at every point of the material. This optimization problem relies on a spatial discretisation of the domain with triangular elements allowing stress discontinuities at their boundaries (Krabbenhoft et al., 2005). The unknowns of the problem are the stresses at the nodes. These, and the lower bound, are found through optimization (Krabbenhoft and Lyamin, 2014; Krabbenhoft and Damkilde, 2003). Basal friction is implemented as a constraint which ensures that normal and shear components of stress at each side of all nodes in contact with the base obey the Coulomb criterion. The method obtains an optimal stress field at the onset of deformation and is therefore here applied to the frictional wedge of experiment 1 only.

3.6.2. Elfen

Elfen (used by authors Albertz and Crook) is a Lagrangian finite element code which employs an elasto-plastic continuum formulation (www.rockfield.co.uk). Here Elfen is used with an explicit dynamic solution technique and a non-associated flow rule with zero dilation. An adaptive remeshing scheme is utilised where the mesh is updated if the element distortion in any part of the grid exceeds a user-defined tolerance. The element size on the new mesh depends on the spatial distribution of the plastic strain rate. The majority of the remeshing is applied locally whereas global remeshing (i.e., on the entire mesh) is performed only infrequently. This approach reduces dispersion introduced during mapping of values from the old to the new mesh. In the experiments a linear quadrilateral element is used with reduced integration and hourglass stabilization, giving linear displacement and constant stress fields. Stress integration is performed using a Green-Naghdi rate formulation and an elasto-plastic constitutive model. Explicit time integration is used with transient equilibrium obtained by defining mass-scaling that ensures that the contribution of inertia terms is negligible. The basal boundary condition is represented using a general elasto-plastic contact interaction algorithm based on the penalty method. The elastic response is governed by normal and tangential penalty coefficients and frictional sliding is represented via a Mohr–Coulomb model with zero dilation. Elfen is used for experiments 1, 2 and 3.

3.6.3. ELEFANT

ELEFANT (used by author Thieulot) is a finite element code, based on bilinear velocity and constant pressure (Q1P0) elements and a Uzawa formulation for pressure. Markers are used to track material properties and are advected by a 4th-order Runge–Kutta scheme. The direct solver MUMPS (Amestoy et al., 2001, 2006) is used to solve the large linear systems arising from the discretised equations. ELEFANT is an improvement on its predecessor FANTOM (Thieulot, 2011) (e.g., in marker advection and Uzawa pressure iterations). Viscosity is computed on the markers and arithmetically averaged per element, implying a constant viscosity value within each element. The stopping criterion for the Picard non-linear iterations is based on a normalized correlation of two consecutive velocity and pressure fields (Thieulot, 2014). Boundary friction is simulated by a layer that is one element thick/wide with boundary friction material properties. Markers that leave the frictional boundary layer are assigned the material properties of their new surroundings. ELEFANT is used for experiment 1 only because the code failed experiments 2 and 3 due to a lack of consistency of shear zone localisation with time which prevented initial shear zones to fully develop thrusts.

3.6.4. Fric2D

Fric2D (used by author Cooke) is a Boundary Element Method code that solves the equilibrium and compatibility equations of continuum mechanics (Cooke and Pollard, 1997). The code employs a linear elastic rheology and frictional slip along faults via a penalty method. Linear, constant displacement discontinuity elements are used along boundaries and faults. The code is Eulerian and large strains are simulated by iterating the infinitesimal strain solutions. Following Shackleton and Cooke (2007), the displacement field from the previous iteration determines the starting geometry of the body for the next iteration. Fault development is assessed by work minimization: Of all possible faults, the fault that grows is the one that minimizes the external work on the system (Cooke and Madden, 2014). This fault must reduce the external work more than the energy required to produce the fault. The models incorporate basal and side frictional surfaces that are one element distance (2.5 mm) inward from rigid model boundaries. Fric2D's assumption of homogeneous material properties limits the application of this code to benchmark experiment 1.

3.6.5. GALE

GALE v 1.4.1 (used by author Landry) is a particle-in-cell code from the Computational Infrastructure for Geodynamics (CIG). GALE solves the non-linear Stokes equations with a non-linear loop around a solve using Uzawa iterations. Within each Uzawa iteration, GALE uses the MUMPS direct solver for the internal preconditioning and velocity solves. The Uzawa iterations terminate when $||\nabla v||_2/||\nabla v_0||_2 < 10^{-7}$, where v_0 is a solution assuming zero pressure. The non-linear iterations terminate when $||v - v_{old}||_2/||v||_2 < 10^{-3}$. The experiments employed quadrilateral finite elements with linear shape functions for velocity and pressure. Gale uses particles to track material properties. The finite element integrals use viscosity computed using the particle locations as integration points. Boundary friction is implemented by changing the material properties (e.g., internal angle of friction) within two elements of the boundary so that they mimic the wall friction. For experiments 2 and 3, only the bottom and right sides received this treatment. The left side was held fixed. GALE is used for experiments 1, 2 and 3.

3.6.6. I3VIS

I3VIS (used by author Gerya) is a finite difference staggered grid marker-in-cell code that solves the Stokes equations for visco-elasto-plastic or visco-plastic rheologies (Gerya and Yuen, 2007). Material properties are tracked using markers and interpolated to various nodal points of the Eulerian staggered grid by using distance-dependent averaging. Viscosity is interpolated to the Gauss points using bi- (tri-)linear interpolation from the marker values. The mechanical equations are solved using the direct sparse Pardiso solver (Schenk and Gärtner, 2004, 2006) in 2-D and a geometrical multigrid solver (Gerya, 2010) in 3-D. The convergence criterion is set by prescribed levels of tolerance for the stress- and velocity-normalized residues of the Stokes and continuity equations (machine precision in 2-D and 10^{-4} in 3-D). Boundary friction is implemented through frictional contact layers which are two cells wide at the sides and two cells high at the base. Properties of markers that are displaced from the boundary layer are set to those of the ambient material. I3VIS is used for experiments 1, 2 and 3 and in addition in 3-D for experiment 2.

3.6.7. MILAMIN_VEP

MILAMIN_VEP (used by author Kaus) is a finite element code that solves the Stokes equations for visco-elasto-plastic or visco-plastic rheologies. The code is employed in a Lagrangian manner with remeshing for large deformations (every 301 steps or if elements become too distorted). The elements are quadrilateral with linear velocity shape functions and a discontinuous constant pressure shape function. Material properties are tracked using tracers. At the beginning of each time step, material properties (e.g., effective viscosity, cohesion and friction angle) are computed at integration points by arithmetic averaging from nearby particles. During non-linear plasticity iterations, the effective viscosity at an integration point is updated using the local strain-rates of that integration point. Upon remeshing, fields are interpolated back from integration points to particles and the particles are used to transfer information to the new mesh. The code uses Picard iterations and the convergence criteria is $\max(|v-v_{old}|/v) < 10^{-3}$ or a maximum number of 25 iterations. The frictional boundary condition was implemented by including a frictional layer of 1 mm thick and at least 2 elements thick. The thickness of the frictional layers is kept constant throughout the simulation, to prevent entrainment of the layer in developing faults. During the first iteration step in the plasticity algorithm and in the first time step, the maximum pressure used to evaluate the yield stress is limited to feasible stresses based on estimates from a homogeneous pure-shear setting (as described in Lemiale et al. (2008)). No erosional diffusion was employed at the free surface. MILAMIN_VEP is used for experiments 1, 2 and 3.

3.6.8. pTatin

pTatin (used by authors Le Pourhiet and May) utilises a hybrid material point, finite element spatial discretisation. The Stokes problem is formulated using the mixed Q2P1 finite element space (Brezzi and Fortin, 1991). Material lithology and history variables (e.g., accumulated plastic strain) are stored on Lagrangian material points. Effective viscosity is evaluated directly on the material points and projected onto the Gauss quadrature points using a P0 interpolant and harmonic averaging. A Newton-based method is employed to solve the non-linear Stokes problem (May et al., 2014). Non-linear iterations are terminated when the 2-norm of the initial non-linear residual has been reduced by a factor of 10^{-2}, or is less then 10^{-4}. At each non-linear iteration, the linearized Stokes problem is solved using an iterative solver, FGMRES. This solver is preconditioned with an upper block triangular matrix, which is defined in terms of a velocity solve and a pressure Schur complement solve (May et al., 2015). For low and medium resolution models, the velocity block solution is obtained using the sparse direct solver Umpfpack, for the high resolution models, geometric multigrid with four levels was used and the parallel direct solver superludist as the coarse grid solver. The frictional boundary conditions are implemented by requiring the shear traction on the interface (evaluated on Gauss quadrature points) to be proportional to the normal traction and in the opposed direction to the current displacement. If the velocity is below a threshold of 10^{-17} m s^{-1}, no shear traction is applied. No strain-softening was applied to the basal friction. pTatin is used for experiments 1, 2 and 3.

3.6.9. SDEM

SDEM (used by author Egholm) is a distinct-element (Cundall and Strack, 1979) code that integrates the movements of many discrete particles through time. The particles are circular, but vary in size. Particle interaction is by elastic repulsive forces and shear forces controlled by friction. Although the particles maintain their circular shape, they each carry a stress tensor, which reacts to the local deformation and is used for computing the forces at contact points between particles (Egholm, 2007). The stress tensors enable SDEM to be parameterized by macroscopic properties such as the angle of internal friction and cohesion. Boundary conditions are implemented by the use of rigid walls that can move. Boundary friction is controlled through the friction coefficient of these walls. Because of the discrete structure of the method, granular properties such as dilation and force chains are implicitly captured by SDEM. Force chains develop by propagation of particle contacts forces, and they are important for capturing the micro-scale mechanics of granular materials (e.g. Majmudar and Behringer (2005)). The increased size of SDEM particles compared to real sand grains must, however, be expected to exaggerate the influence of the force chains for generating stress heterogeneities at the larger scale of the sandbox modelled here. SDEM is used for experiments 1 and 2.

3.6.10. Sdvig

Sdvig (used by author Mishin) is a MATLAB-based finite element code that solves the Stokes equations on an Eulerian finite element grid that deforms in the horizontal direction. Material properties are carried by Lagrangian particles. The elements are quadrilateral with quadratic velocity shape functions and linear discontinuous pressure shape functions. The friction boundary is implemented via particle transmutation: friction boundary properties are used for particles near the boundaries. The friction boundary is 0.06 cm thick in experiment 1, and 0.1 cm thick in experiments 2 and 3. The convergence velocity is increased gradually for 10–50 iterations before the start of actual convergence. A normalized L2 norm of the velocity change is used as a non-linear convergence criterion. The threshold value is 10^{-3} and maximum 25 non-linear iterations are performed per time step. Viscosity is computed per element as an arithmetic average of values carried by corresponding particles. Sdvig is used for experiments 1, 2 and 3.

3.6.11. SOPALE

SOPALE (used by author Buiter) is an arbitrary Lagrangian Eulerian finite-element code that solves the equation of conservation of momentum in an incompressible formulation. It employs quadrilateral elements with linear shape functions for velocity and discontinuous constant pressure. Pressure P is computed as mean stress through the penalty method: $P = -k\nabla\cdot\boldsymbol{u}$. k is the penalty factor (with dimension of viscosity) and $\boldsymbol{u}$ is the velocity. A true free surface is obtained by a slight vertical adjustment of the Eulerian mesh to accommodate surface displacements (Fullsack, 1995). A very small amount of diffusive erosion and sedimentation with diffusion coefficient 10^{-9} m^2 s^{-1} is applied at the surface to mimic the sliding of sand grains along steep slopes in the analogue models. Material properties are tracked by particles and assigned to an element based on the majority of particles of a certain material present in that element. The convergence criteria is $\max|v-v_{old}|/v_{scale} < 5 \times 10^{-3}$, with v_{scale} the applied wall velocity. The mechanical equations are solved using the sparse Cholesky solver BLKFCT (developed by Ng and Peyton of Oak Ridge National Laboratory). Boundary friction is implemented through the use of frictional contact layers which are four elements wide at the sides and four elements high at the base. Particles that leave the frictional layer are deleted. SOPALE is used for experiments 1, 2 and 3.

4. Experiment 1

4.1. Experiment 1: model setup and analytical solutions

Experiment 1 tests whether model wedges in the stable domain of critical wedge theory remain stable when translated horizontally (Fig. 2a). A quartz sand wedge with a horizontal base ($\beta = 0°$) and a surface slope of $\alpha = 20°$ is pushed horizontally by inward movement of a mobile wall with 2.5 cm h^{-1} (Fig. 3a, Table 1). This experiment should not result in internal deformation and the surface slope should remain at 20°. Eleven codes run this experiment (Table 2).

For a wedge that is translated in a stable manner, we can derive analytical solutions for the parameters that we use to quantify wedge behaviour. Because no internal deformation occurs, strain-rate is zero and the rate of dissipation of internal energy $\dot{W}_i = 0$. This is not completely true if a basal shear zone builds in the wedge just above the basal boundary. In that case, $\dot{W}_i$ would be on the order of 2×10^{-5} W m^{-1} (using a simple analytical calculation of Eq. (12) for effective strain-rate and shear stress in a shear zone with $\varphi = 36°$, $C = 30$ Pa, $\rho = 1560$ kg m^{-3}, and $V = 2.5$ cm h^{-1}). Surface slope does not change and, therefore, the gravitational rate of work $\dot{W}_g = 0$. Root-mean-square velocity v_{rms} is equal to the applied velocity of 6.9444444×10^{-6} m s^{-1}. The applied force can be derived from $F_a = 0.5\,\rho\,g\,A\,tan(\phi_b) + C_b L = 7.9$ Nm^{-1} (using area A = length L (8.24 cm) × height h (3 cm), $\phi_b = 16°$, $C_b = 30$ Pa, and $\rho = 1560$ kg m^{-1} (Table 1)).

4.2. Experiment 1: results

The results of the eleven codes that run this experiment are visualised by their material field (Fig. 4), pressure field (Fig. 5), and strain-rate field (Fig. 6) after 4 cm of translation. All experiments maintain their initial surface slope and do not show obvious internal deformation (Fig. 4). However, in detail, several of the wedges show deformation at their toes. GALE and Sdvig have a slight amount of sand moving up into the sticky air. This is possible because the air viscosity in the experiments is prescribed as 10^4 Pa s, implying a sand falling velocity which is too low (ca. 10^{-8} m s^{-1}) on the time-scale of the numerical experiment for sand to fall back to the base. SOPALE has a small amount of accretion at the wedge toe. These results illustrate the difficulty of maintaining a sharp wedge toe during translation over a frictional boundary.

A stable wedge that experiences no forces apart from gravity is expected to have a lithostatic internal pressure field. EEM, ELEFANT, I3VIS, pTatin, and SOPALE show a pressure field that approaches lithostatic values also after 4 cm of shortening (Fig. 5). The pressure field of the other codes does not show a clear pattern. The strain-rate field visualises incipient shear zones for Elfen, MILAMIN_VEP and Sdvig, which do, however, not lead to finite deformation over the duration of the experiment (Fig. 6). ELEFANT, GALE, I3VIS, pTatin, and SOPALE have zero strain-rate (except for toe deformation of ELEFANT and SOPALE), as expected for this experiment. None of the models form a shear zone within the wedge just above the base and simple shear is accommodated by the frictional basal boundary condition in all models.

The internal rate of dissipation of energy and the gravitational rate of work (Eqs. (12) and (13)) show variability among the codes, but the values are all small and close to the zero analytical prediction (Fig. 7a,b and Table A.5 in Appendix A). The root-mean-square velocity over the sand domain (Eq. (14)) shows variability in the initial stages, but all values converge to the analytical solution (Fig. 7c). The force that is applied by the mobile wall is more or less constant for most models, as is to be expected for a translating wedge, but large differences occur in the force magnitude (Eq. (15), Fig. 7d). The laboratory of Cergy-Pontoise (authors Maillot and Souloumiac) measured the applied force in their sandbox experiment as 10.7 N m^{-1}. This is higher than most numerical values, because there is an additional friction of the analogue sand wedge on the two side walls of the box, whereas there are no side walls in the 2-D numerical simulations. The variations in magnitude of the applied force in experiment 1 may point to variations in the effective boundary friction between models, related to the different boundary friction algorithms that are used in the experiments.

4.3. Experiment 1: discussion

All models pass the stable wedge test, but some differences between the models are apparent. The SDEM model shows distributed internal strain-rates of moderate magnitude that may be related to particle motions (Fig. 6). Continuum models (FDM, FEM) approximate the discontinuous assembly of sand grains with an averaging continuum approach. For these models, a translating wedge will have zero vertical velocity and the root-mean-square velocity therefore equals the velocity that is applied by the mobile wall. However, in the sandbox models sand grains may not only experience horizontal translation, but could also undergo some vertical motion as grains move relative to each other. These small

Table 2
Numerical parameters for experiment 1.

Code	Method[a]	Elements (horz × vert)	Tracers	Domain size (excl bound.) (cm)	Basal bc	Air	Elasticity[b] E (Pa)	Diffs wrt description
EEM	EEM	2523	–	8.24 × 3.00	friction	no		$\varphi = 36°$, $\phi_b^p = \phi_b^s = 15°$
ELEFANT	FEM	400 × 100 Q1P0	4,000,000	13.24 × 3.20	layer	yes		
Elfen	FEM	2349	–	8.24 × 3.00	friction	no	5e6	$\phi_b^p = \phi_b^s = 15°$
Fric2D	BEM	181	–	8.24 × 3.00	friction	no	200	no softening, Δ t = 36s
GALE[c]	ALE	256 × 64 Q1P0	491,520	13.24 × 3.00	layer	yes		$\eta_{air} = 1$ Pa s
I3VIS	FDM	265 × 60	1060 × 240	13.24 × 3.00	layer	yes		
MILAMIN_VEP[d]	FEM	240 × 60 Q1P0	2416 × 302	13.24 × 3.00	layer	yes		$\eta_{air} = 10$ Pa s, $\rho_{air} = 10$ kgm^{-3}
pTatin	FEM	256 × 64 Q2P1	262,144	13.24 × 3.00	friction	yes		Δ t = 36s, $\phi_b^p = \phi_b^s = 15°$
SDEM	DEM	ca. 2000 ptcl	–	8.24 × 3.00	layer	no		
Sdvig	FEM	212 × 64 Q2P1	29,266	13.24 × 3.00	layer	yes		
SOPALE[e]	ALE	331 × 75 Q1P0	994 × 226	13.24 × 3.00	layer	no		

[a] ALE = Arbitrary Lagrangian Eulerian, BEM = Boundary Element Method, DEM = Distinct Element Method, EEM = Equilibrium Element Method, FDM = Finite Difference Method, FEM = Finite Element Method.
[b] The models have no elasticity, unless a value for Young's Modulus E is given.
[c] GALE has a pre-existing boundary layer of one cell high along the entire base of the model, also in front of the wedge.
[d] MILAMIN_VEP smooths the velocity discontinuity between mobile wall and base over one element (0.5 mm)
[e] SOPALE includes a thin layer of sand (0.05 mm thickness) in front of the wedge.

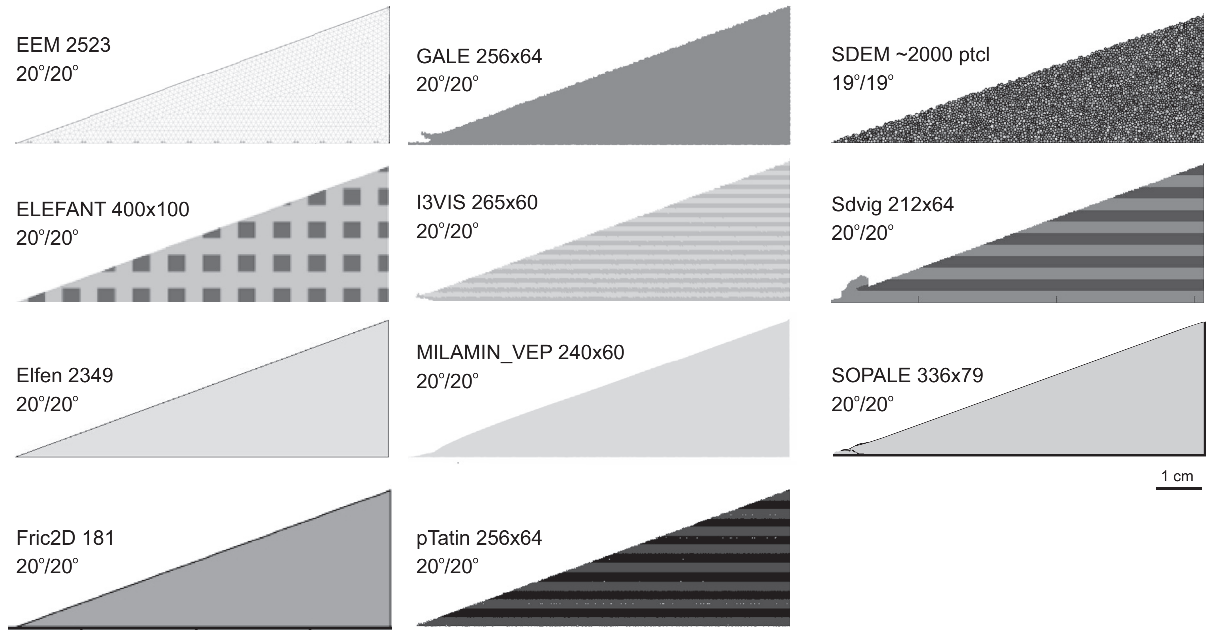

Fig. 4. Results of experiment 1 after 4 cm of shortening depicted by material fields. Resolution in terms of the number of elements or particles in the entire model domain is shown with the model names. The numbers under the model names are the values for surface slope at 0 and at 4 cm of shortening.

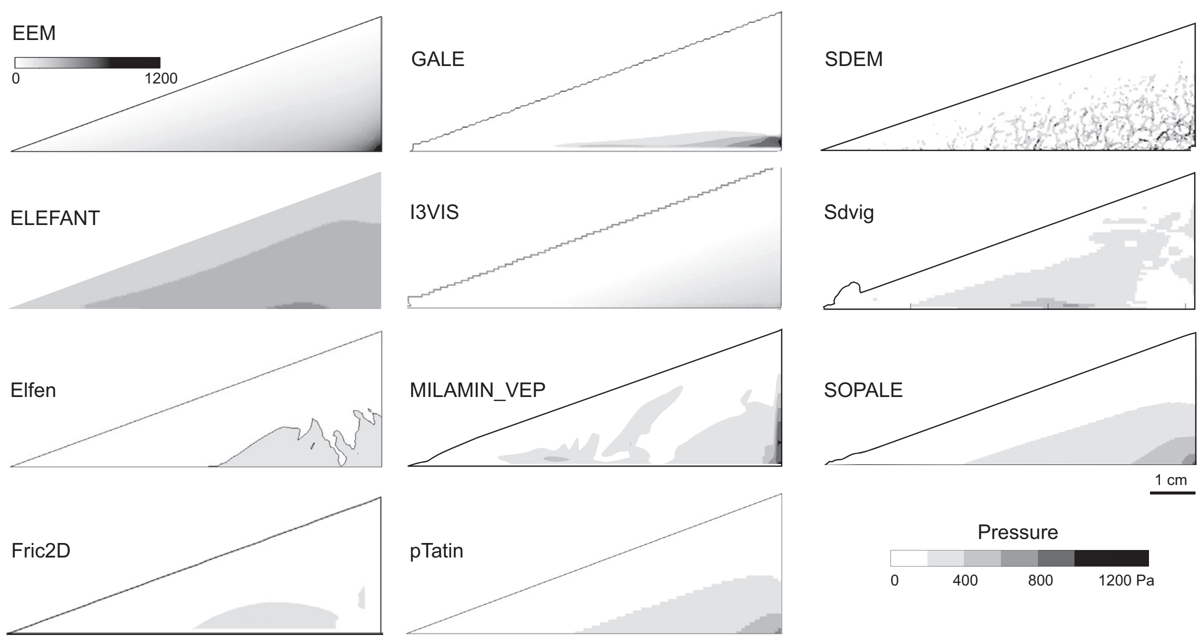

Fig. 5. Pressure fields of experiment 1 after 4 cm of shortening.

vertical motions could influence the internal strain-rates and root-mean-square velocity of sandbox models at specific measurement times. We do not have root-mean-square velocity measurements of sandbox experiments to compare our numerical values against and, as far as we are aware, the behaviour of sand grains in a volume of sand that is translated (and not deformed) has not been investigated in detail. The distinct-element model (SDEM) results indicate that particles experience some vertical motions during wedge translation, but that these mainly average out for this setup.

The sticky-air layer seems to have had no noticeable influence on the experiments as no systematic difference is detected between codes that employed an air layer (ELEFANT, GALE, I3VIS, MILAMIN_VEP, pTatin, and Sdvig) and those that did not (EEM, Elfen, Fric2D, SDEM, SOPALE).

5. Experiment 2

5.1. Experiment 2: model setup

The second experiment tests how an unstable subcritical wedge deforms to reach the critical taper solution (Figs. 2a and 3b). The model is built of three horizontal layers of quartz-corundum-quartz

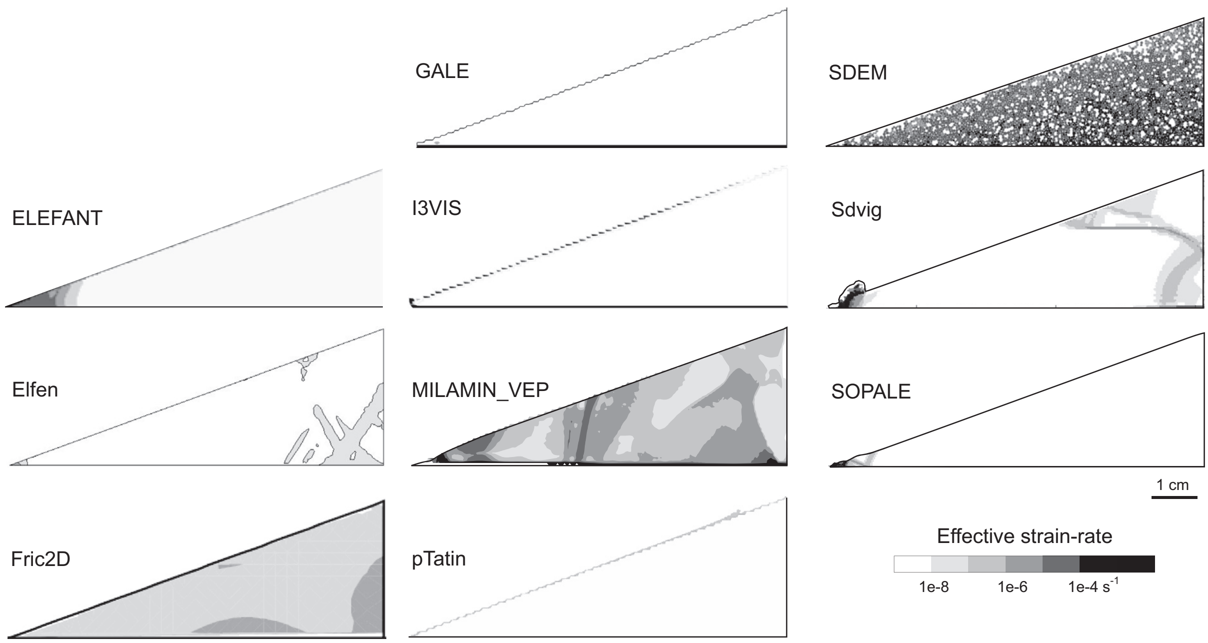

Fig. 6. Strain-rate fields of experiment 1 after 4 cm of shortening.

sand which are shortened by a mobile wall which moves into the model domain with 2.5 cm h^{-1}. The initial surface slope is 0° and basal slope remains at 0° throughout the experiment. The critical taper value for our wedge varies with peak strength, stable strength, and cohesion (Fig. 2). Lohrmann et al. (2003) infer that the strength of wedge segments at critical taper values is controlled by the frictional strength of faults that have reached dynamic stable strength (Fig. 2c). Following this argument, the low critical taper value for our wedge would be 4.8° if the material is cohesionless and 4.1° for depth-dependent cohesion. The corresponding high critical taper values are 29.2° and 36.8°, respectively.

Eight codes run this experiment (Table 3), each at 2 or 3 different resolutions. Basal friction follows values for quartz sand on foil (Table 1), whereas all codes also used the boundary friction for quartz sand on foil for the front- and backwalls, ignoring the alternation of quartz-corundum-quartz sand as far as boundary friction is concerned.

5.2. Experiment 2: results

Experiment 2 builds a thrust wedge through a combination of mainly in-sequence forward and backward thrusting (Fig. 8). Deformation starts by forming a pop-up structure near the mobile wall, though the forward thrust of the pop-up is more pronounced than the backward thrust in the results of MILAMIN_VEP and SOPALE. With increasing shortening, some models deform in a style of in-sequence pop-ups (e.g., GALE), whereas others focus deformation on forward shear zones (e.g., SOPALE). Decrease or increase in resolution leads to changes in the location of shear zones, the number of shear zones, and their width, as expected for these numerical methods because plasticity is resolution-dependent (Fig. 9). However, overall the results of the individual codes do not change indicating that to first-order the results have converged. The strain (Fig. 10a, b) and strain-rate (Fig. 11) fields highlight several incipient shear zones that do not always accumulate enough offset to become visible in the material field. The pressure field of the models remains more or less lithostatic, with lower pressure values in (incipient) shear zones (Fig. 10c, d). The pressure field of the SDEM model is highly heterogeneous, which reflects the importance of discrete force chains for transmitting stress in a granular assembly. I3VIS shows incipient distributed faulting in its pressure field over the entire width of the model domain.

The surface slopes of the 2-D numerical models converge towards the critical taper value for both deformation styles (dominated by either forward thrusts or pop-ups) (Fig. 12a, Fig. 13, Table A.7). The oscillations in surface slope are caused by steepening of the slope before a new thrust forms and shallowing once the new in-sequence thrust breaks through. These oscillations are especially apparent for the initial stages with few thrusts, but reduce once more thrusts have formed. The Sdvig models do not form well-localised shear zones, but rather broad folds, and surface slope could not be measured for these models. Because the SDEM models form a second pop-up only at late evolution stages with shortening in earlier stages being accommodated by thrusting near the backwall, surface slope measurements have not been made for these models.

Theoretical shear zone dip angles for Roscoe, Arthur, and Mohr–Coulomb (Eqs. (8)–(10)) are relative to σ_1. For initial thrusts, σ_1 will be more or less horizontal, but for a critically tapered wedge of our material properties, σ_1 makes an angle of 6° with the horizontal. This implies that we could expect the dip angle of forward shear zones to decrease with thrust number, while backward thrust dips would increase with thrust number. Such a trend is, however, not visible in Figs. 14 and 15. Forward thrusts tend to be listric, with increasing dip angle upwards (Fig. 14, Table A.8). The bottom dip angles tend towards Mohr–Coulomb angles, the middle dip angles lie between Mohr–Coulomb and Arthur angles, whereas the top dip angles are closer to the Arthur angle with spreads towards Mohr–Coulomb and Roscoe angles. The majority of the dip angles lie within the theoretically admissible range of Mohr–Coulomb to Roscoe dip angles.

The dip angles of backward thrusts tend to be steeper than the forward thrust dip angles (Fig. 15) and have less tendency for listric thrust shapes. Initial backward thrusts have approximately Roscoe dip angles. Later thrusts show approximately Roscoe dip angles if σ_1 were horizontal, but lie between Arthur and Roscoe dip angles when compared to the case of rotated σ_1 as expected in critical tapers. Initial backward thrusts, and sometimes the first 2–3

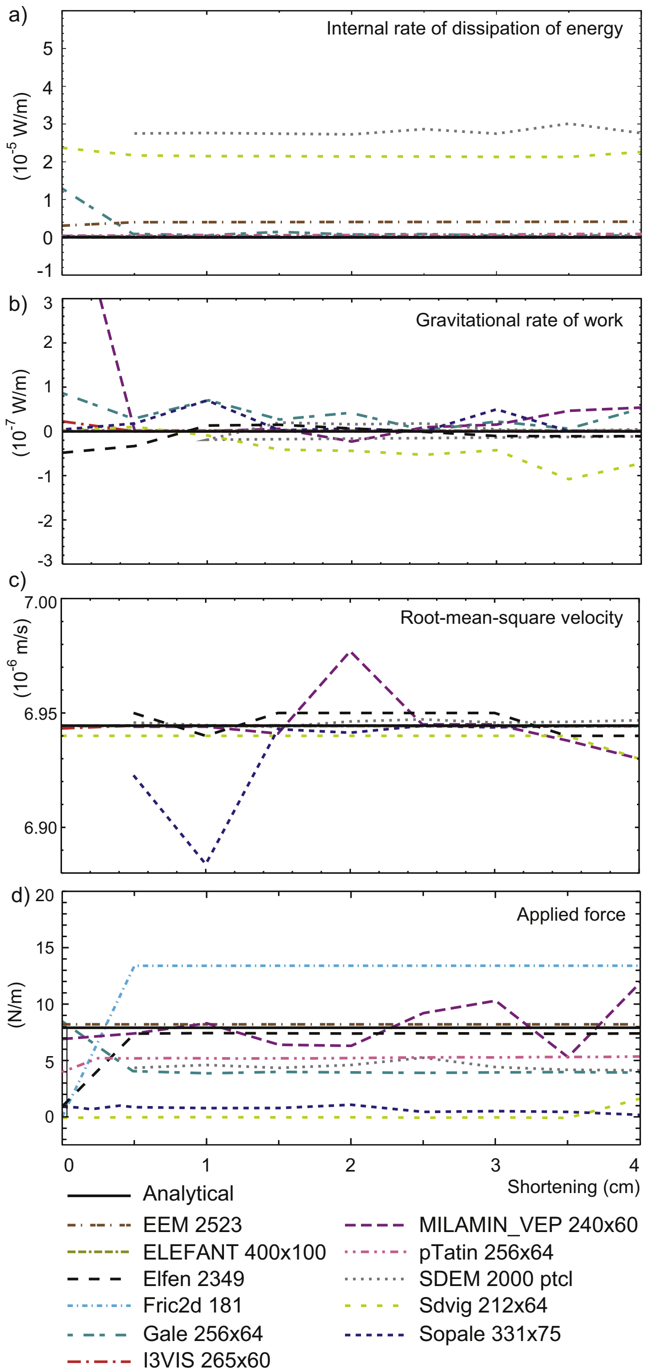

Fig. 7. a) Internal rate of dissipation of energy, b) gravitational rate of work, c) root-mean-square velocity, and d) applied force versus shortening for experiment 1.

backward thrusts as well, are located near the mobile wall (Fig. 8). This could perhaps influence thrust dip angle in comparison with backward thrusts that form away from the mobile wall, but a trend indicating such a potential influence is not visible in Fig. 15.

More forward thrusts form with increasing amount of shortening, as can be expected for a deforming brittle thrust wedge, but the rate of thrust formation differs substantially between the models (between ca. 0.3–0.9 thrusts/cm shortening) (Fig. 16a, Table A.9). Thrust spacing of newly formed forward thrusts to the previously formed forward thrust shows a large variation (Fig. 16b). Large thrust spacings occur when deformation steps far outward, typically observed when a pop-up structure forms in front of the wedge (e.g., GALE just before 6 cm of shortening (Fig. 8)). The number of forward shear zones at 10 cm of shortening tends to be higher than the number of backward thrusts (Table A.9). The I3VIS models have the largest number of thrusts.

All models show an increase in root-mean-square velocity v_{rms} with increasing shortening (Fig. 17c). This reflects a larger part of the model domain being incorporated into the wedge as the wedge grows towards its critical taper. Because deformation does not reach the leftmost boundary in most models, not all of the model domain is participating in the thrust wedge and v_{rms} at 10 cm of shortening is below the value of the applied velocity. v_{rms} of distinct element model SDEM is about an order of magnitude higher than the values of the continuum models (Table A.6). The distinct element method works by time-integrating particle accelerations caused by disequilibrium forces. This process inevitably involves small velocity oscillations that partially cancel out when summed, but nevertheless contribute to the value of v_{rms}. This is also reflected in the values for the rate of dissipation of energy and the gravitational rate of work. The internal rate of dissipation of energy varies with a factor of about two between the continuum models (Fig. 17a and Table A.6). The gravitational rate of work increases with shortening and then fluctuates around ca. 10^{-4} Wm^{-1} (Fig. 17b), reflecting the building of topography towards the critical taper value (Fig. 12a). The applied force could not be measured for all models. For the four codes that provided force measurements, the applied force increases with the amount of shortening, which is to be expected for a wedge that grows in height.

5.3. Experiment 2: 3-D wedge models

Many published numerical thrust wedge models so far are 2-D as accurate simulation of brittle behaviour with thrust formation requires a high spatial resolution (ca. 1 mm node spacing) which is challenging to achieve. For this reason, only few numerical investigations of 3-D brittle wedges exist so far (Ruh et al., 2013). Here we present two 3-D models computed with I3VIS with a lateral width of 9 cm and 18.6 cm (Fig. 18). The lateral sides are held fixed and the friction along the lateral walls causes the surface strike of thrusts to become convex with respect to the mobile wall

Table 3
Numerical parameters for experiment 2.

Code	Method	Elements	Tracers	Basal bc	Air	Elasticity[a]	Diffs wrt description
Elfen	FEM	14700–15100	–	friction	no	E = 5e6 Pa	$\phi_b^p = \phi_b^s = 15°$
GALE	ALE	256 × 64 Q1P0	491,520	layer	no		left side fixed, variable Δt
I3VIS	FDM	350 × 60	1400 × 240	layer	yes		variable Δt
MILAMIN_VEP	FEM	350 × 60 Q1P0	6946 × 302	layer	no		
pTatin	FEM	256 × 64 Q2P1	262,144	friction	no		Δ t = 36s, $\phi_b^p = \phi_b^s = 15°$
SDEM	DEM	87936 ptcl	–	layer	no		
Sdvig	FEM	350 × 70 Q2P1	94,500	layer	yes		Δ t = 14.4 s
SOPALE	ALE	350 × 60 Q1P0	1049 × 171	layer	no		

[a] The models have no elasticity, unless a value for Young's Modulus E is given.

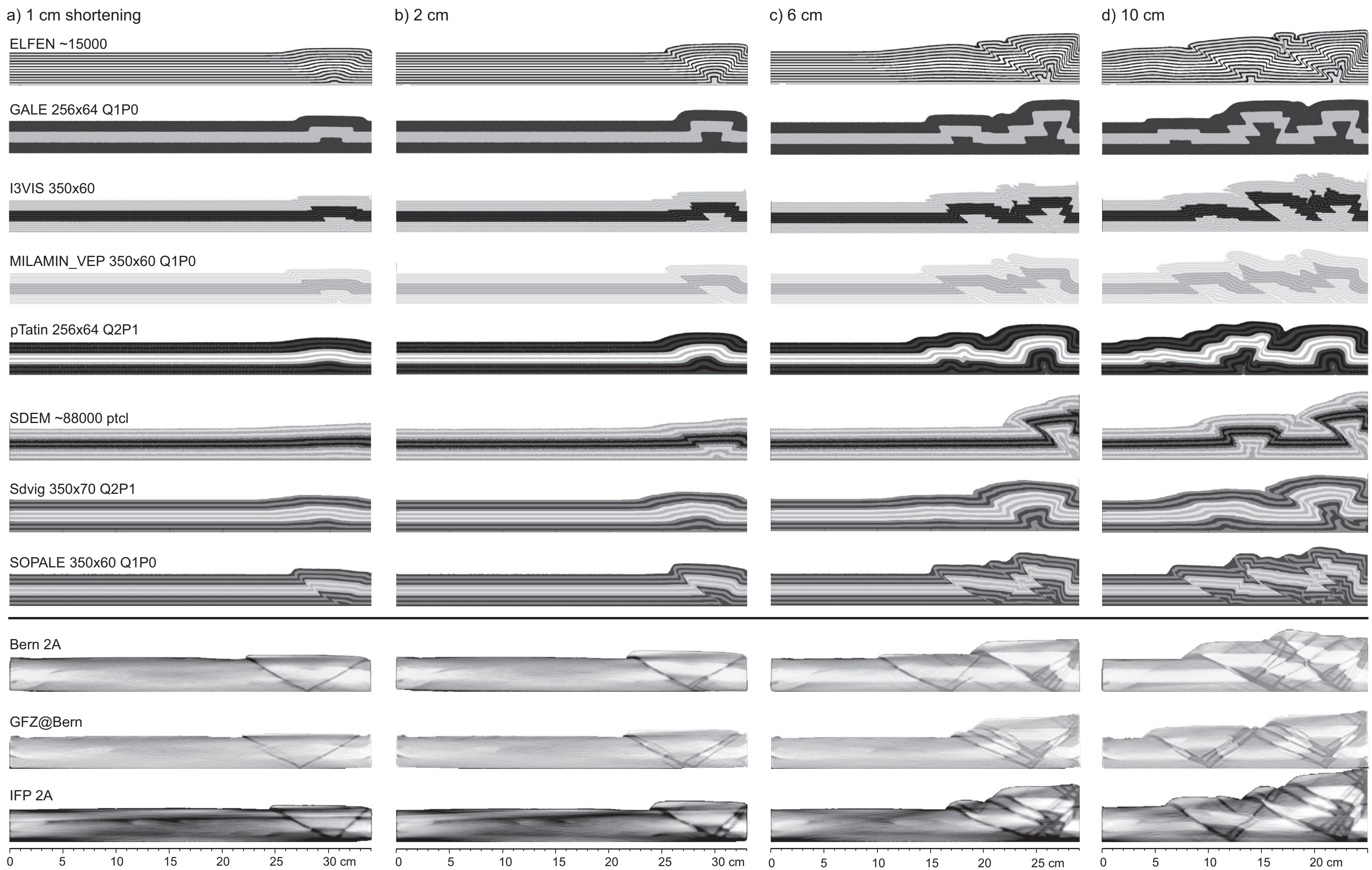

Fig. 8. Material fields of experiment 2 after 1, 2, 6 and 10 cm of shortening for 8 numerical models. Resolution in number of elements or particles is shown with the model names. Wedge formation initiates with a pop-up structure near the mobile wall and continues with in-sequence formation of forward thrusts and backward thrusts. Results of the analogue laboratories of the University of Bern and IFP (as imaged in an X-ray computer tomographer) from Schreurs et al. (2016) shown below.

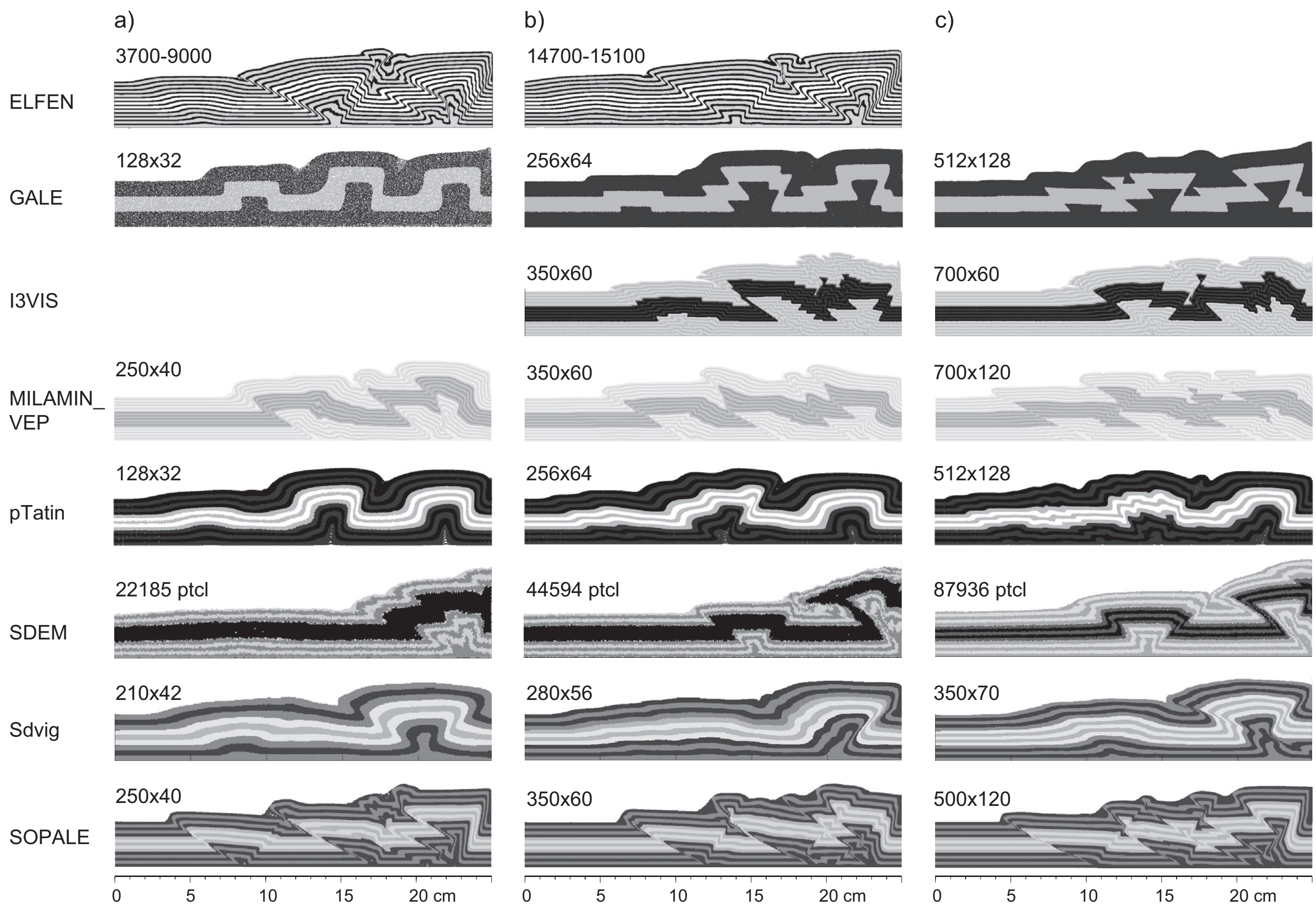

Fig. 9. Material fields at 10 cm shortening for experiment 2 at different resolutions.

(Schreurs et al., 2006; Cubas et al., 2010; Souloumiac et al., 2012).

Surface slope in 3-D push experiments is higher near frictional side walls than towards the centre of the model (Fig. 18). The curved surface strike of the thrusts of the 9 cm wide model (Fig. 18a,c) indicates that the model is influenced by the frictional side walls over its entire model width. This agrees with observations of Cubas et al. (2010) who found that the influence of lateral walls in their quartz sand wedge model disappears at ca. 8 cm from the lateral walls (their φ is 33° softening to 30°, $\phi_b \approx 7.5°–10°$ and $C_b \approx 10$ Pa). A model of 9 cm wide would thus be entirely influenced by the lateral boundaries. Surface slope measured on a centre section, however, still lies within the range of analogue surface slope measurements (Fig. 12b).

5.4. Experiment 2: numerical-analogue comparisons

A comparison of the numerical and analogue thrust wedges at 10 cm of shortening shows that the models deform either in a style dominated by pop-ups, each formed by a forward and a backward thrust (e.g., Elfen, GALE, Buenos Aires, Cergy-Pontoise), or in a style dominated by forward thrusts (e.g., MILAMIN_VEP, SOPALE, Bern, IFP, Parma) (Fig. 19). These two modes of deformation occur in both analogue and numerical models. In section 5.5 we speculate that the modes may be caused by variations in effective basal friction. Taking this into account, Fig. 19 first of all shows an encouraging overall agreement in thrust wedge formation, highlighting that both methods capture the essential aspects of internal deformation by forward and backward thrusting. However, variability among the models occurs related to the two modes of deformation and further differences are apparent in surface slope, number of shear zones, the degree of localisation of shear zones (e.g., Sdvig), and shear zone dip angles. In fact, the variability among the models could be said to be larger than would be expected for the strict setup defined for this experiment. For the analogue laboratories this may point to intrinsic variability due to model building (e.g., sieving of sand into the model apparatus) or sand storage conditions (e.g., humidity). For the numerical models, the differences may be caused by differences in numerical solution technique, resolution, and/or the implementation of boundary friction.

Surface slope evolution was measured through the centre of the 5 analogue models that were monitored in an X-ray computer tomographer (Fig. 12b) (Schreurs et al., 2016). In addition, Fig. 13 compares surface slopes at 10 cm shortening for 14 analogue laboratories (1–2 experiments per laboratory) with the corresponding surface slopes of 6 numerical codes at 1–3 different resolutions. Whereas the 2-D numerical models converge towards the critical taper value, the analogue models overall do not. The reason for this is unclear, but we speculate that analogue models could need more shortening before a critical taper value is reached. This might be related to shortening partly being taken up by compaction in analogue models, but we do not expect that this would postpone reaching the critical taper by several cm of shortening. An alternative explanation may be found in the observation that the numerical models tend to form more forward thrusts than the analogue models at similar amounts of shortening (Table A.9). As a wedge at critical taper is built by thrusts, models with an increased

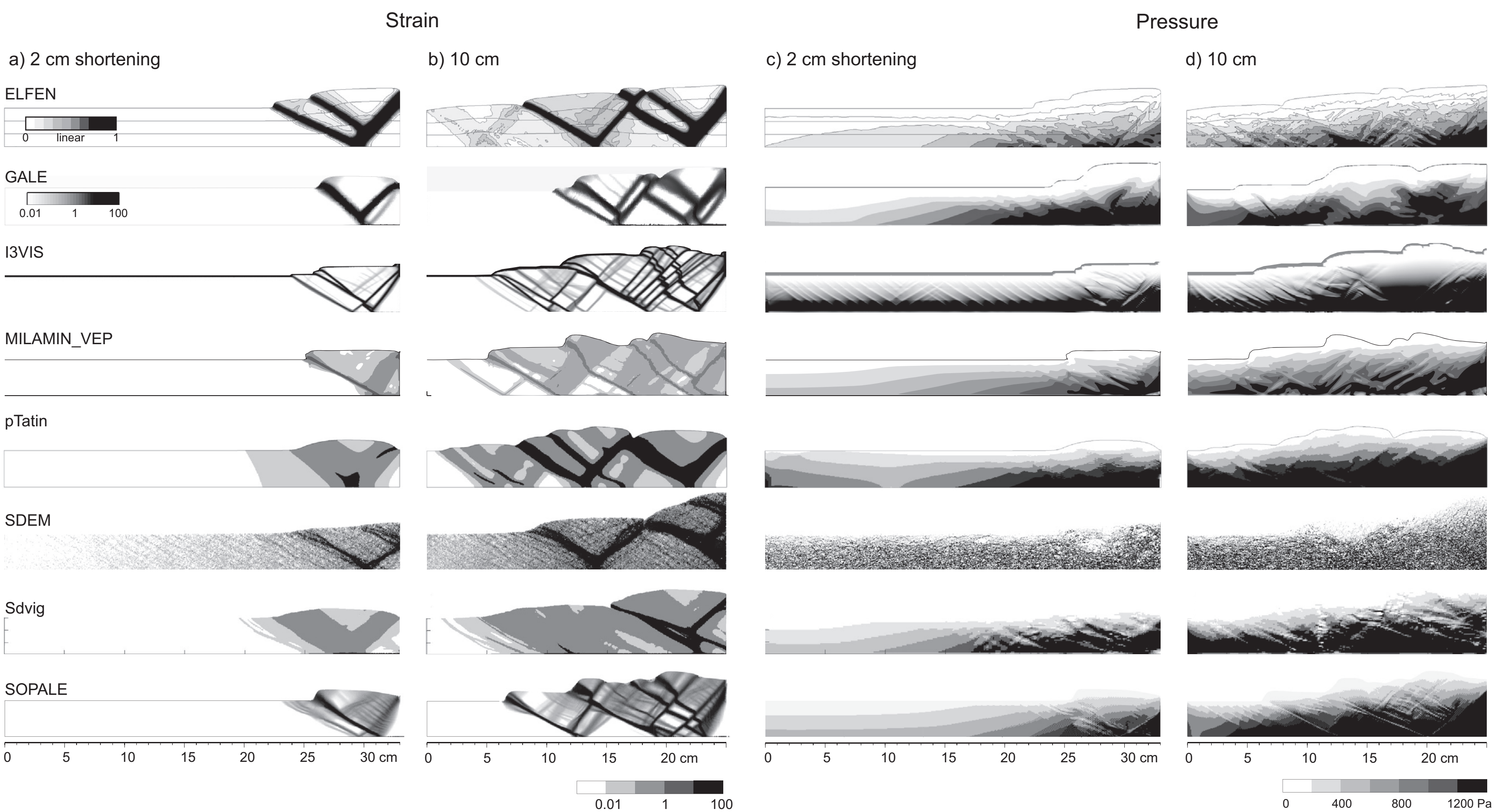

Fig. 10. Finite strain fields (measured as second invariant of the strain tensor) and dynamic pressure (mean stress) fields of experiment 2 after 2 and 10 cm of shortening. The models are shown at the same resolution as in Fig. 8.

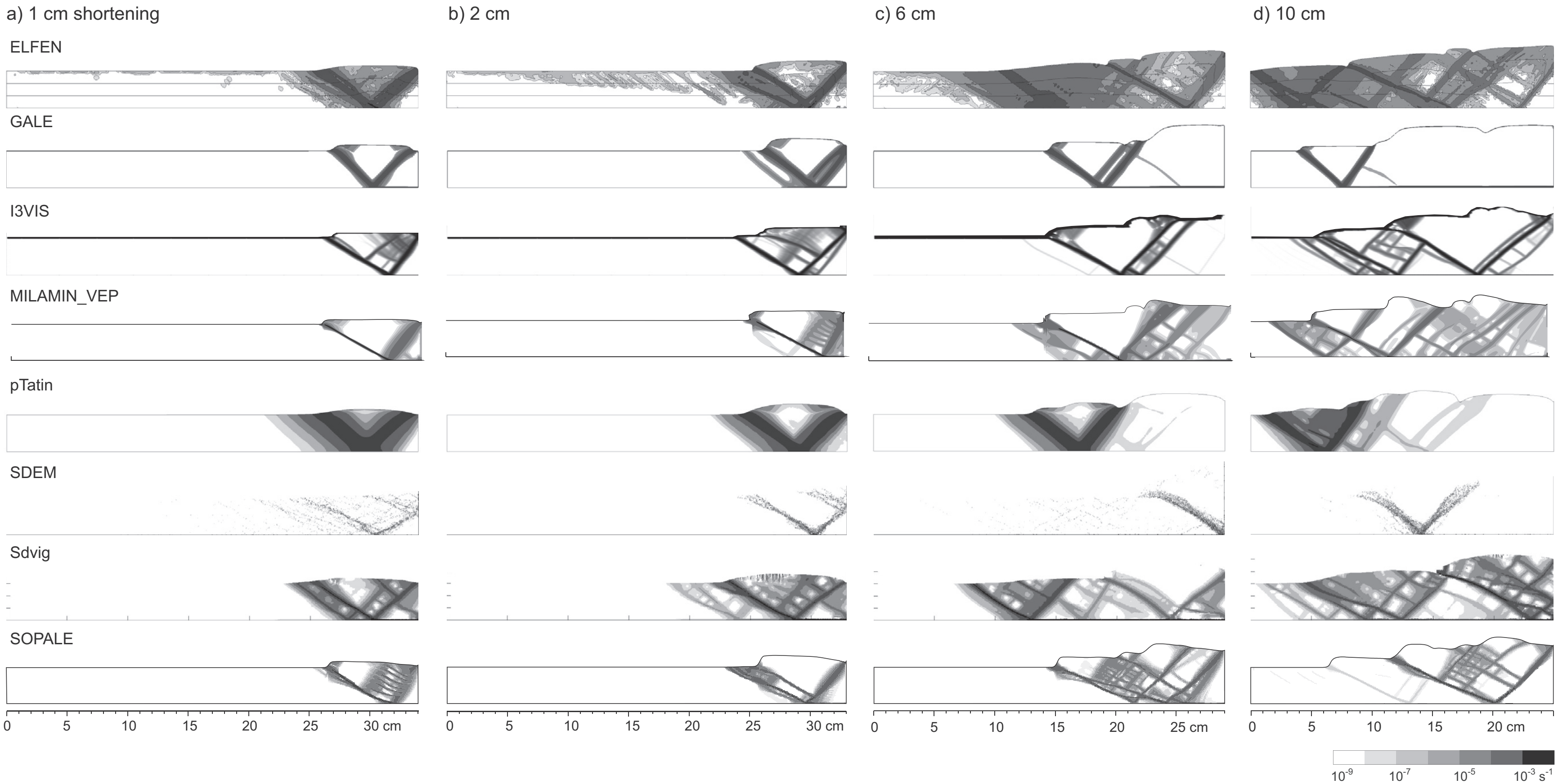

Fig. 11. Strain-rate fields of experiment 2 after 1, 2, 6 and 10 cm of shortening. The models are shown at the same resolution as in Fig. 8.

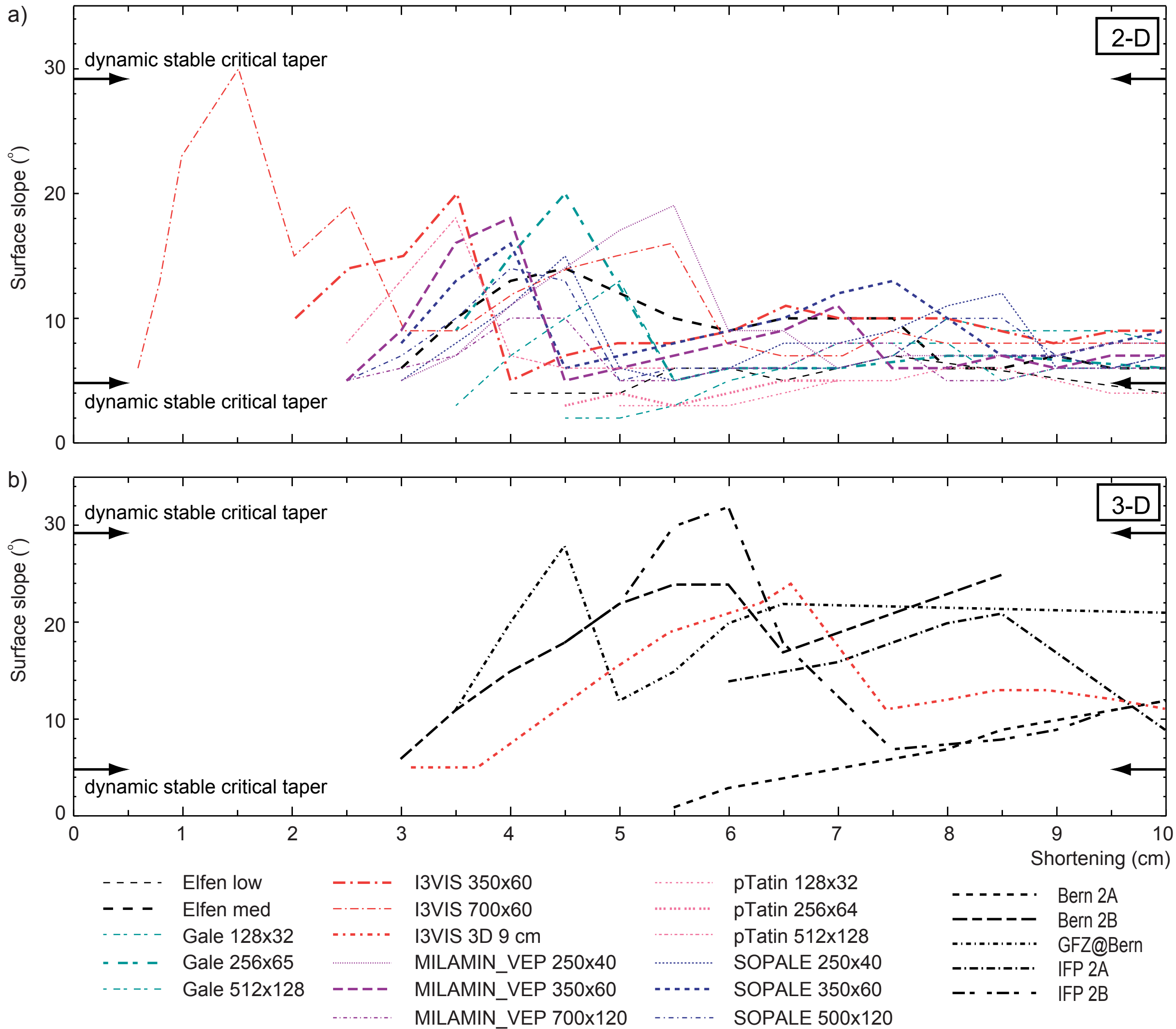

Fig. 12. Surface slope against shortening for experiment 2. Surface slope is measured as the best visual fit line through the valleys of the thrusts (Fig. 3d). a) 2-D numerical surface slope values converge towards the lower critical taper value of 4.8° (computed for $\varphi = 31°$, $\phi_b = 14°$, $\beta = 0°$, and $C = C_b = 0$ Pa). The numerical results are shown for up to three different resolutions (Table A.7). b) A comparison of the 3-D numerical surface slope values to the values of five analogue experiments that were analysed in an X-ray computer tomographer (Schreurs et al., 2016). Slope values for the 3-D numerical and analogue models are measured for a section through the centre of the model. Up to two experiments per analogue laboratory are shown.

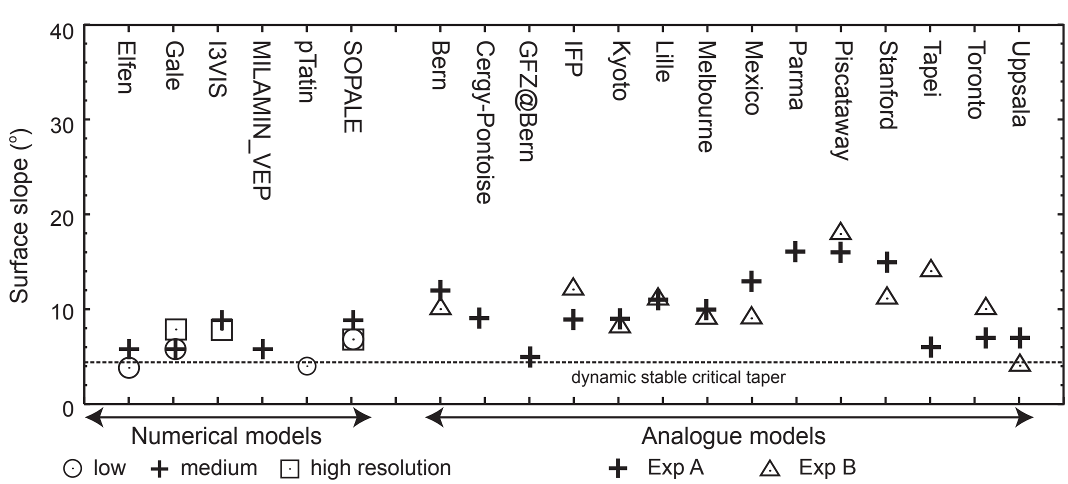

Fig. 13. Surface slope at 10 cm shortening for numerical and analogue models for experiment 2. The results of the numerical experiments are shown for up to three different resolutions (Table A.7). The analogue results (Schreurs et al., 2016) are for sections through the middle of the experiment and show up to two experiments per laboratory.

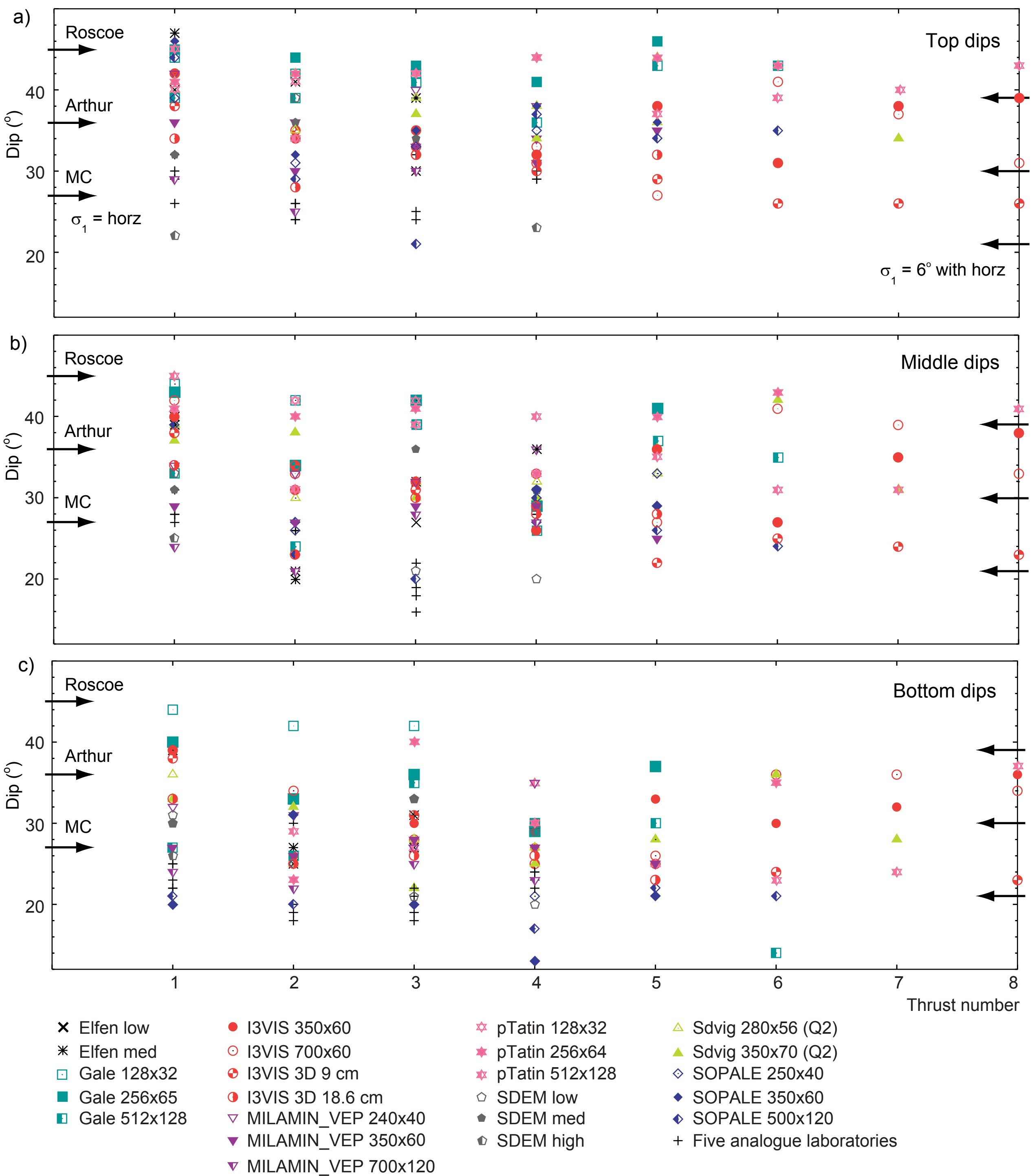

Fig. 14. Dip angles of forward shear zones for experiment 2. Dip angles were measured for each thrust when the thrust just formed and accumulated enough offset to be visible on finite strain plots and as a small surface topography (Fig. 3d). Theoretical shear zone dip angles with σ_1 for Roscoe, Arthur, and Mohr–Coulomb (MC) (Eqs. (8)–(10)) are indicated with arrows. Initially, σ_1 is horizontal, resulting in the theoretical dip angles indicated at the left side of the graphs. For a critical tapered wedge with our material properties, σ_1 makes an angle of 6° degrees with the horizontal. The theoretical dip angles for this situation are indicated at the right side of the graphs. For each experiment up to 3 different resolutions are shown. The analogue results are from Schreurs et al. (2016). a) Top dip angles, b) Middle dip angles, and c) Bottom dip angles.

number of thrusts may reach a critical taper more quickly. Analogue and numerical wedge models that employ a setup in which a layer of brittle material is pulled towards a backstop (conveyor belt or pull setup), instead of pushed, usually have shortening by 10s of cm and may thus be better posed for reaching criticality (Stockmal et al., 2007; Lohrmann et al., 2003) (provided 3-D model width is large enough to overcome effects of lateral wall friction). The number of backward thrusts is comparable between analogue and numerical models (Table A.9). Also the rate of forward thrust formation and thrust spacing of numerical and analogue models overlap (Fig. 16).

The dip angles of forward thrust zones in the numerical models are higher than the dip angles of the analogue models (Fig. 14). The analogue dip angles are Mohr–Coulomb or lower, whereas the

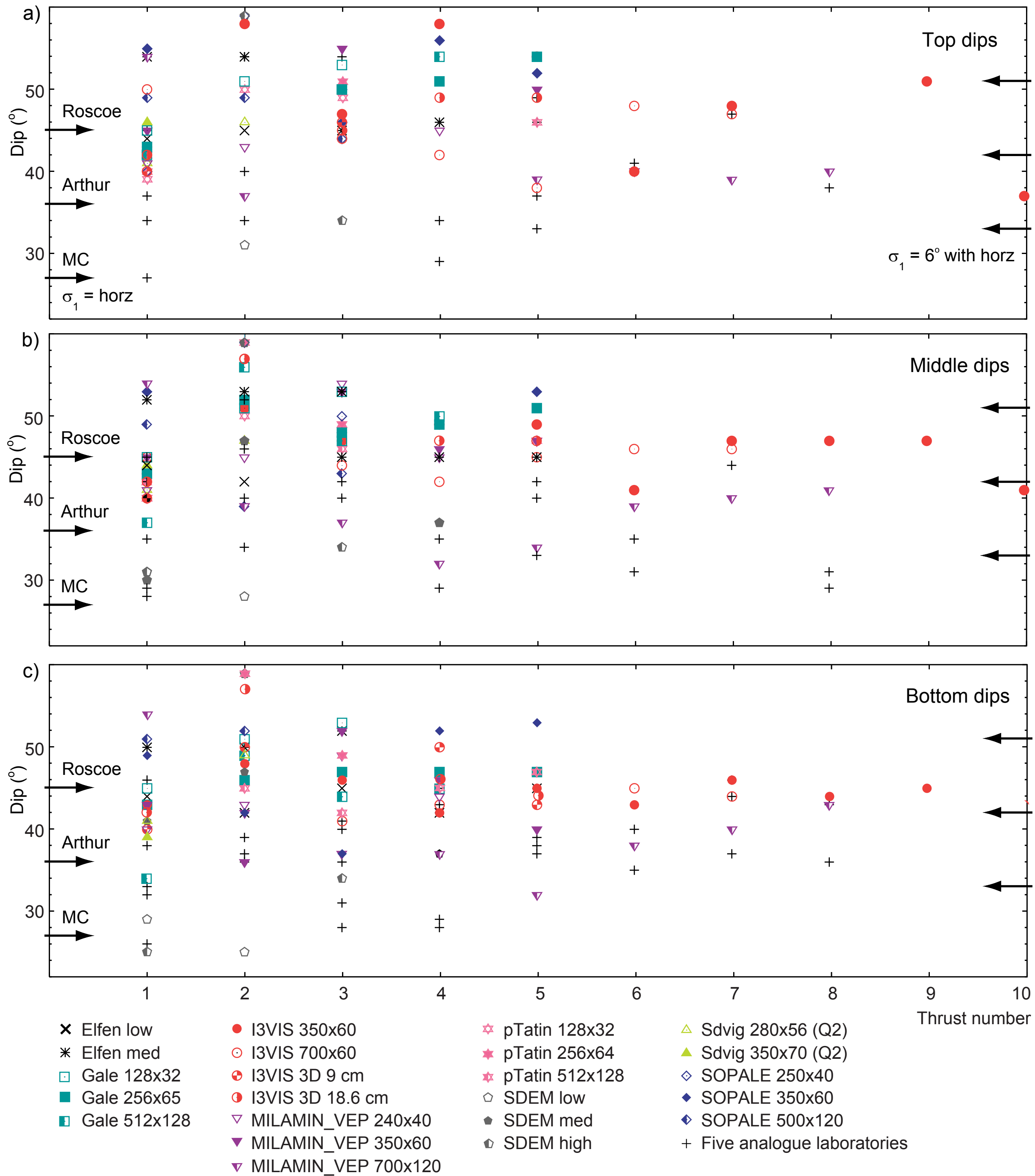

Fig. 15. Dip angles of backward shear zones for experiment 2. Dip angles were measured for each thrust when the thrust just formed and accumulated enough offset to be visible on finite strain plots and as a small surface topography (Fig. 3d). Theoretical shear zone dip angles with σ_1 for Roscoe, Arthur, and Mohr–Coulomb (MC) (Eqs. (8)–(10)) are indicated with arrows. Initially, σ_1 is horizontal, resulting in the theoretical dip angles indicated at the left side of the graphs. For a critical tapered wedge with our material properties, σ_1 makes an angle of 6° degrees with the horizontal. The theoretical dip angles for this situation are indicated at the right side of the graphs. For each experiment up to 3 different resolutions are shown. The analogue results are from Schreurs et al. (2016). a) Top dip angles, b) Middle dip angles, and c) Bottom dip angles.

numerical dip angles become steeper than Mohr–Coulomb upwards. As numerical shear band dip angles are sensitive to resolution, one speculation could be that the numerical models would need to increase their resolution in order to reach Mohr–Coulomb dip angles also towards the surface of the model (top dips). However, our models show no trend towards lower dip angles for higher resolution. In addition, bottom dips are Mohr–Coulomb, while middle and top dips are not. It is important to keep in mind that all shear band dip angles between Roscoe and Mohr–Coulomb are admissible (Vermeer, 1990). The dip angles of analogue backward thrusts are highly variable, making a comparison not very meaningful.

5.5. Experiment 2: discussion

5.5.1. Numerical sensitivity analyses

Despite the strictly described setup, the numerical models show variability in style of thrust wedge formation (pop-ups versus

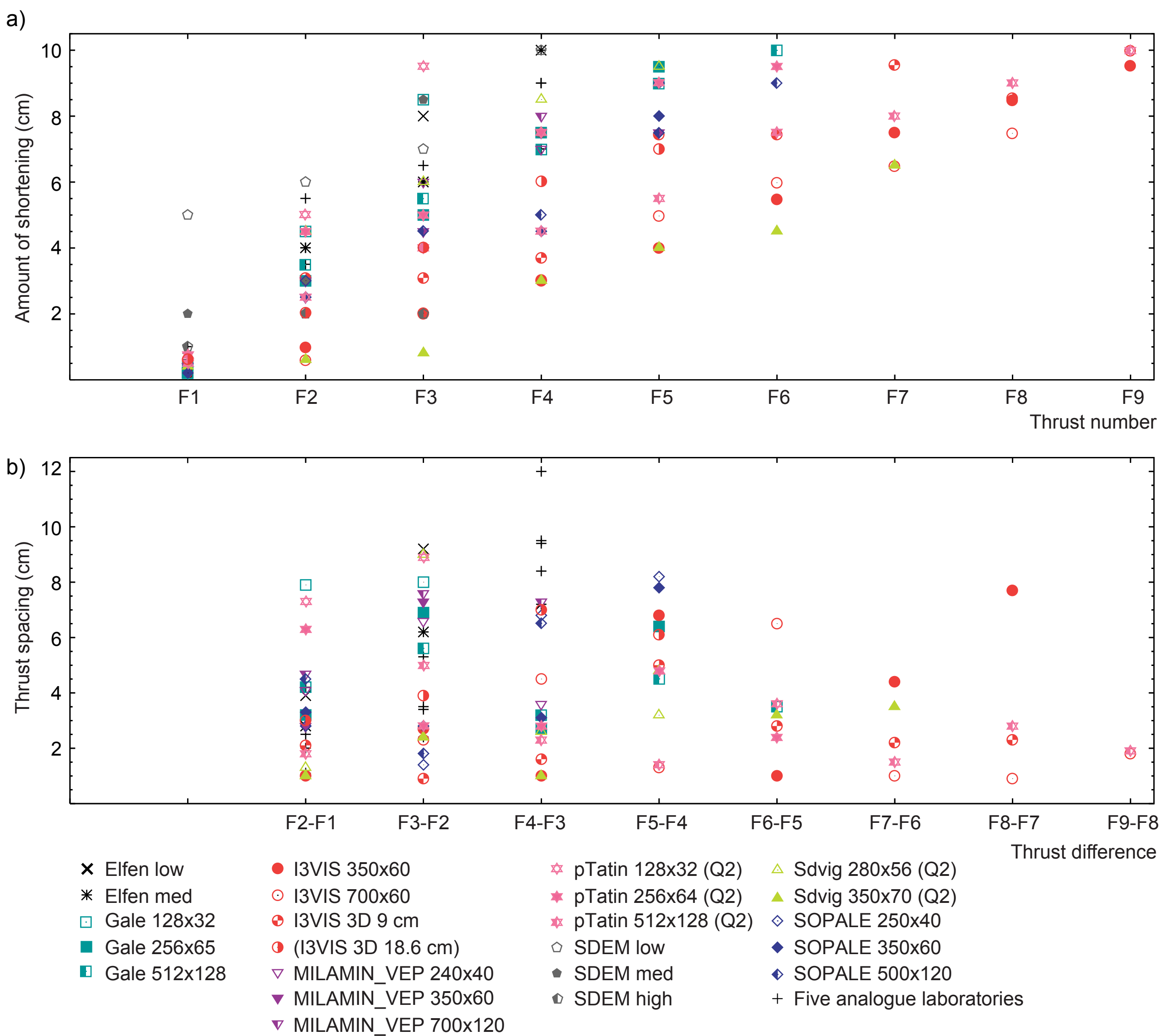

Fig. 16. a) Amount of shortening at which each forward thrust forms versus thrust number for experiment 2. As expected, more thrusts form with increasing shortening, but a large spread exists as to when thrusts form in the numerical and analogue models. b) Thrust spacing between forward thrusts, plotted as spacing from a newly formed thrust to the previous forward thrust (Fig. 3d). In both panels, up to 3 different resolutions are shown for each experiment. The analogue results are from Schreurs et al. (2016).

forward thrusting dominated), number of forward and backward thrusts, thrust dip angle, and thrust spacing. Experiment 2 was run at 2 to 3 different resolutions by each of the participating 8 codes. For our continuum models, no strong indications exist for an increase in number of shear zones with increased mesh resolution, or a corresponding decrease in thrust spacing. The similarity of individual model results with changes in resolution (Fig. 9) furthermore indicates that resolution is not a decisive factor causing inter-model differences. We further tested the effects of element type (Q1P0 versus Q2P1), time step, the frictional boundary condition, and grid remeshing (Appendix B).

An intriguing observation is that the two finite element models that employ higher-order (Q2P1) elements, pTatin and Sdvig, tend to deform by folding rather than by shear zone formation (Fig. 8). A test with MILAMIN_VEP shows, however, that the order of the element is not the cause of this difference in deformation style (Fig. B.31). pTatin and Sdvig also used larger time steps than the prescribed 3.6 s (Table 3). Even though brittle behaviour is time independent, the time step used in forward modelling can impact localisation behaviour because it affects particle advection and error propagation. Tests with SOPALE show that the location of shear zones change with changes in time step, but that the time step is not causing the difference in localisation behaviour (Fig. B.32). Further tests with pTatin point to the role of grid remeshing in shear zone localisation (Fig. B.33). pTatin remeshes its grid every time step, without interpolating the velocities onto the new mesh. This causes a slight shift of the shear bands in the particle reference frame. This in turn could cause strain-softening to act diffusely, leading to folds rather than localised shear zones. Changing the remeshing strategy is shown to largely improve the situation (Fig. B.33b,c).

The models in experiment 2 also differed in the implementation of boundary friction. A test with pTatin shows that the choice of boundary friction algorithm can cause substantial changes in wedge propagation even within one code (Fig. B.33a,b). In the next section we show that it is likely the difference in the effective basal friction that is the cause of much of the inter-model variability for experiment 2, for both analogue and numerical models.

5.5.2. Effect of basal friction

Part of the variability among the models in experiment 2 is

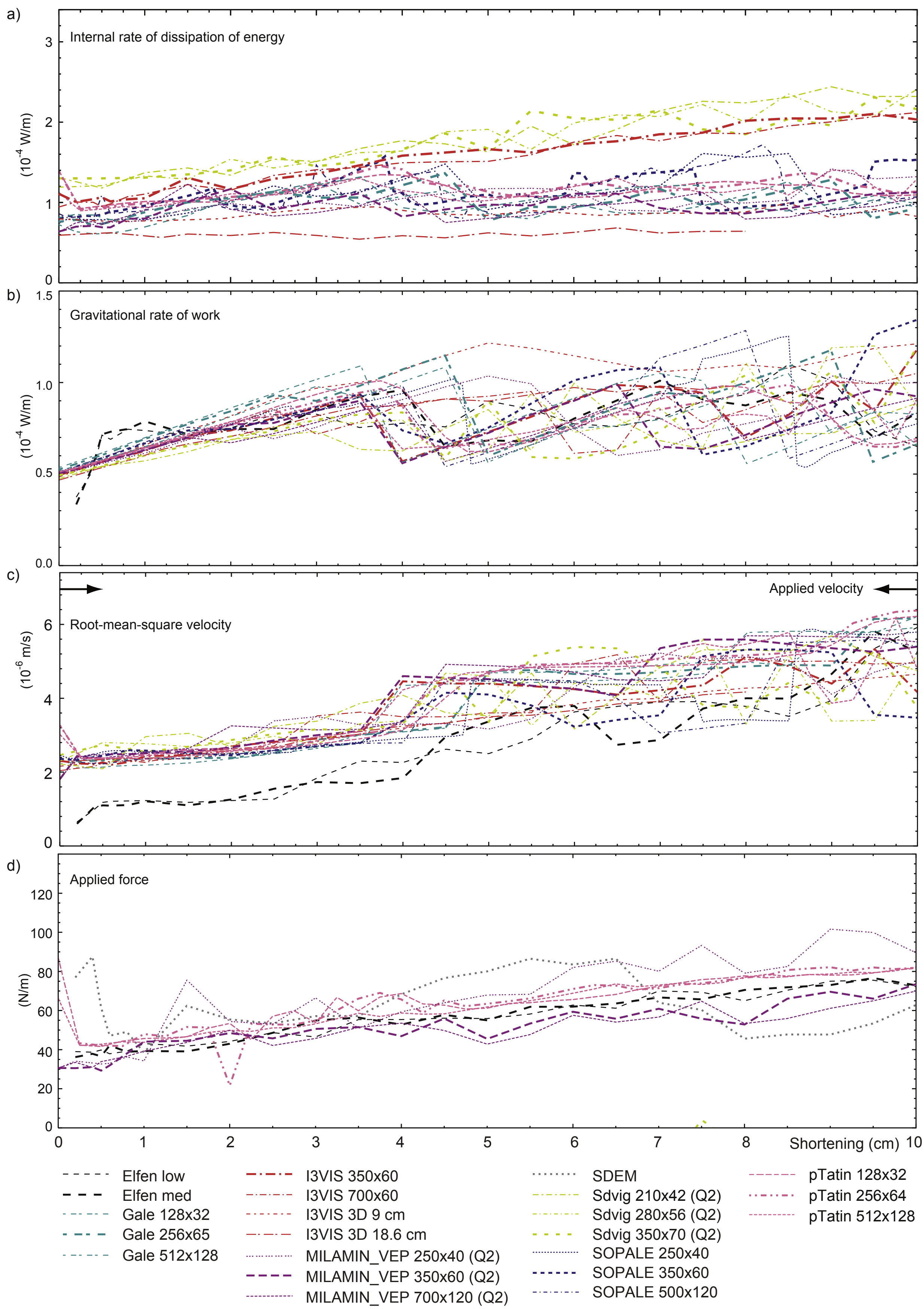

Fig. 17. a) Internal rate of dissipation of energy, b) gravitational rate of work, c) root-mean-square velocity, and d) applied force versus shortening for experiment 2. In all panels, up to 3 different resolutions are shown for each experiment.

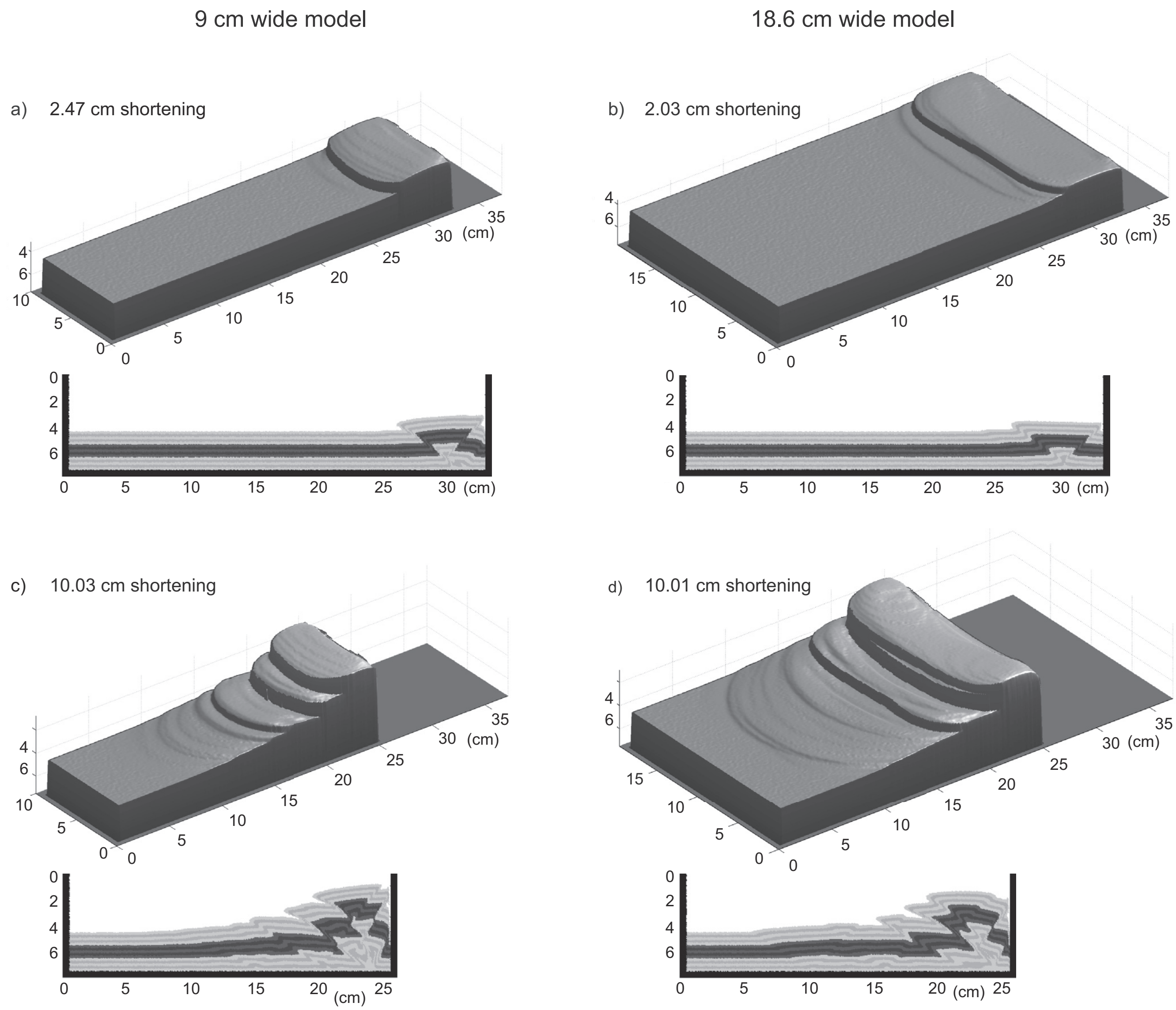

Fig. 18. 3-D models of experiment 2 computed with I3VIS, showing surface view and a cross-section through the centre of the model domain at a) 2.5 cm shortening for a model width of 9 cm, b) 2 cm shortening for a model width of 18.6 cm c) 10 cm shortening for a model width of 9 cm, and d) 10 cm shortening for a model width of 18.6 cm.

related to the difference in style of thrust wedge formation: some models deform in a style dominated by pop-up structures formed by a forward and backward thrust (e.g., Elfen and GALE), whereas others are dominated by forward thrusts (e.g., MILAMIN_VEP and SOPALE) (Fig. 8). The same two deformation styles are observed in the analogue models of experiment 2 (Schreurs et al., 2016). We speculate here that this variability may be related to differences in the effective boundary friction. The numerical models employ different algorithms to apply the frictional condition that simulates sand–foil interaction at the model boundaries (Section 3.6) and these may result in differences in the effective basal friction. Analogue models may differ in their effective boundary friction depending on how the model was built. Boundary friction measurements for quartz sand on foil for the analogue materials vary with up to 6° for the angle of boundary friction and an order of magnitude for basal cohesion (Table 1). Fig. 20 shows three results of experiment 2 computed with SOPALE which only differ in the basal friction magnitude. The results illustrate that a lower basal friction results in further outward propagating of the wedge in a style which is dominated by both forward and backward thrusts (pop-ups). A higher basal friction leads to a shorter wedge which is dominated by forward thrusts (Davis and Engelder, 1985; Huiqi et al., 1992). Though this is not a strict proof, it is a support for our proposal that the numerical and analogue models of experiment 2 did not all have the same effective basal strength and that this influenced their style of wedge formation.

6. Experiment 3

6.1. Experiment 3: model setup

The third experiment examines thrust evolution in a brittle material for a setup in which the initial deformation occurs away from the mobile wall (Figs. 2a and 3c). The model is again built of three horizontal layers of quartz-corundum-quartz sand which are shortened by a mobile wall which moves into the model domain with 2.5 cm h^{-1}. A stiff basal sheet is attached to the mobile wall and moves with it forming a velocity discontinuity at 12 cm from the mobile wall. The sheet is 1 mm thick in the analogue experiments, but not included explicitly in the model domain of the

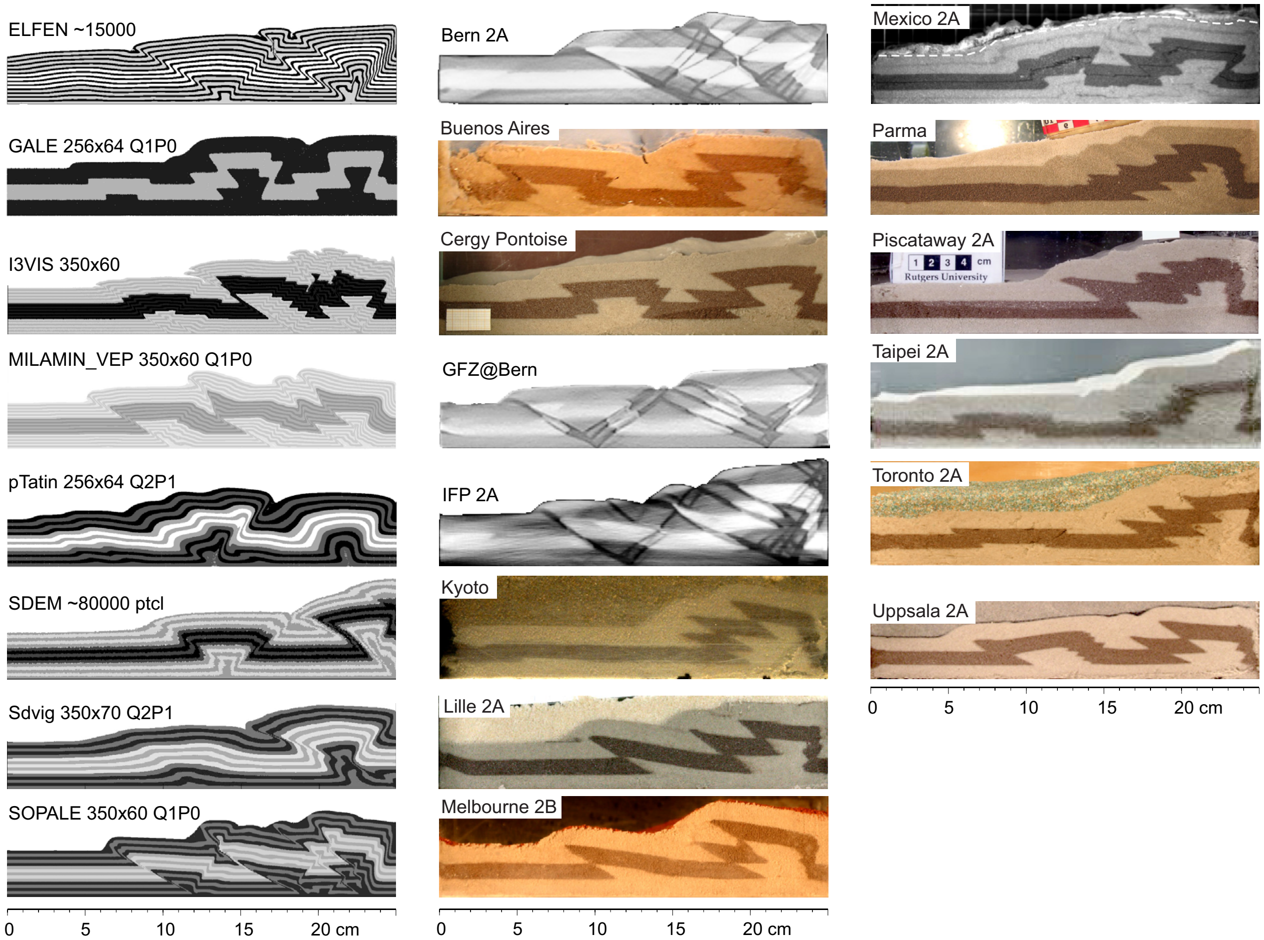

Fig. 19. Comparison of numerical and analogue results of experiment 2 at 10 cm shortening. Numerical results in left column, analogue results in middle and right columns. The analogue sections are at 50% model width, except Lille which is at 50% − 2 cm, and are courtesy of Schreurs et al. (2016).

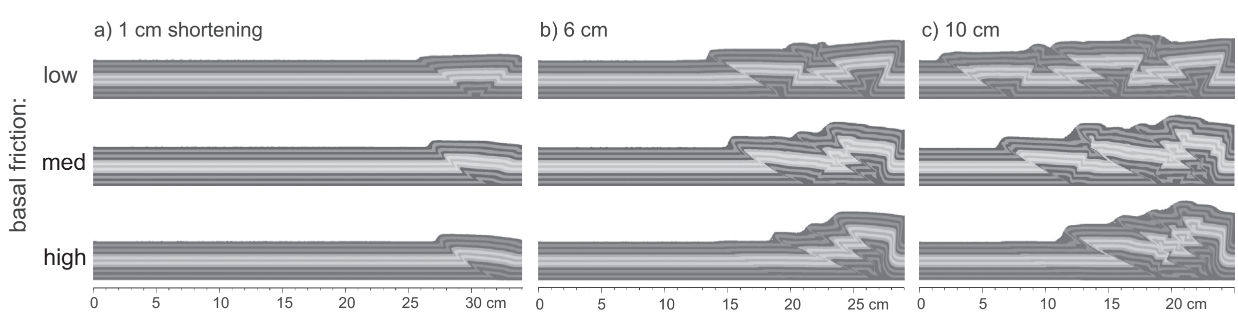

Fig. 20. The style of deformation of experiment 2 depends on the effective basal friction. For a low basal friction, deformation moves further outward (at equal amount of shortening) and occurs in a more symmetric style in comparison with higher basal friction experiments. Top: low basal friction ϕ_b 11° softening to 9°, middle: medium basal friction ϕ_b 16° softening to 14° (default), bottom: high basal friction ϕ_b 21° softening to 19°. Models run with SOPALE with a resolution of 350 × 60 elements in the sand domain.

Table 4
Numerical parameters for experiment 3.

Code	Method	Elements	Tracers	Basal bc	Air	Elasticity[a]	Diffs wrt description
Elfen	FEM	14,700–15,300	–	friction	no	E = 5e6 Pa	$\phi_b^p = \phi_b^s = 15°$
GALE[b]	ALE	256 × 64 Q1P0	491,520	layer	no		left side fixed, variable Δt
I3VIS[c]	FDM	350 × 60	1400 × 240	layer	yes		variable Δt
MILAMIN_VEP[b]	FEM	350 × 60 Q1P0	6946 × 302	layer	no		
pTatin	FEM	256 × 64 Q2P1	262,144	friction	no		Δ t = 36s, $\phi_b^p = \phi_b^s = 15°$
Sdvig	FEM	350 × 70 Q2P1	94,500	layer	yes		Δ t = 14.4 s
SOPALE[b]	ALE	350 × 60 Q1P0	1049 × 171	layer	no		

[a] The models have no elasticity, unless a value for Young's Modulus E is given.
[b] GALE, MILAMIN_VEP and SOPALE smooth the velocity discontinuity at the tip of the sheet over 2 elements.
[c] I3VIS includes the mobile basal sheet (with a thickness of 0.5 mm) explicitly in the model domain.

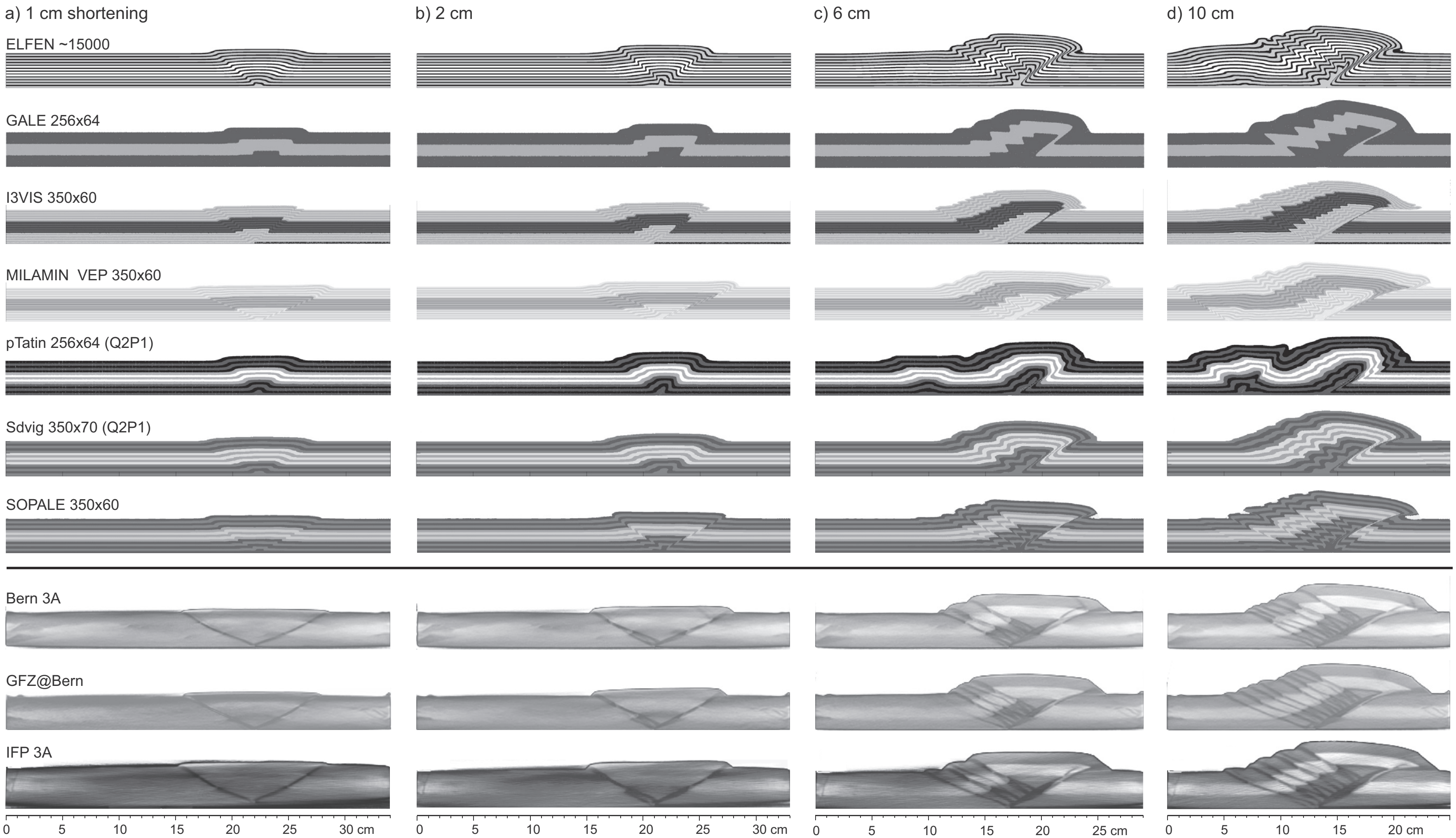

Fig. 21. Material fields of experiment 3 after 1, 2, 6 and 10 cm of shortening for 7 numerical models. Resolution in number of elements or particles is shown with the model names. Shortening is initially accommodated by the formation of a pop-up structure centred on the tip of the basal sheet. With increasing shortening, forward thrusts initiate at the tip of the basal sheet and are then progressively translated upward along the backward thrust. Results of the analogue laboratories of the University of Bern and IFP (as imaged in an X-ray computer tomographer) from Schreurs et al. (2016) shown below.

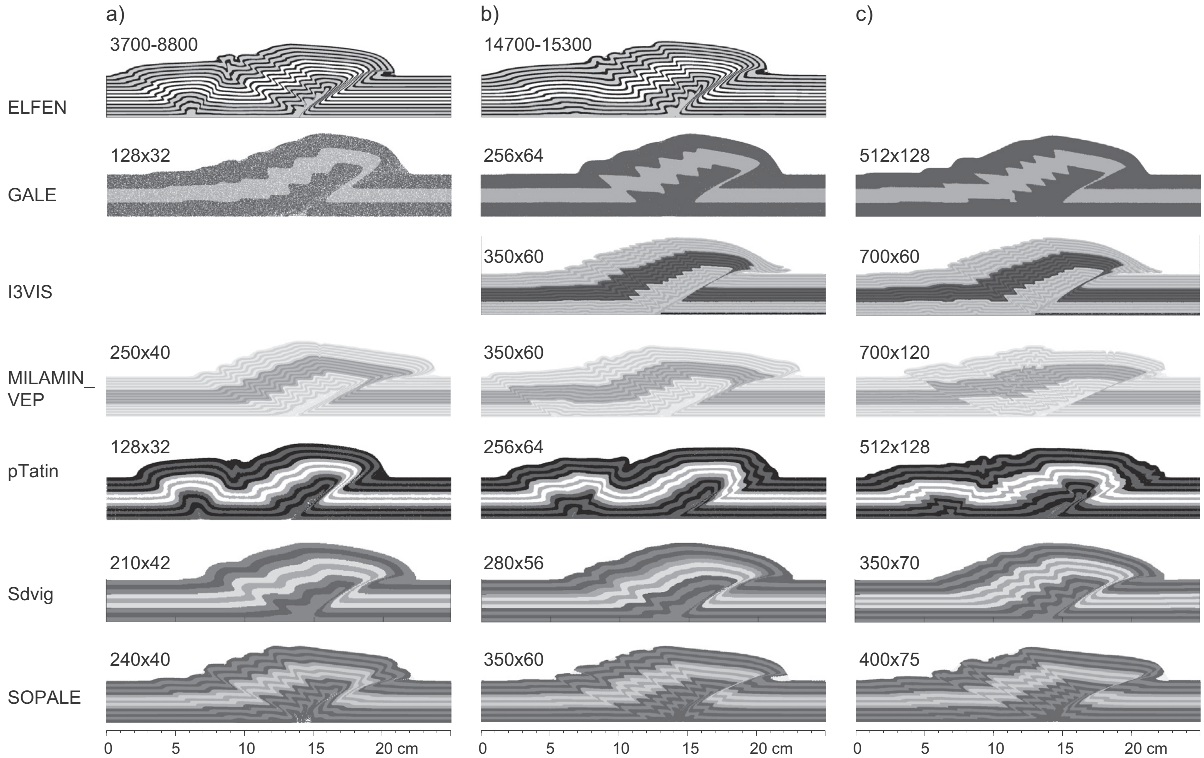

Fig. 22. Material fields at 10 cm shortening for experiment 3 at different resolutions.

numerical experiments. For continuum models, the tip of the sheet forms a sharp velocity discontinuity which poses a numerical challenge as the jump in velocity needs to be accommodated over one element or between two nodes. GALE, MILAMIN_VEP and SOPALE taper the velocity jump over 2 elements, whereas Elfen, I3VIS, Sdvig and pTatin have a strict velocity discontinuity. These different implementations did not lead to clear differences in model results. The initial surface slope is 0° and basal slope remains at 0° throughout the experiment. This setup is not expected to build a wedge at critical taper above the base.

Experiment 3 was run by 7 codes at 2 to 3 different resolutions each (Table 4). All codes employed the boundary friction for quartz sand only and ignored the effect on boundary friction of the alternation of quartz-corundum-quartz sand at the front- and backwalls.

6.2. Experiment 3: results

During the first few centimeters of shortening, all models form a pop-up centred above the velocity discontinuity (Fig. 21). The right branch of this pop-up becomes a dominant backward thrust. As the velocity discontinuity (the tip of the sheet) moves to the left, new forward thrusts form that are progressively transported upwards along this backward thrust. Some models form an additional backward thrust parallel to the main backward thrust at later shortening stages (pTatin, SOPALE). As the velocity discontinuity is such a strong deformation localiser, most thrusts form at this location. However, in some models deformation steps out and a new pop-up is formed in front of the thrust stack (Elfen, MILAMIN_VEP, pTatin). We speculate that in these cases, the boundary friction algorithm and/or the implementation of the velocity discontinuity may have smoothened the impact of the velocity discontinuity, allowing deformation to step out.

As for experiment 2, changes in resolution lead to variations in the number of shear zones and in shear zone width, but the individual styles of models do not change (Fig. 22). The strain and especially strain-rate fields highlight many incipient shear zones that do not all accumulate enough offset to become visible in the material field (Fig. 23a,b and Fig. 24). Gale and I3VIS show a tendency for outward stepping of deformation, which in contrast to Elfen, MILAMIN_VEP and pTatin does not lead to finite deformation in front of the thrust stack. SOPALE has incipient shear zones both in the frontal and back domains. The pressure field in the models is mainly lithostatic, with lower pressure values in (incipient) shear zones (Fig. 23c,d). Pressure is highest under the stacked thrusts, reflecting overburden loading.

Experiment 3 simulates an unstable wedge, but we do not have an analytical prediction for its critical taper value. This is because it is unclear whether a critical taper would build over the base of the model or over the strain-softened main backward thrust. The numerical surface slope values have a larger spread than in experiment 2 (Figs. 25 and 26). After 10 cm of shortening, the surface slopes lie between 10° − 20° (Fig. 26, Table A.11).

Forward thrusts are slightly listric, with bottom dip angles about the Mohr–Coulomb value, or lower, and top dip angles around the Arthur value (Fig. 27a–c, Table A.12). The lower and middle thrust dip angles tend to lie below theoretical predicted values. This may reflect that σ_1 is not parallel to the base of the model domain for this setup. The number of backward thrusts is low in this experimental setup, but the backward thrusts have again a large range in dip values (Fig. 27d–f, Table A.12).

As may be expected, more forward thrusts form with increasing amounts of shortening, but the rate of thrust formation differs between models (between ca. 0.6–1.1 thrusts/cm shortening) (Fig. 28). I3VIS models have the largest number of thrusts, pTatin and Elfen the lowest (Table A.13).

The values for internal rate of dissipation of energy, gravitational rate of work and root-mean-square velocity show fair

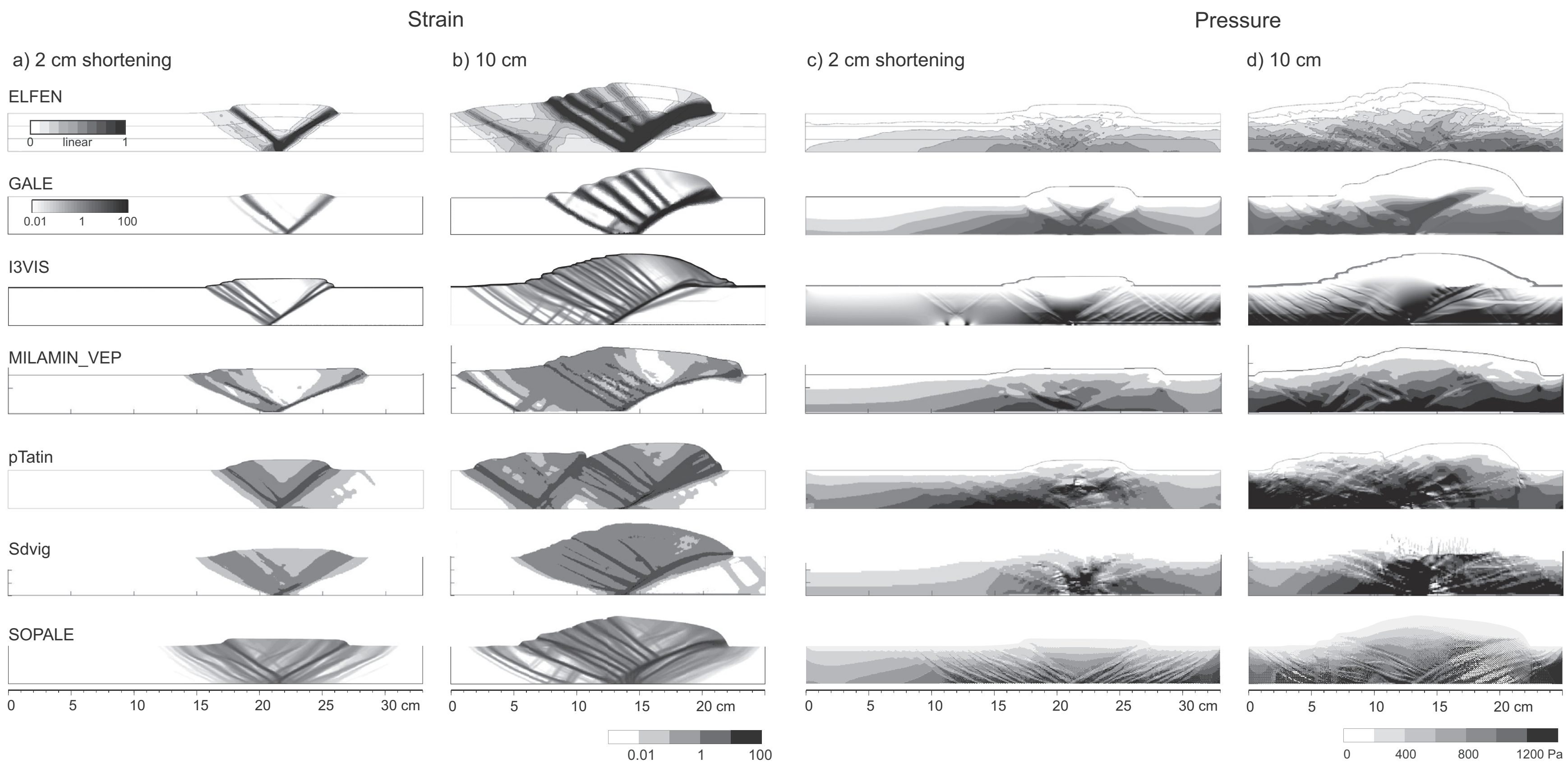

Fig. 23. Finite strain fields (measured as second invariant of the strain tensor) and dynamic pressure (mean stress) fields of experiment 3 after 2 and 10 cm of shortening. The models are shown at the same resolution as in Fig. 21.

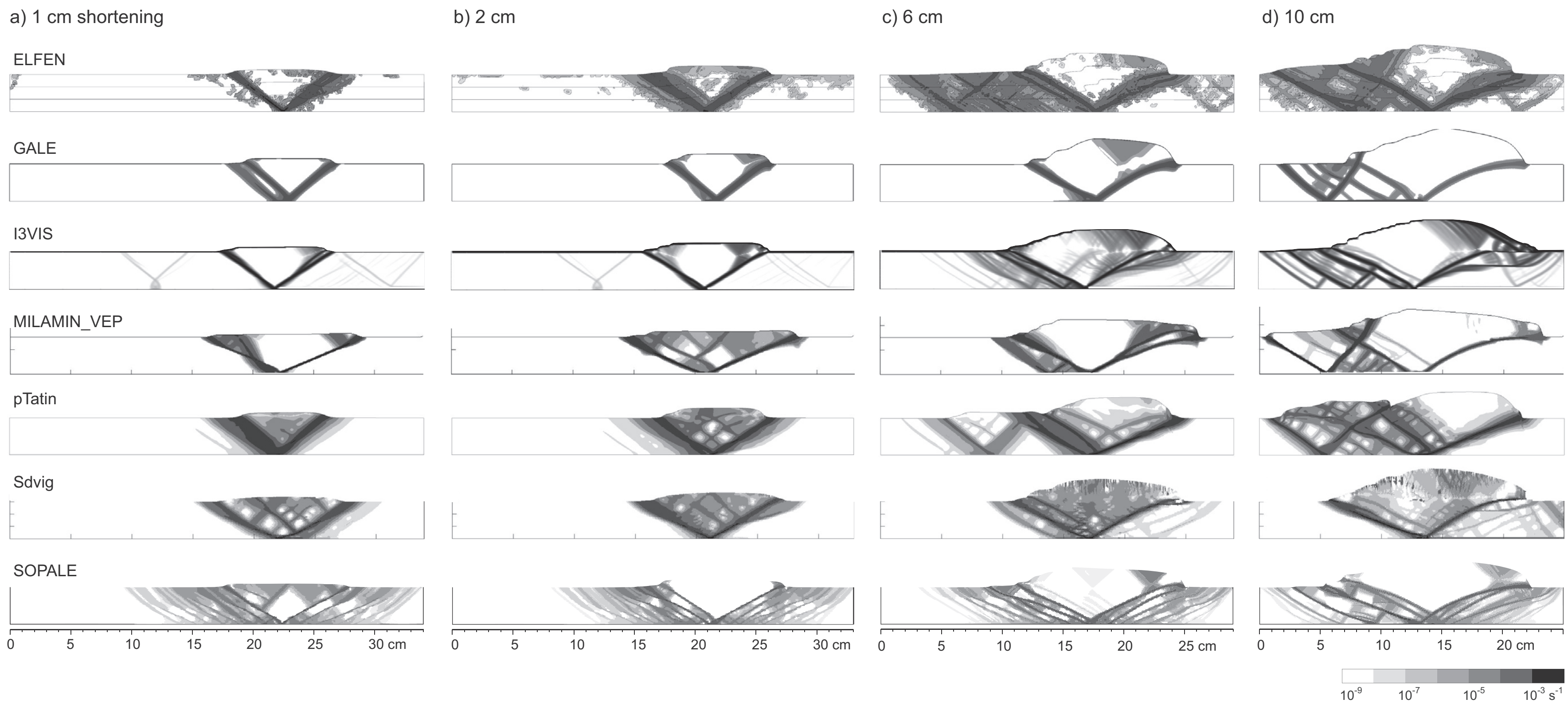

Fig. 24. Strain-rate fields of experiment 3 after 1, 2, 6 and 10 cm of shortening. The models are shown at the same resolution as in Fig. 21.

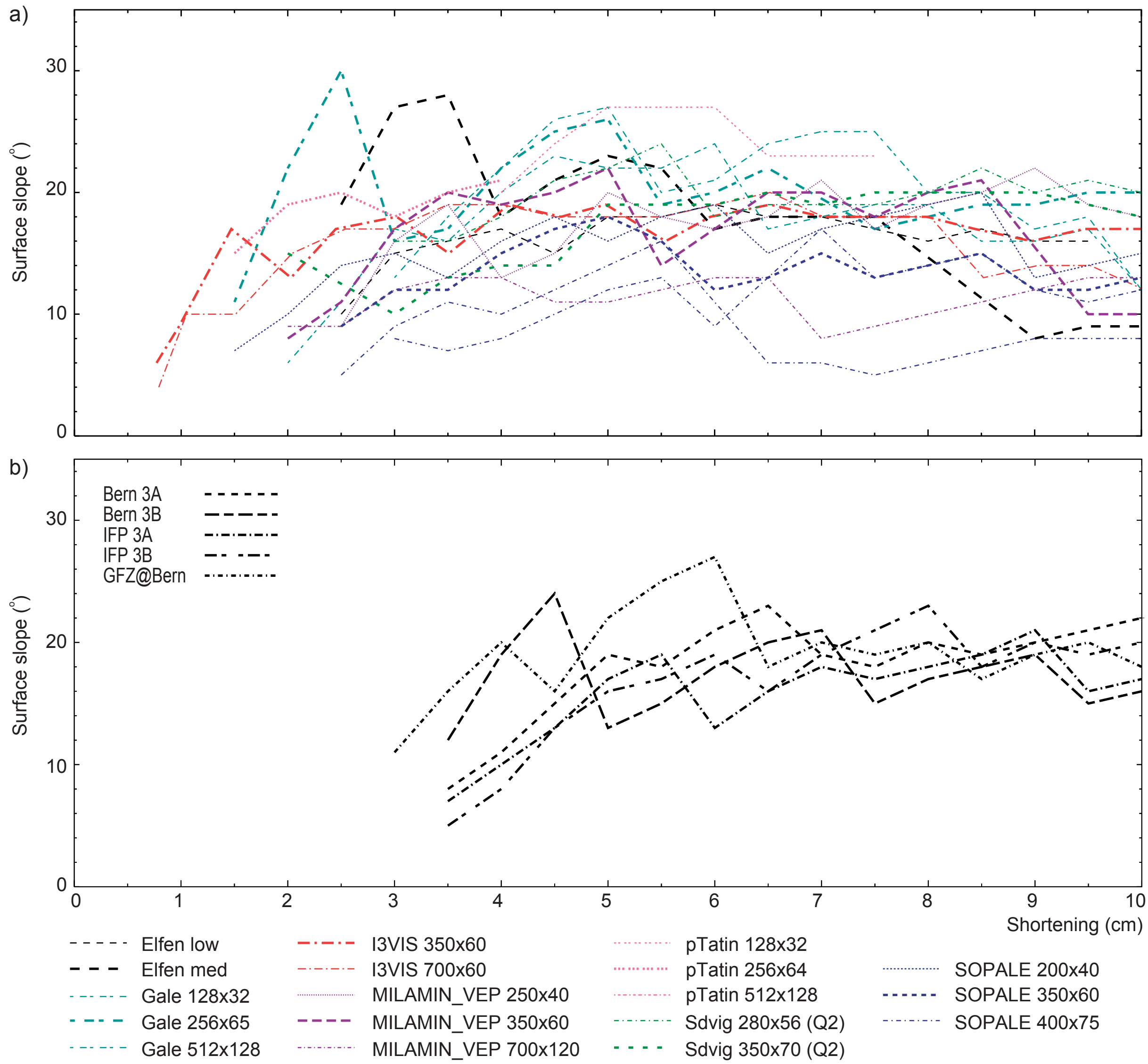

Fig. 25. Surface slope against shortening for experiment 3. Surface slope is measured as the best visual fit line through the valleys of the thrusts (Fig. 3d). All values at 0.5 cm of shortening can be found in Table A.11. a) 2-D numerical surface slope values for up to three different resolutions. b) Surface slope values for sections through the middle of the model domain of 5 analogue models that analysed results in an X-ray tomographer (Schreurs et al., 2016). Up to two experiments per analogue laboratory are shown.

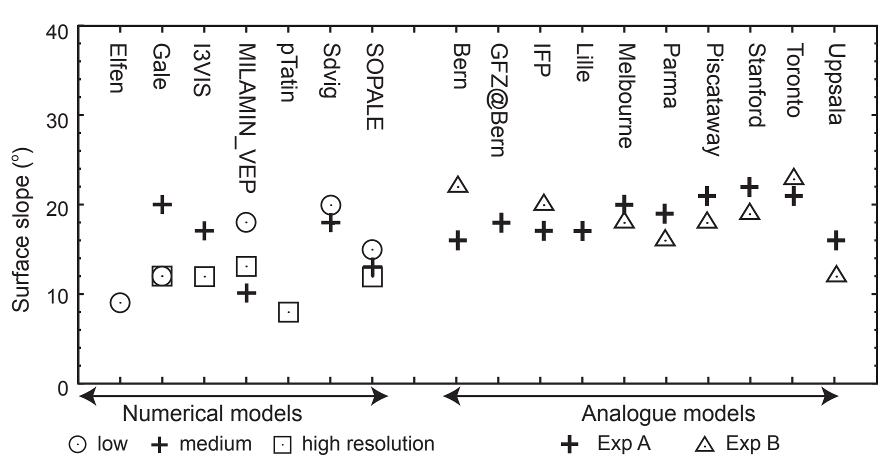

Fig. 26. Surface slope at 10 cm shortening for numerical and analogue models for experiment 3. The results of the numerical experiments are shown for up to three different resolutions (Table A.11). The analogue results (Schreurs et al., 2016) are for sections through the middle of the experiment and show up to two experiments per laboratory.

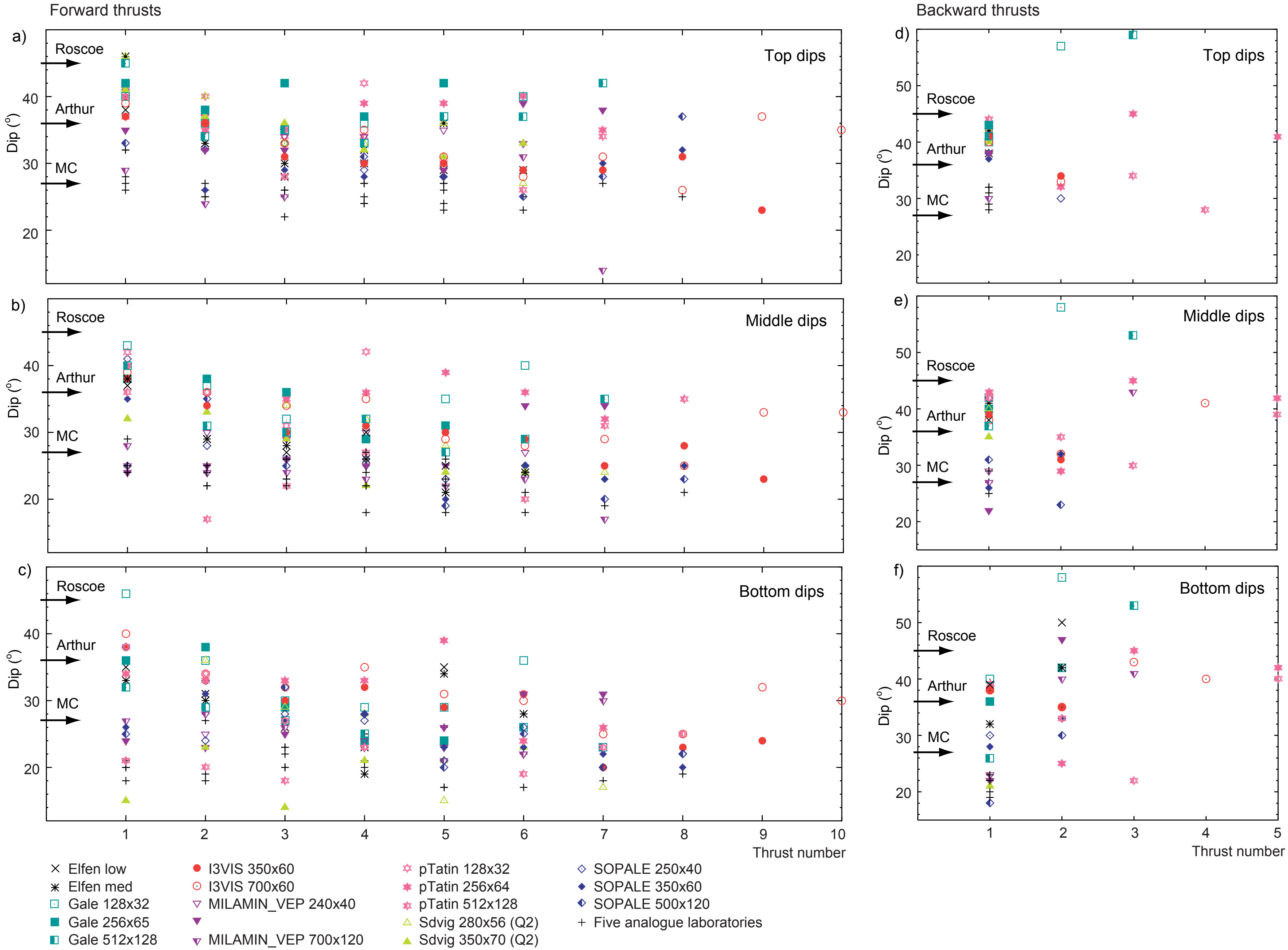

Fig. 27. Dip angles of forward and backward shear zones for experiment 3. Dip angles were measured for each thrust when the thrust just formed and accumulated enough offset to be visible on finite strain plots and as a small surface topography (Fig. 3d) Theoretical shear zone dip angles with σ_1 for Roscoe, Arthur, and Mohr–Coulomb (MC) (Eqs. (8)–(10)) are indicated with arrows for the initial stage where σ_1 is horizontal. For each experiment up to 3 different resolutions are shown. The analogue results are from Schreurs et al. (2016). Forward shear zones: a) Top dip angles, b) Middle dip angles, and c) Bottom dip angles. Backward shear zones: d) Top dip angles, e) Middle dip angles, and f) Bottom dip angles.

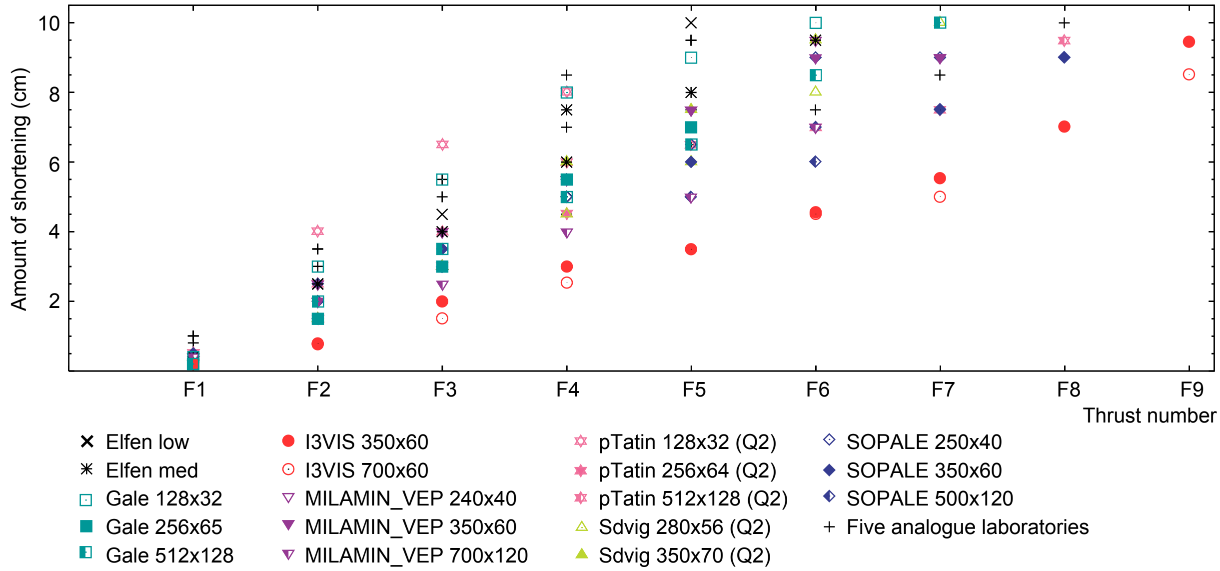

Fig. 28. Amount of shortening at which each forward thrust forms versus thrust number for experiment 3. For each experiment, results at 2–3 different numerical resolutions are shown. More thrusts form with increasing shortening, but with a large spread in number of shear zones at a specific amount of shortening for the numerical and analogue models.

agreement among the models (Fig. 29, Table A.10). The variation between models in the internal rate of dissipation of energy lies within a factor 2 (Fig. 29a). The gravitational rate of work increases with the amount of shortening, reflecting the growth of the wedge (Fig. 29b). The root-mean-square velocity is fairly constant for most models, which likely reflects that the deformation style is set early in the experiment and forward thrusts are no longer active once they are translated upward in the thrust stack (Fig. 29c). The applied force for the models that provided this value increases with amount of shortening, reflecting the building of the thrust stack (Fig. 29d).

6.3. Experiment 3: numerical-analogue comparisons

The numerical and analogue models build a stack of forward thrusts over a dominant backward thrust (Fig. 30). In all analogue experiments, deformation is concentrated in this thrust stack, whereas some of the numerical models show deformation propagating to the foreland. We speculate again that this variability in deformation style may be related to the numerical implementation of the basal boundary friction and the velocity discontinuity.

The similarity in wedge shapes for the analogue models is reflected in similar surface slopes (Figs. 25 and 26). The analogue surface slopes converge to similar values whereas the numerical surface slopes show larger variations. This is the opposite situation of experiment 2, where the numerical models converged towards the critical taper value. The variations in the numerical surface slopes are likely due to the variation in deformation style in this experiment. In some models deformation steps forward in a frontal pop-up, whereas thrusting remains localised in the thrust stack in others. Wedges are built with a similar number of forward thrusts in the numerical and analogue models (Fig. 28, Table A.13). As in experiment 2, the dip angles of forward and backward thrusts of the analogue models are consistently lower than for the numerical models. Shear bands in the analogue models are likely to initially form at Mohr–Coulomb angles, because of low confining pressure and a non-zero initial dilation angle (Section 3.3), whereas shear zone dip angles in numerical continuum models with zero dilation will range between the Mohr–Coulomb and Roscoe values. The numerical shear zone dip angles may therefore be higher.

6.4. Experiment 3: discussion

Despite the strictly prescribed setup and similar numerical resolutions, the numerical models show variability in style of deformation, number of forward and backward thrusts, thrust dip angles, and surface slope. This experiment illustrates the intrinsic difficulty that numerical models face when reproducing analogue setups. The boundary conditions in the analogue experiments are not commonly used in numerical experiments and therefore not fully tested. The different numerical implementations of boundary friction in the participating codes likely has an impact on the numerical results, but we could not evaluate the effects in a quantitative manner from our study. However, we speculate that the different implementations led to differences in the effective basal friction, thus causing differences in deformation style in experiments 2 and 3. We note that the analogue results for experiment 2 show similar differences in deformation style as the numerical models, pointing to likely variations in effective basal friction also for analogue models. A sharp velocity discontinuity as in experiment 3 is challenging as the velocity jump needs to be accommodated over one element or between two nodes, causing potential dynamic pressure differences. Also this may give rise to differences in model results. For future numerical-analogue comparison experiments, we recommend avoiding frictional boundary conditions and sharp velocity discontinuities.

7. Conclusions

We present a comparison of results of seven to eleven numerical codes for three brittle thrust wedge experiments that are inspired by analogue setups. The companion paper by Schreurs et al. (2016) presents results of fifteen analogue laboratories for the same three setups. To allow future comparisons to our results, we provide detailed descriptions of the experimental setups and quantifications of bottom, middle and top shear zone dip angles, number of shear zones, surface slope, rate of dissipation of internal energy, gravitational rate of work, root-mean-square velocity, and applied force as well as visualisations of the material, strain, strain-rate and pressure fields. All eleven participating codes pass the first stable wedge test by showing negligible internal deformation of a wedge that is translated horizontally over a frictional boundary. Eight

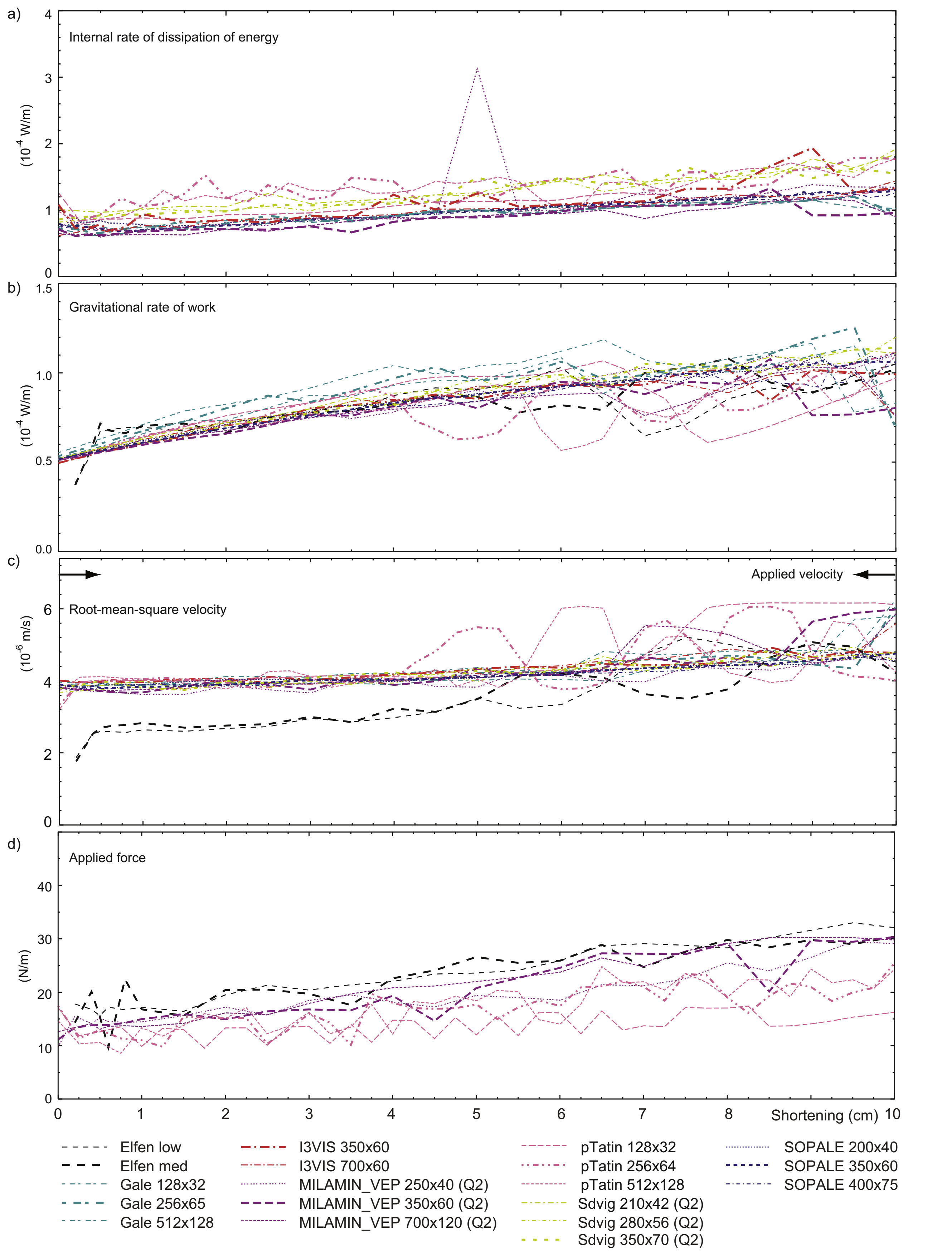

Fig. 29. a) Internal rate of dissipation of energy, b) gravitational rate of work, c) root-mean-square velocity, and d) applied force versus shortening for experiment 3. In all panels, up to 3 different resolutions are shown for each experiment.

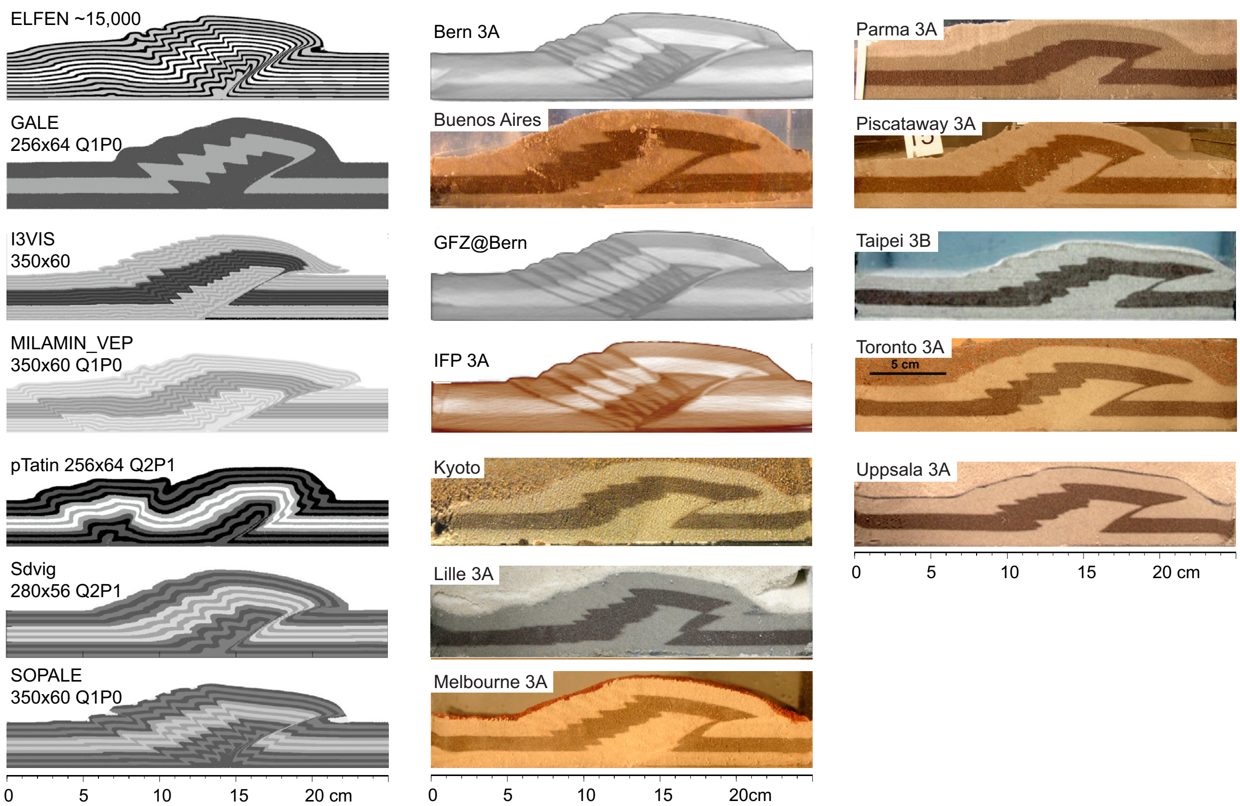

Fig. 30. Comparison of numerical and analogue results of experiment 3 at 10 cm shortening. Numerical results in left column, analogue results in middle and right columns. The analogue sections are at 50% model width, except Lille which is at 50% − 2 cm, and are courtesy of Schreurs et al. (2016).

codes run the second experiment that builds a critical taper from a subcritical initial state by translating a vertical (backstop) wall into a horizontally layered sandpack. All codes recover the critical taper angle, but we obtain two deformation styles characterised by either mainly forward dipping thrusts or a series of thrust pop-ups. The same two deformation styles are obtained in the corresponding analogue models of Schreurs et al. (2016). We speculate that these styles are caused by differences in effective basal friction. In the third experiment, which was run by seven codes, shortening is transferred to the centre of the model domain by a rigid sheet attached to the mobile backwall. The tip of the sheet represents a velocity discontinuity for the numerical models. The experiments build a stack of forward thrusts that are translated upward along a main backward thrust above the velocity discontinuity. The variability among the numerical results is less than the variations in analogue results in experiment 2, but this is reversed in experiment 3 where the numerical results show higher variability.

Despite strictly prescribed numerical setups and a similar range of numerical resolutions tested, we find variations in surface slope, the number of shear zones, the degree of localisation of shear zones, shear zone dip angle, internal rate of dissipation of energy and applied force. We suggest that a large part of the numerical variability may be caused by the difficulty of representing frictional boundary conditions and sharp velocity discontinuities with continuum numerical methods. We recommend future experiments, that aim at direct comparisons of numerical and analogue results, to avoid frictional boundary conditions and sharp velocity discontinuities. Numerical benchmarks are best based on analytical solutions or setups that have boundary conditions which are straightforward to implement by all participating codes. The variability in the modelled shear zones in our experiments also points to a need for the numerical Earth Sciences community to define a test for brittle material behaviour.

Because brittle material behaviour remains a numerical challenge, we recommend that future studies report all details of their numerical plasticity approach. This ideally should include all applicable descriptions and values of:

1 The pre-yield behaviour (elastic, viscoelastic, rigid),
2 The computation of the initial plastic step,
3 The computation of plastic yield (at integration points, particles, element),
4 Interpolation and/or averaging methods employed for viscosity,
5 Whether viscous and brittle behaviour are implemented in parallel or serial,
6 Adjustments for near-surface yield behaviour in regions where frictional strength is low,
7 The solution methods used to solve the non-linear problem and the linearized problem for velocity and pressure,
8 The discretisation technique and the order of employed shape functions,
9. The stopping criterion used to terminate the non-linear solver and the linear solver,
10 The convergence behaviour of the non-linear residual,
11 The number of non-linear solves which failed to converge and whether the time step was taken in the event of a non-converged non-linear solve,
12 The dilation angle,
13 Strain- or strain-rate dependent softening including its interval and rate,
14 Time step,
15 Background viscosity,
16 Bulk/shear modulus.

Overall, our experiments show that numerical models run with different numerical techniques can successfully reproduce laboratory brittle thrust wedge models at the cm-scale. We show how the formation of new shear zones and the localisation of deformation on these shear zones allow deformation to obtain the critical taper angle. The similarity in results between the analogue and numerical models encourages using both techniques for investigating the formation and evolution of accretionary prisms and fold-and-thrust belts. However, we emphasize that, where shear zones are concerned, trends, rather than absolute numbers, should be used in applications of model results to natural settings.

Acknowledgements

We would like to thank the following analogue modelling laboratories for providing images of their experiments: Bern, Buenos Aires, Cergy-Pontoise, GFZ, IFP Energies Nouvelles, Kyoto, Melbourne, Mexico, Parma, Piscataway, Tapei, Toronto, and Uppsala. More details of their results can be found in Schreurs et al. (2016). We thank Susan Ellis, Luke Hodkinson and Louis Moresi for many discussions on numerical – analogue comparisons and the numerical implementation of boundary friction. Two anonymous reviewers provided constructive and helpful feedback on the manuscript. SOPALE was developed by Philippe Fullsack and augmented by the Dalhousie Geodynamics Group. C.T. benefited of an ERC Advanced Investigator Grant awarded to T. Torsvik, University of Oslo, Norway. M.A. thanks ExxonMobil Upstream Research Co. for permission to publish his contributions to this study. S.B. is grateful to the Geological Survey of Norway for internal funding of this project.

Appendix A. Numerical values of the wedge experiments

The quantification of results for up to 3 different resolutions for each participating code is given by the following tables:

Table A.5
Quantification of experiment 1 at 4 cm shortening.

Code	Resolution in domain (elements)	Dissipation (W m^{-1})	Gravitational rate of work (W m^{-1})	V_{rms} ($\times$ 10^{-6} m s^{-1})	Applied force (N m^{-1})
EEM	2523	–	–	–	8.202
Elfen	2349	4.13×10^{-6}	-1.08×10^{-8}	6.94	7.40
ELEFANT	400 × 100	1.23×10^{-8}	1.27×10^{-9}	6.94412	–
Fric2D	181	5.10×10^{-10}	1.52×10^{-10}	6.94432	13.6853
GALE	128 × 32	6.63×10^{-10}	1.06×10^{-10}	6.9446	3.03538
GALE	256 × 64	5.16×10^{-10}	5.30×10^{-11}	6.94452	3.92594
GALE	512 × 128	3.11×10^{-10}	5.10×10^{-11}	6.94446	4.07502
I3VIS	265 × 60	2.15×10^{-10}	2.67×10^{-11}	6.9444	–
MILAMIN_VEP	240 × 60	–	5.38×10^{-8}	6.930	11.90
pTatin[a]	128 × 32	1.09×10^{-6}	1.60×10^{-8}	5.76559	5.3557
pTatin	256 × 64	1.12×10^{-6}	1.90×10^{-9}	6.01182	5.3556
pTatin[b]	512 × 128	2.44×10^{-6}	-9.72×10^{-9}	6.53312	5.1895
SDEM	ca. 2000 ptcl	2.76×10^{-5}	4.49×10^{-9}	6.9468	4.1298
Sdvig	212 × 64	2.26×10^{-5}	-7.22×10^{-8}	6.93	1.62
SOPALE	331 × 75	2.76×10^{-10}	7.97×10^{-11}	6.94442	–
Average		–	–	6.76 ± 0.37	6.0 ± 3.5
Analytical		0	0	6.94444	7.9

[a] 3.75 cm of shortening.
[b] 3.26 cm of shortening.

Table A.6
Quantification of experiment 2 at 10 cm shortening.

Code	Resolution in sand (elements)	Dissipation ($\times$ 10^{-4} W m^{-1})	Gravitational rate of work ($\times$ 10^{-4} W m^{-1})	V_{rms} ($\times$ 10^{-6} m s^{-1})	Applied force (N m^{-1})
Elfen	3700–9000	–	0.650	5.92	72.9
Elfen	14700–15100	–	0.835	5.24	72.2
GALE	128 × 32	0.981336	0.825677	5.91568	–
GALE	256 × 64	0.925466	0.662107	6.16699	–
GALE	512 × 128	0.943758	0.660044	6.21015	–
I3VIS	350 × 60	2.03239	1.182606	4.1603	–
I3VIS	700 × 60	2.11934	1.050599	4.9557	–
MILAMIN_VEP	250 × 40	1.321075	0.998343	5.071892	89.566215
MILAMIN_VEP	350 × 60	1.123954	0.923470	5.432228	73.521024
MILAMIN_VEP	700 × 120	1.061362	0.914261	5.540580	69.993023
pTatin	128 × 32	1.094582	0.605170	6.218284	81.560014
pTatin	256 × 44	1.134233	0.682187	6.374850	81.877248
pTatin	512 × 128	1.292539	0.912553	4.775449	82.249730
SDEM	87936 ptcl	25.810764	10.613753	50.8611	62.868
Sdvig	210 × 42	2.32	0.887	4.74	–
Sdvig	280 × 56	2.41	0.870	5.20	–
Sdvig	350 × 70	2.16	1.20	3.75	–
SOPALE	250 × 40	0.98828	0.77487	5.79275	–
SOPALE	350 × 60	1.53302	1.343546	3.47284	–
SOPALE	500 × 120	1.07042	0.8338571	5.3991	–
Average[a]		1.44 ± 0.52	0.88 ± 0.20	5.28 ± 0.81	76.3 ± 7.6

[a] Averages for internal rate of dissipation of energy, gravitational rate of work, and root-mean-square velocity without SDEM.

Table A.7
Surface slope[a] evolution for experiment 2.

Code	Resolution (elements)	1.0	1.5	2.0	2.5	3.0	3.5	4.0	4.5	5.0	5.5	6.0	6.5	7.0	7.5	8.0	8.5	9.0	9.5	10.0
		cm of shortening																		
Elfen	3700–9000	–	–	–	–	–	–	4	4	4	6	6	5	6	7	–	–	–	–	4
Elfen	14700–15100	–	–	–	–	6	10	13	14	12	10	9	10	10	10	6	6	7	6	6
GALE	128 × 32	–	–	–	–	–	–	–	2	2	3	5	6	8	8	8	5	6	6	6
GALE	256 × 64	–	–	–	–	–	9	15	20		5	6	6	6	–	7	7	–	–	6
GALE	512 × 128	–	–	–	–	–	3	7	10	13	5	6	6	6	7	10	9	9	9	8
I3VIS	350 × 60	–	–	10	14	15	20	5	7	8	8	9	11	10	10	10	9	8	9	9
I3VIS	700 × 60	23	30	15	19	9	9	12	14	15	16	8	7	7	9	8	8	8	8	8
I3VIS 3-D 9 cm[b]	350 × 30 × 90	–	–	–	–	5	5	–	10	15	19	22	24	–	11	12	13	13	12	11
MILAMIN_VEP	250 × 40	–	–	–	–	5	7	11	14	17	19	9	9	6	7	7	7	7	8	8
MILAMIN_VEP	350 × 60	–	–	–	5	9	16	18	5	6	7	8	9	11	6	6	7	6	7	7
MILAMIN_VEP	700 × 120	–	–	–	5	6	7	10	10	5	5	6	6	8	8	5	5	6	6	6
pTatin	128 × 32	–	–	–	–	–	–	–	–	3	3	3	4	5	5	6	6	5	4	4
pTatin	256 × 44	–	–	–	–	–	–	–	3	4	3	4	5	5	–	–	–	–	–	–
pTatin	512 × 128	–	–	–	8	13	18	7	6	6	6	–	–	–	–	–	–	–	–	–
SOPALE	250 × 40	–	–	–	–	5	8	11	15	6	5	6	8	8	9	11	12	6	6	7
SOPALE	350 × 60	–	–	–	–	8	13	16	6	7	8	9	10	12	13	–	7	7	8	9
SOPALE	500 × 120	–	–	–	5	7	10	14	13	5	6	6	6	6	7	10	10	7	6	7

[a] Values only listed for stages at which surface slope could reliably be determined. All measurements in degrees and average of 2 measures (S.B. and G.S.).
[b] Width of 3-D model measured along mobile wall. Surface slope measurements on section through middle of model domain. Measurements for I3VIS 3-D 9 cm are at 30.9, 37.0, 43.1, 49.2, 54.6, 62.9, 65.7, 74.4, 80.0, 84.6, 89.2, 95.5, and 100.3 mm of shortening.

Table A.8
Dip angles[a] of first shear zones for experiment 2.

Code	Resolution (elements)	Forward thrust				Backward thrust			
		Shortening (cm)	Bottom (°)	Middle (°)	Top (°)	Shortening (cm)	Bottom (°)	Middle (°)	Top (°)
Elfen	3700–9000	0.4	39	39	47	0.4	50	52	54
Elfen	14700–15100	0.4	40	40	40	0.4	44	44	44
GALE	128 × 32	0.4	44	44	44	0.4	45	45	45
GALE	256 × 64	0.2	40	43	45	0.2	43	43	43
GALE	512 × 128	0.4	27	33	39	0.4	34	37	42
I3VIS	350 × 60	0.2	39	40	42	0.2	43	43	43
I3VIS	700 × 60	0.2	39	42	42	0.2	43	45	50
I3VIS 3-D 9 cm[b]	350 × 30 × 90	0.6	38	38	38	0.6	40	40	40
I3VIS 3-D 18.6 cm[b]	350 × 30 × 186	0.6	33	34	34	0.6	42	42	42
MILAMIN_VEP	250 × 40	0.4	32	34	42	0.4	40	41	41
MILAMIN_VEP	350 × 60	0.4	27	29	36	0.4	43	45	45
MILAMIN_VEP	700 × 120	0.4	24	24	29	0.5	54	54	54
pTatin	128 × 32	0.75	–	41	40	0.75	–	40	39
pTatin	256 × 64	0.75	–	41	41	0.75	–	42	42
pTatin	512 × 128	0.5	–	45	45	0.5	–	40	40
SDEM	22185 ptcl	5.0	31	33	–	5.0	29	31	–
SDEM	44594 ptcl	2.0	30	31	32	2.0	41	40	–
SDEM	87936 ptcl	1.0	26	25	22	1.0	25	30	–
Sdvig	280 × 56	0.4	36	39	40	0.4	41	41	41
Sdvig	350 × 70	0.4	33	37	41	0.4	39	44	46
SOPALE	250 × 40	0.2	21	–	39	0.2	40	–	51
SOPALE	350 × 60	0.2	20	–	46	0.2	49	53	55
SOPALE	500 × 120	0.2	21	39	44	0.4	49	49	51

[a] All measurements average of 2 measures (S.B. and G.S.).
[b] Width of 3-D model measured along mobile wall. Dip measurements on section through middle of model domain.

Table A.9
Number[a] of shear zones at 10 cm of shortening for experiment 2.

Code	Resolution (elements)	Forward thrusts (number)	Backward thrusts (number)
Elfen	3700–9000	4	5
Elfen	14700–15100	3	3
GALE	128 × 32	3	3
GALE	256 × 64	5	5
GALE	512 × 128	6	4
I3VIS	350 × 60	9	10
I3VIS	700 × 60	9	7
I3VIS 3-D 9 cm	350 × 30 × 90	5	4
I3VIS 3-D 18.6 cm	350 × 30 × 186	5	5
MILAMIN_VEP	250 × 40	4	4
MILAMIN_VEP	350 × 60	4	5
MILAMIN_VEP	700 × 120	4	6
pTatin	128 × 32	3	3
pTatin	256 × 64	6	2
pTatin	512 × 128	9	3
SDEM	22185 ptcl	4	2
SDEM	44594 ptcl	2	3
SDEM	87936 ptcl	3	2
Sdvig	280 × 56	5	2
Sdvig	350 × 70	4	2
SOPALE	250 × 40	5	3
SOPALE	350 × 60	5	5
SOPALE	500 × 120	5	3
Numerical average[b,c]		5 ± 2	4 ± 2
Analogue average[c,d]		4 ± 1	4 ± 2

[a] Shear zones that are recognisable in the finite deformation and strain plots at 10 cm shortening.
[b] Average of 2-D models.
[c] Rounded to integers.
[d] For sections through centre of models (Schreurs et al., 2016).

Table A.10
Quantification of experiment 3 at 10 cm shortening.

Code	Resolution in sand (elements)	Dissipation ($\times 10^{-4}$ W m^{-1})	Gravitational rate of work ($\times 10^{-4}$ W m^{-1})	V_{rms} ($\times 10^{-6}$ m s^{-1})	Applied force (N m^{-1})
Elfen	3700–8800	–	1.05	4.52	32.1
Elfen	14700–15300	–	1.02	4.21	30.4
GALE	128 × 32	1.02109	0.831172	5.80677	–
GALE	256 × 64	0.957492	0.689957	6.03455	–
GALE	512 × 128	0.892108	0.699431	6.2645	–
I3VIS	350 × 60	1.33156	0.992048	4.7762	–
I3VIS	700 × 60	1.43868	0.755911	5.5941	–
MILAMIN_VEP	250 × 40	1.344738	1.100506	4.594150	28.957608
MILAMIN_VEP	350 × 60	0.956627	0.802562	5.991020	30.210429
MILAMIN_VEP	700 × 120	0.902563	0.758568	5.873762	29.745289
pTatin	128 × 32	1.318371	0.970080	6.113167	16.247551
pTatin	256 × 64	1.770843	1.114301	4.008796	25.496140
pTatin	512 × 128	1.582941	0.940965	4.221023	19.058124
Sdvig	210 × 42	1.84	1.11	4.78	–
Sdvig	280 × 56	1.92	1.20	4.55	–
Sdvig	350 × 70	1.55	1.14	4.80	–
SOPALE	200 × 40	1.309364	1.111828	4.552730	–
SOPALE	350 × 60	1.303263	1.058328	4.758593	–
SOPALE	400 × 75	1.254807	1.042812	4.742997	–
Average		1.33 ± 0.31	0.97 ± 0.16	5.06 ± 0.72	26.5 ± 5.5

Table A.11
Surface slope[a] evolution for experiment 3.

Code	Resolution (elements)	1.0	1.5	2.0	2.5	3.0	3.5	4.0	4.5	5.0	5.5	6.0	6.5	7.0	7.5	8.0	8.5	9.0	9.5	10.0
		cm of shortening																		
Elfen	3700–8800	–	–	–	19	27	28	18	21	23	22	17	18	18	18	–	–	8	9	9
Elfen	14700–15300	–	–	–	10	15	16	17	15	18	18	19	18	18	17	16	17	16	16	–
GALE	128 × 32	–	–	–	–	13	18	22	26	27	20	21	24	25	25	20	20	17	18	12
GALE	256 × 64	–	11	22	30	16	17	22	25	26	19	20	22	–	17	18	19	19	20	20
GALE	512 × 128	–	–	6	11	17	16	20	23	22	22	24	17	18	19	19	16	16	17	12
I3VIS	350 × 60	9	17	13	17	18	15	19	18	19	16	18	19	18	18	18	17	16	17	17
I3VIS	700 × 60	10	10	15	17	17	19	19	18	18	18	19	20	18	18	18	13	14	14	12
MILAMIN_VEP	250 × 40	–	–	–	9	16	19	13	15	20	18	17	18	21	17	19	20	22	19	18
MILAMIN_VEP	350 × 60	–	–	8	11	17	20	19	20	22	14	17	20	20	18	20	21	–	10	10
MILAMIN_VEP	700 × 120	–	–	9	9	12	13	13	11	11	12	13	13	8	9	10	11	12	13	13
pTatin	128 × 32	–	–	–	–	–	–	20	24	27	27	27	23	23	23	–	–	–	–	–
pTatin	256 × 64	–	15	19	20	18	20	21	–	–	–	–	–	–	–	–	–	–	–	–
pTatin	512 × 128	–	–	–	5	9	11	10	12	14	16	–	6	6	5	6	7	8	8	8
Sdvig	280 × 56	–	–	–	–	16	16	18	21	22	24	18	19	19	19	20	22	20	21	20
Sdvig	350 × 70	–	–	15	–	10	13	14	14	19	19	19	20	19	20	20	20	20	19	18
SOPALE	200 × 40	–	7	10	14	15	13	16	18	16	18	19	15	17	18	19	20	13	14	15
SOPALE	350 × 60	–	–	–	9	12	12	15	17	18	16	12	13	15	13	14	15	12	12	13
SOPALE	400 × 75	–	–	–	–	8	7	8	10	12	13	9	13	17	13	14	15	12	11	12

[a] Values only listed for stages at which surface slope could reliably be determined. All measurements in degrees and average of 2 measures (S.B. and G.S.).

Table A.12
Dip angles[a] of first shear zones for experiment 3.

Code	Resolution (elements)	Forward thrust				Backward thrust			
		Shortening (cm)	Bottom (°)	Middle (°)	Top (°)	Shortening (cm)	Bottom (°)	Middle (°)	Top (°)
Elfen	3700–8800	0.4	33	38	46	0.4	32	41	42
Elfen	14700–15300	0.4	35	37	38	0.4	39	38	38
GALE	128 × 32	0.4	46	43	40	0.4	40	42	40
GALE	256 × 64	0.2	36	38	42	0.2	36	40	43
GALE	512 × 128	0.2	32	40	45	0.2	26	37	41
I3VIS	350 × 60	0.21	38	38	37	0.21	38	39	41
I3VIS	700 × 60	0.2	40	39	39	0.2	38	38	40
MILAMIN_VEP	250 × 40	0.4	21	25	–	0.4	22	29	42
MILAMIN_VEP	350 × 60	0.4	24	24	35	0.4	22	22	38
MILAMIN_VEP	700 × 120	0.4	27	28	29	0.4	23	27	30
pTatin	128 × 32	0.5	38	42	41	0.5	39	43	44
pTatin	256 × 64	0.5	34	40	40	0.5	39	43	43
pTatin	512 × 128	0.5	21	36	37	0.5	39	42	44
Sdvig	280 × 56	0.4	34	38	46	0.4	38	40	42
Sdvig	350 × 70	0.4	15	32	41	0.4	21	35	40
SOPALE	200 × 40	0.4	38	41	41	0.4	30	42	43
SOPALE	350 × 60	0.5	26	35	41	0.5	28	26	37
SOPALE	400 × 75	0.4	25	25	33	0.4	18	31	38

[a] All measurements average of 2 measures (S.B. and G.S.).

Table A.13
Number[a] of shear zones at 10 cm of shortening for experiment 3.

Code	Resolution (elements)	Forward thrusts (number)	Backward thrusts (number)
Elfen	3700–8800	6	2
Elfen	14700–15300	5	2
GALE	128 × 32	6	1
GALE	256 × 64	5	1
GALE	512 × 128	7	3
I3VIS	350 × 60	9	1
I3VIS	700 × 60	11	4
MILAMIN_VEP	250 × 40	6	1
MILAMIN_VEP	350 × 60	7	2
MILAMIN_VEP	500 × 120	7	3
pTatin	128 × 32	4	2
pTatin	256 × 64	7	4
pTatin	512 × 128	7	5
Sdvig	280 × 56	5	1
Sdvig	350 × 70	6	1
SOPALE	200 × 40	7	2
SOPALE	350 × 60	8	2
SOPALE	400 × 75	8	2
Numerical average[b]		7 ± 2	2 ± 1
Analogue average[b,c]		6 ± 1	1 ± 0

[a] Shear zones that are recognisable in the finite deformation and strain plots at 10 cm shortening.
[b] Rounded to integers.
[c] For sections through centre of models (Schreurs et al., 2016).

Appendix B. Numerical sensitivity tests

We used experiment 2 to test the sensitivity of the wedge experiments to the type of finite element (Fig. B.31), the time step (Fig. B.32), the implementation of boundary friction (Fig. B.33a,b), and the frequency of grid remeshing (Fig. B.33b,c) (section 5.5.1). While the individual styles of the wedge experiments are mostly preserved, these tests illustrate the intrinsic high sensitivity of rigid-plastic wedge experiments to changes in numerical parameters. In addition to the tests shown here, experiments 2 and 3 were run at 2 to 3 different resolutions for each of the participating codes (Figs. 9 and 22 and other results throughout in figures and tables). Fig. 20 shows the effects of varying magnitude of basal friction (section 5.5.2).

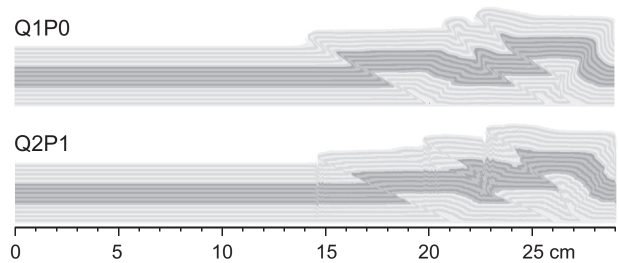

Figure B.31. Comparison of experiment 2 at 6 cm of shortening for Q1P0 elements (top) with linear velocity interpolation and constant pressure and Q2P1 elements (bottom) with quadratic velocity and linear pressure. Models run with MILAMIN_VEP at an elemental resolution of 350 × 60 elements in the sand domain.

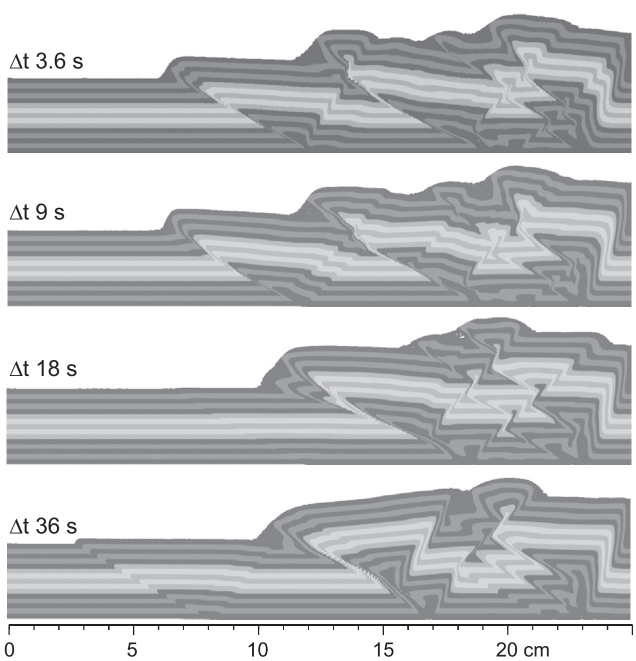

Figure B.32. Comparison of experiment 2 at 10 cm of shortening for time steps 3.6, 9, 18, and 36 s. 3.6 s was prescribed and used by most codes, Sdvig used 14.4 s and pTatin 36 s. Models run with SOPALE at an elemental resolution of 350 × 60 elements in the sand domain.

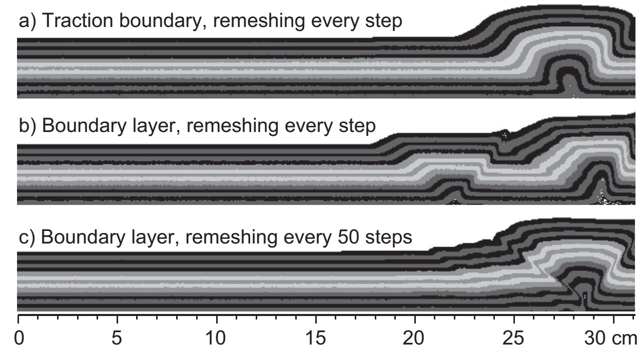

Figure B.33. Comparison of pTatin results for experiment 2 at 3.9 cm of shortening. a) Original model (e.g., Figs. 8, 10 and 11) with a shear traction frictional boundary and grid remeshing every time step. b) Model with a frictional boundary layer and remeshing every time step. Velocity is not interpolated from the old to the new mesh. c) Model with a frictional boundary layer and remeshing every 50 time steps. Velocity is interpolated from the old to the new mesh. Models run at an elemental resolution of 256 × 32 elements in the sand domain.

References

Amestoy, P., Duff, I., L'Excellent, J.-Y., Koster, J., 2001. A fully asynchronous multifrontal solver using distributed dynamic scheduling. SIAM J. Matrix Anal. Appl. 23, 1541.

Amestoy, P., Guermouche, A., L'Excellent, J.-Y., Pralet, S., 2006. Hybrid scheduling for the parallel solution of linear systems. Parallel Comput. 32, 136156.

Arthur, J.R.F., Dunstan, T., Al-Ani, Q.A.J., Assadi, A., 1977. Plastic deformation and failure of granular media. Géotechnique 27, 53–74.

Bésuelle, P., Desrues, J., Raynaud, S., 2000. Experimental characterisation of the localisation phenomenon inside a Vosges sandstone in a triaxiall cell. Int. J. Rock Mech. Min. Sci. 37, 1223–1237.

Blankenbach, B., Busse, F., Christensen, U., Cserepes, L., Gunkel, D., Hansen, U., Harder, H., Jarvis, G., Koch, M., Marquart, G., Moore, D., Olsen, P., Schmeling, H., Schnaubelt, T., 1989. A benchmark comparison for mantle convection codes. Geophys. J. Int. 98, 23–38.

Brezzi, F., Fortin, M., 1991. Mixed and Hybrid Finite Element Methods. Springer-Verlag New York, Inc.

Buiter, S.J.H., Babeyko, A.Yu, Ellis, S., Gerya, T.V., Kaus, B.J.P., Kellner, A., Schreurs, G., Yamada, Y., 2006. The numerical sandbox: comparison of model results for a shortening and an extension experiment. In: Buiter, S.J.H., Schreurs, G. (Eds.), Analogue and Numerical Modelling of Crustal-scale Processes, 253. Geol. Soc., Lond., Spec. Publ, pp. 29–64.

Buiter, S.J.H., 2012. A review of brittle compressional wedge models. Tectonophysics 530–531, 1–17. http://dx.doi.org/10.1016/j.tecto.2011.12.018.

Burbidge, D.R., Braun, J., 2002. Numerical models of the evolution of accretionary wedges and fold-and-thrust belts using the distinct-element method. Geophys. J. Int. 148, 542–561.

Cadell, H.M., 1890. Experimental researches in mountain building. Trans. R. Soc. Edinb. 35, 337–357.

Choi, E., Petersen, K.D., 2015. Making Coulomb angle-oriented shear bands in numerical tectonic models. Tectonophysics 657, 94–101. http://dx.doi.org/10.1016/j.tecto.2015.06.026.

Cooke, M.L., Pollard, D.D., 1997. Bedding plane slip in initial stages of fault-related folding. J. Struct. Geol. 19, 567–581.

Cooke, M.L., Madden, E.H., 2014. Is the earth lazy? A review of work minimization in fault evolution. J. Struct. Geol. 66, 334–346. http://dx.doi.org/10.1016/j.jsg.2014.05.004.

Coulomb, C.A., 1773. L'application des règles de maximis et minimis à quelques problèmes de statique, relatifs à l'architecture. Mém. Math. Phys. Acad. Roy. Sci. 7, 343–382.

Crameri, F., Schmeling, H., Golabek, G.J., Duretz, T., Orendt, R., Buiter, S.J.H., May, D.A., Kaus, B.J.P., Gerya, T.V., Tackley, P.J., 2012. A comparison of numerical surface topography calculations in geodynamic modelling: an evaluation of the sticky air method. Geophys. J. Int. 189, 38–54. http://dx.doi.org/10.1111/j.1365-246X.2012.05388.x.

Crook, A.J.L., Wilson, S.M., Yu, J.G., Owen, D.R.J., 2006. Predictive modelling of structure evolution in sandbox experiments. J. Struct. Geol. 28, 729–744. http://dx.doi.org/10.1016/j.jsg.2006.02.002.

Cubas, N., Maillot, B., Barnes, C., 2010. Statistical analysis of an experimental compressional sand wedge. J. Struct. Geol. 32, 818–831. http://dx.doi.org/10.1016/j.jsg.2010.05.010.

Cundall, P., Strack, O., 1979. A discrete numerical model for granular assemblies. Géotechnique 29, 47–65.

Dahlen, F.A., 1984. Noncohesive critical Coulomb wedges: an exact solution. J. Geophys. Res. 89, 10,125–10,133.

Dahlen, F.A., Suppe, J., Davis, D., 1984. Mechanics of fold-and-thrust belts and accretionary wedges: cohesive Coulomb theory. J. Geophys. Res. 89, 10,087–10,101.
Davis, D., Suppe, J., Dahlen, F.A., 1983. Mechanics of fold-and-thrust belts and accretionary wedges. J. Geophys. Res. 88, 1153–1172.
Davis, D.M., Engelder, T., 1985. The role of salt in fold-and-thrust belts. Tectonophysics 119, 67–88.
Egholm, D.L., 2007. A new strategy for discrete element numerical models: 1. Theory. J. Geophys. Res. 112, B05203. http://dx.doi.org/10.1029/2006JB004557.
Egholm, D.L., Sandiford, M., Clausen, O.R., Nielsen, S.B., 2007. A new strategy for discrete element numerical models: 2. Sandbox applications. J. Geophys. Res. 112, B05204. http://dx.doi.org/10.1029/2006JB004558.
Ellis, S., Schreurs, G., Panien, M., 2004. Comparisons between analogue and numerical models of thrust wedge development. J. Struct. Geol. 26, 1659–1675. http://dx.doi.org/10.1016/j.jsg.2004.02.012.
Exadaktylos, G.E., Vardoulakis, I., Stavrpoulou, M.C., Tsombos, P., 2003. Analogue and numerical modeling of normal fault patterns produced due to slip along a detachment zone. Tectonophysics 376, 117–134.
Fullsack, P., 1995. An arbitrary Lagrangian-Eulerian formulation for creeping flows and its application in tectonic models. Geophys. J. Int. 120, 1–23.
Gerya, T.V., 2010. Introduction to Numerical Geodynamic Modelling. Cambridge University Press, p. 345.
Gerya, T.V., Yuen, D.A., 2007. Robust characteristics method for modelling multiphase visco-elasto-plastic thermo-mechanical problems. Phys. Earth Planet. Int. 163, 83–105. http://dx.doi.org/10.1016/j.pepi.2007.04.015.
Graveleau, F., Malavieille, J., Dominguez, S., 2012. Experimental modelling of orogenic wedges: a review. Tectonophysics 538–540, 1–66. http://dx.doi.org/10.1016/j.tecto.2012.01.027.
Gutscher, M.-A., Kukowski, N., Malavieille, J., Lallemand, S., 1998. Material transfer in accretionary wedges from analysis of a systematic series of analog experiments. J. Struct. Geol. 20, 407–416.
Hubbert, M.K., 1937. Theory of scale models as applied to the study of geologic structures. Bull. Geol. Soc. Am. 48, 1459–1520.
Huiqi, L., McClay, K.R., Powell, D., 1992. Physical Models of Thrust Wedges. In: McClay, K.R. (Ed.), Thrust Tectonics. Chapman and Hall, New York, pp. 71–81.
Kaus, B.J.P., 2010. Factors that control the angle of shear bands in geodynamic numerical models of brittle deformation. Tectonophyiscs 484, 36–47. http://dx.doi.org/10.1016/j.tecto.2009.08.042.
Klinkmüller, M., Schreurs, G., Rosenau, M., Kemnitz, H., 2016. Properties of granular analogue model materials: a community wide survey. Tectonophysics. http://dx.doi.org/10.1016/j.tecto.2016.01.017.
Koyi, H., 1995. Mode of internal deformation in sand wedges. J. Struct. Geol. 17, 293–300.
Krabbenhoft, K., Damkilde, L., 2003. A general non-linear optimization algorithm for lower bound limit analysis. Int. J. Num. Methods Eng. 56, 165–184.
Krabbenhoft, K., Lyamin, A.V., 2014. Optum G2, Optum Computational Engineering, www.optumce.com.
Krabbenhoft, K., Lyamin, A.V., Hjiaj, M., Sloan, S.W., 2005. A new discontinuous upper bound limit analysis formulation. Int. J. Num. Methods Eng. 63, 1069–1088.
Krantz, R.W., 1991. Measurements of friction coefficients and cohesion for faulting and fault reactivation in laboratory models using sand and sand mixtures. Tectonophysics 188, 203–207.
Lemiale, V., Mühlhaus, H.-B., Moresi, L., Stafford, J., 2008. Shear banding analysis of plastic models formulated for incompressible viscous flows. Phys. Earth Planet. Sci. Lett. 171, 177–186. http://dx.doi.org/10.1016/j.pepi.2008.07.038.
Le Pourhiet, L., Mattioni, L., Moretti, I., 2006. 3D modelling of rifting through a pre-existing stack of nappes in the Gulf of Corinth (Greece): a mixed analogue/numerical approach. In: Buiter, S.J.H., Schreurs, G. (Eds.), Analogue and Numerical Modelling of Crustal-scale Processes, 253. Geol. Soc., Lond., Spec. Publ., pp. 233–252
Lohrmann, J., Kukowski, N., Adam, J., Oncken, O., 2003. The impact of analogue material properties on the geometry, kinematics, and dynamics of convergent sand wedges. J. Struct. Geol. 25, 1691–1711.
Majmudar, T.S., Behringer, R.P., 2005. Contact force measurements and stress-induced anisotropy in granular materials. Nature 435, 1079–1082.
Marshak, S., Wilkerson, M.S., 1992. Effect of overburden thickness on thrust belt geometry and development. Tectonics 11, 560–566.
Mary, B.C.L., Maillot, B., Leroy, Y.M., 2013. Predicting orogenic wedge styles as a function of analogue erosion law and material softening. Geochem. Geophys. Geosyst. 14 (10) http://dx.doi.org/10.1002/ggge.20262.
May, D.A., Brown, J., Le Pourhiet, L., 2014. pTatin3D: high-performance methods for long-term lithospheric dynamics. In: Proceedings of the International Conference for High Performance Computing, Networking, Storage and Analysis. IEEE Press, pp. 274–284.
May, D.A., Brown, J., Le Pourhiet, L., 2015. A scalable, matrix-free multigrid preconditioner for finite element discretizations of heterogeneous stokes flow. Comput. Methods Appl. Mech. Eng. 290, 496–523. http://dx.doi.org/10.1016/j.cma.2015.03.014.
McClay, K.R., 1990. Extensional fault systems in sedimentary basins: a review of analogue model studies. Mar. Petrol. Geol. 7, 206–233.
Mulugeta, G., 1988. Modelling the geometry of Coulomb thrust wedges. J. Struct. Geol. 10, 847–859.
Nilfouroushan, F., Pysklywec, R., Cruden, A., 2012. Sensitivity analysis of numerical scaled models of fold-and-thrust belts to granular material cohesion variation and comparison with analog experiments. Tectonophysics 526–529, 196–206. http://dx.doi.org/10.1016/j.tecto.2011.06.022.
Panian, J., Wiltschko, D., 2007. Ramp initiation and spacing in a homogeneous thrust wedge. J. Geophys. Res. 112, B05417. http://dx.doi.org/10.1029/2004JB003596.
Panien, M., Buiter, S.J.H., Schreurs, G., Pfiffner, O.A., 2006a. Inversion of a symmetric basin: insights from a comparison between analogue and numerical experiments. In: Buiter, S.J.H., Schreurs, G. (Eds.), Analogue and Numerical Modelling of Crustal-scale Processes, 253. Geol. Soc., Lond., Spec. Publ, pp. 253–270.
Panien, M., Schreurs, G., Pfiffner, A., 2006b. Mechanical behaviour of granular materials used in analogue modelling: insights from grain characterisation, ring-shear tests and analogue experiments. J. Struct. Geol. 28, 1710–1724. http://dx.doi.org/10.1016/j.jsg.2006.05.004.
Roscoe, K.H., 1970. The influence of strains in soil mechanics. Géotechnique 20, 129–170.
Ruh, J.B., Gerya, T., Burg, J.-P., 2013. High-resolution 3D numerical modeling of thrust wedges: influence of décollement strength on transfer zones. Geochem. Geophys. Geosyst. 14 (4), 1131–1155. http://dx.doi.org/10.1002/ggge.20085.
Saltzer, S.D., 1992. Boundary conditions in sandbox models of crustal extension: an analysis using distinct elements. Tectonophysics 215, 349–362.
Saltzer, S.D., Pollard, D.D., 1992. Distinct element modeling of structures formed in sedimentary overburden by extensional reactivation of basement normal faults. Tectonics 11, 165–174.
Seyferth, M., Henk, A., 2006. A numerical sandbox: high-resolution distinct element models of halfgraben formation. Int. J. Earth. Sci. 95, 189–203. http://dx.doi.org/10.1007/s00531-005-0034-x.
Schellart, W.P., 2000. Shear test results for cohesion and friction coefficients for different granular materials: scaling implications for their usage in analogue modelling. Tectonophysics 324, 1–16.
Schenk, O., Gärtner, K., 2004. Solving unsymmetric sparse systems of linear equations with PARDISO. J. Future Gen. Comput. Syst. 20, 475–487.
Schenk, O., Gärtner, K., 2006. On fast factorization pivoting methods for symmetric indefinite systems. Elec. Trans. Numer. Anal. 23, 158–179.
Schmeling, H., Babeyko, A.Y., Enns, A., Faccenna, C., Funiciello, F., Gerya, T., Golabek, G.J., Grigull, S., Kaus, B.J.P., Morra, G., Schmalholz, S.M., van Hunen, J., 2008. A benchmark comparison of spontaneous subduction models – towards a free surface. Phys. Earth Planet. Int. 171, 198–223. http://dx.doi.org/10.1016/j.pepi.2008.06.028.
Schreurs, G., Buiter, S.J.H., Boutelier, D., Corti, G., Costa, E., Cruden, A.R., Daniel, J.-M., Hoth, S., Koyi, H.A., Kukowski, N., Lohrmann, J., Ravaglia, A., Schlische, R.W., Withjack, M.O., Yamada, Y., Cavozzi, C., Delventisette, C., Elder Brady, J.A., Hoffmann-Rothe, A., Mengus, J.-M., Montanari, D., Nilforoushan, F., 2006. Analogue benchmarks of shortening and extension experiments. In: Buiter, S.J.H., Schreurs, G. (Eds.), Analogue and Numerical Modelling of Crustal-scale Processes, 253. Geol. Soc., Lond., Spec. Publ, pp. 1–27.
Schreurs, G., Buiter, S.J.H., Boutelier, J., Burberry, C., Callot, J.-P., Cavozzi, C., Cerca, M., Chen, J.-H., Cristallini, E., Cruden, A.R., Cruz, L., Daniel, J.-M., Da Poian, G., Garcia, V.H., Gomes, V.J.S., Grall, C., Guillot, Y., Guzmán, C., Nur Hidayah, T., Hilley, G., Klinkmüller, M., Koyi, H.A., Lu, C.-Y., Maillot, B., Meriaux, C., Nilfouroushan, F., Pan, C.-C., Pillot, D., Portillo, R., Rosenau, M., Schellart, W.P., Schlische, R.W., Take, A., Vendeville, B., Vergnaud, M., Vettori, M., Wang, S.-H., Withjack, M.O., Yagupsky, D., Yamada, Y., 2016. Benchmarking analogue models of brittle thrust wedges. J. Struct. Geol. in (this issue).
Shackleton, J.R., Cooke, M.L., 2007. Is plane-strain a valid assumption in non-cylindrical fault-cored folds? J. Struct. Geol. 29, 1229–1240.
Simpson, G., 2011. Mechanics of non-critical fold-thrust belts based on finite element models. Tectonophysics 499, 142–155. http://dx.doi.org/10.1016/j.tecto.2011.01.004.
Smart, K.J., Couzens-Schultz, B.A., 2001. Mechanics of blind thrusting: comparison of numerical and physical modelling. J. Geol. 109, 771–779.
Stockmal, G.S., Beaumont, C., Nguyen, M., Lee, B., 2007. Mechanics of thin-skinned fold-and-thrust belts: insights from numerical models. In: Sears, J.W., Harms, T.A., Evenchick, C.A. (Eds.), Whence the Mountains? Inquiries into the Evolution of Orogenic Systems: a Volume in Honor of Raymond a. Price, Geol. Soc. Am. Spec. Paper, 433, pp. 63–98. http://dx.doi.org/10.1130/2007.2433(04).
Souloumiac, P., Leroy, Y.M., Maillot, B., Krabbenhoft, K., 2009. Predicting stress distributions in fold-and-thrust belts and accretionary wedges by optimization. J. Geophys. Res. 114, B09404. http://dx.doi.org/10.1029/2008JB005986.
Souloumiac, P., Maillot, B., Leroy, Y.M., 2012. Bias due to side wall friction in sand box experiments. J. Struct. Geol. 35, 90–101. http://dx.doi.org/10.1016/j.jsg.2011.11.002.
Thieulot, C., 2011. FANTOM: two- and three-dimensional numerical modelling of creeping flows for the solution of geological problems. Phys. Earth Planet. Inter 188, 4768.
Thieulot, C., 2014. ELEFANT: a user-friendly multipurpose geodynamics code. Solid Earth Discuss. 6, 1949–2096.
Van Keken, P.E., Currie, C., King, S.D., Behn, M.D., Cagnioncle, A., He, J., Katz, R.F., Lin, S.-C., Parmentier, E.M., Spiegelman, M., Wang, K., 2008. A community benchmark for subduction zone modeling. Phys. Earth Planet. Int. 171, 187–197. http://dx.doi.org/10.1016/j.pepi.2008.04.015.
Vermeer, P.A., 1990. The orientation of shear bands in biaxial tests. Géotechnique 40, 223–236.
Zhao, W.-L., Davis, D.M., Dahlen, F.A., Suppe, J., 1986. Origin of convex accretionary wedges: evidence from Barbados. J. Geophys. Res. 91, 10,246–10,258.